Rôle du squelette granulaire dans le comportement du béton sous trés fortes contraintes : analyse expérimentale et numérique.

Ewa Piotrowska Paulina

UNIVERSITÉ DE GRENOBLE

THÈSE

Pour obtenir le grade de

DOCTEUR DE L'UNIVERSITÉ DE GRENOBLE

Spécialité: **Ingénierie-Matériaux Mécanique Énergétique Environnement Procédés Production (510)**

Arrêté ministériel: 7 août 2006

Présentée par

Ewa PIOTROWSKA

Thèse dirigée par **Yann Malécot** et
co-dirigée par **Vincent Richefeu**

préparée au sein du **Laboratoire 3SR**
dans **l'École Doctorale IMEP2**

Role of coarse aggregates in the triaxial behavior of concrete: experimental and numerical analysis

Thèse soutenue publiquement le **15.07.2013**,
devant le jury composé de:

M. Laurent Daudeville
Professeur à l'UJF - Grenoble I, Président
M. Pascal Forquin
Professeur à l'Université de Lorraine, Rapporteur
M. Jean-Yves Delenne
Directeur de Recherche de l'INRA Montpellier, Rapporteur
M. Albert Noumowe
Professeur à l'Université de Cergy-Pontoise, Examinateur
M. Yann Malécot
Professeur à l'UJF - Grenoble I, Directeur de thèse
M. Vincent Richefeu
Maître de conférences à l'UJF - Grenoble I, Co-encadrant de thèse

"La vérité de demain se nourrit de l'erreur d'hier"

Antoine de St Exupéry

Acknowledgements

The process of writing and finalizing a Ph.D. thesis is something which cannot be accomplished alone. Therefore, I would like to thank all those who contributed to this thesis and supported me in writing it.

I'm especially grateful to my supervisor Yann Malécot whose guidance and critical reflection on my work were very precious during the whole process. Thank you for your constant encouragement which helped me a lot in completing my work successfully. I would like to express my great gratitude to my co-supervisor Vincent Richefeu for all the help and the numerous discussions which proved to be very important to the completion of this thesis.

I would also like to thank the members of the dissertation committee, Pascal Forquin, Jean-Yves Delenne, Albert Noumowe and Laurent Daudeville, for assessing this thesis and providing valuable comments.

Finally, I would like to thank my family and friends for all their support. Above all, special thanks to Jérôme for always believing in me and being there for me every step of the way.

Abstract

This PhD thesis focuses on identifying concrete behavior under high triaxial loading. The study is carried out within a more general context of understanding the behavior of concrete under impact, which induces very high-intensity triaxial stress states.

In order to reproduce very high stress levels with well-controlled loading paths, static triaxial tests are carried out on concrete samples by means of a very high-capacity triaxial press. We are interested in the influence of coarse aggregates, which occupy approximately 40% of the concrete volume. More specifically, the effects of coarse aggregate shape and composition on concrete behavior for triaxial compression tests ranging from 0 to 650 MPa of confinement are investigated. Both macroscopic response and failure patterns are concerned. Coarse aggregate shape seems to have only a slight influence on concrete behavior while the effects of coarse aggregate composition are quite important over whole range of confining pressures.

The second part of the thesis is devoted to a numerical modeling of concrete. The main objective of this numerical work is to develop a very simple model in terms of interaction laws and introduce concrete heterogeneity at the mesoscopic level. A mesoscopic model of concrete is thus established within the discrete element framework. The effects of coarse aggregate and aggregate/mortar interface properties on the stress-strain curves and damage mechanisms in a concrete sample are investigated. On the other hand, the influence of voids is studied using one-phase samples having different void properties. A complex, nonlinear behavior of a numerical specimen arising from the void structuring is observed. The numerical results complete and allow better understanding of experimental observations.

Keywords: Concrete, coarse aggregate, triaxial loading, high confinement, mesoscopic modeling

Résumé

Ce mémoire de thèse s'intéresse au comportement du béton sous chargement triaxial sévère. L'étude est réalisée dans le contexte plus général de la compréhension du comportement du béton sous impact, ce qui induit des états de contraintes triaxiales de très haute intensité.

Afin de reproduire des niveaux de contraintes très élevés avec des chemins de chargement bien contrôlés, des essais triaxiaux statiques sont réalisés sur des échantillons de béton au moyen d'une presse triaxiale de très grande capacité. Nous nous sommes intéressés à l'influence des granulats, qui occupent environ 40 % du volume du béton. Plus précisément, les effets de la forme et de la composition chimique des granulats sont étudiés pour des compression triaxiale entre 0 et 650 MPa de confinement . On considère à la fois la réponse macroscopique et les modes de rupture. La forme des granulats semble peu influencer le comportement du béton, alors que les effets de leur composition sont assez importants, quelque soit le confinement.

La deuxième partie de la thèse est consacrée à une modélisation numérique du béton. L'objectif principal de ce travail numérique est de développer un modèle très simple en termes de lois d'interaction et d'introduire l'hétérogénéité du béton au niveau mésoscopique. Un modèle mésoscopique du béton est ainsi établi dans le cadre des éléments discrets. On étudie l'influence des propriétés des granulats et de l'interface graulats/mortier sur les courbes contrainte-déformation et les mécanismes d'endommagement. D'autre part, l'influence des vides est étudiée en utilisant des échantillons mono-phasiques avec différentes caractéristiques des vides. Un comportement complexe non linéaire, résultant de la présence, des vides est observé. Par ailleurs, les résultats numériques complètent, et permettent de mieux comprendre, les résultats expérimentaux.

Mots clefs: Béton, granulats, chargement triaxial, fort confinement, modélisation mésoscopique

Contents

Notation

σ_x	axial stress
p_c	confining pressure
$q = \sigma_x - p$	deviatoric stress
$\sigma_m = \frac{\sigma_x + 2p}{3}$	mean stress
ε_x, ε_θ	axial, circumferential strain
ε'_x, ε'_θ	axial, circumferential strain in deviatoric part of the loading
ε_v	volumetric strain

σ_c	compressive strength
σ_t	tensile strength

Sign convention

$\sigma \geq 0$	in compression
$\varepsilon \geq 0$	in compression

Abbreviations

SR	Siliceous Rolled aggregate concrete
SC	Siliceous Crushed aggregate concrete
GB	Glass Ball concrete
LC	Limestone Crushed aggregate concrete
TXT 50 MPa	Triaxial compression test at 50 MPa of confining pressure

Introduction

As everyone knows, concrete is the world's most widely used man-made material. In particular, it is employed in the construction of sensitive structures intended to face extreme loading situations. An example of such a structure is a deflecting wall, built to divert snow avalanche flows. Figure 1 recalls the collapse of two deflecting walls, located in the valley of Chamonix under the Taconnaz glacier, after an exceptional avalanche in February 11th, 1999. In addition to natural risks such as avalanche, earthquake, hurricane, *etc.*, concrete structures are nowadays exposed to numerous man-made and technological hazards.

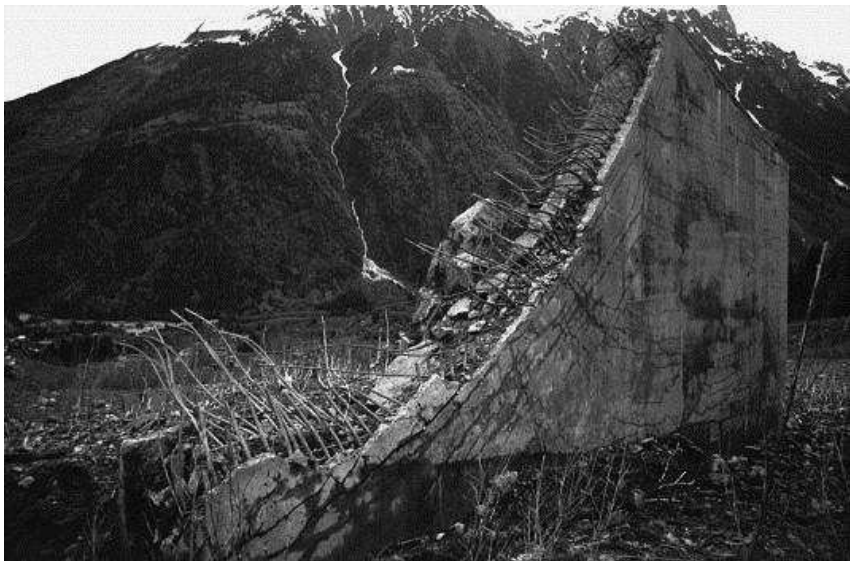

Figure 1: Deflecting wall in Taconnaz site destroyed by avalanche in February 11th, 1999 (image taken from Berthet-Rambaud *et al.* [4])

The general context of the research project enclosing this PhD thesis is thus the vulnerability of complex concrete infrastructure (high-rise buildings, dams, nuclear reactors, *etc.*) under extreme loading situations, such as near-field detonations or ballistic impacts. In these situations, concrete undergoes very high-intensity triaxial stress states (Zukas [71]). When a projectile strikes a concrete structure, various localized effects are generated: spalling on the front face of the structure can be associated with simple tension, while penetration of the projectile into the structural core constitutes the source of dynamic triaxial compression. If the target is thin enough, then both simple tension and

shear stresses can be observed on the distal face of the concrete specimen during the final penetration phase.

The ability to reproduce the concrete behavior under such extreme conditions with a numerical model is essential since full-scale dynamic tests and laboratory tests are very expensive and time-consuming. A validation of concrete behavior models, which simultaneously take into account the phenomena of brittle damage and irreversible strains, requires test results that enable reproducing these complex and intense loading paths.

The static characterization of a constitutive model to predict dynamic calculations represents a common practice in the study of geomaterials. The behavior of concrete in confined compression test slightly depends on the strain rate for dried or wet specimens (Forquin *et al.* [28]). Static triaxial compression is therefore the loading type discussed in this manuscript.

In 2004, the university of Grenoble launched, in collaboration with the CEA Gramat, a research program on the vulnerability of concrete infrastructure. A very-high capacity triaxial press was installed in the 3SR laboratory (University of Grenoble). Thanks to this innovative device, a large experimental campaign has been performed. The experimental studies focused on the influence of loading path (Gabet *et al.* [30], Poinard *et al.* [49], water/cement ratio, saturation degree, coarse aggregate size and cement paste volume (Vu *et al.* [66, 67, 64]) on concrete behavior under high confinement. This research program has been recently incorporated into the French research network PREVI (Pôle de Recherche sur la Vulnérabilité des Infrastructures), recognized by the French ministry of research, which groups laboratories of three universities: 3SR laboratory (University of Grenoble), LML laboratory (University of Lille 1), LEM3 laboratory (University of Lorraine) and one national research organization, CEA Gramat. These units aim at characterizing, understanding and modeling concrete behavior under extreme loading.

In this context, the experimental part of this work aims at investigating the effect of coarse aggregate on concrete behavior for triaxial compression tests ranging from 0 to 650 MPa of confinement. This issue is certainly interesting since coarse aggregates occupy approximately 40% of the concrete volume. Moreover, they exhibit various properties depending on both properties of the parent rock and aggregate creation process, that is natural process of weathering and abrasion or mechanical crushing. Although relatively complex nature of the problem, both apects of aggregate shape and surface texture, and aggregate compostion are concerned by this study.

The second part of the manuscript is devoted to numerical modeling. Due to a strongly heterogeneous nature, concrete can be considered at different scales, what is illustrated in Figure 1. Since we study here, the influence of coarse aggregate on concrete behavior, a mesoscopic model of concrete is developed. The mesoscopic modeling aims at better understanding of damage and failure mechanisms of concrete that come from its heterogeneity, such as large aggregates and also porosity. The importance of meso-scale porosity was underlined in X-ray tomographic observations of concrete samples submitted to hydrostatic compression (Poinard *et al.* [50]). Figure 2 shows selected images of this study. The second objective of the mesoscopic modeling is to be able to deduce the macroscopic behavior of concrete from the knowledge of the behaviors of its constituents. An efficient and accurate model could serve as a concrete mix optimization tool, so that the number of experiments could be reduced.

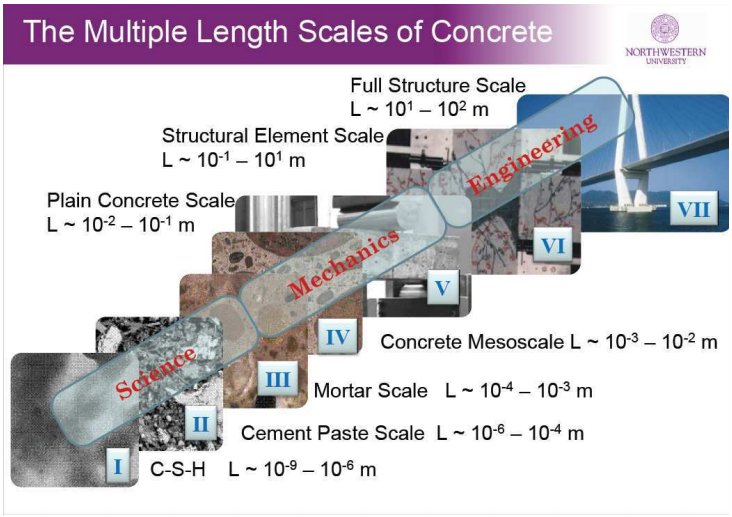

Figure 2: The multiple length scales of concrete (G. Cusatis, International PREVI Workshop on Concrete Structures under Impact and Blast Loads, 2013, Les Houches, France)

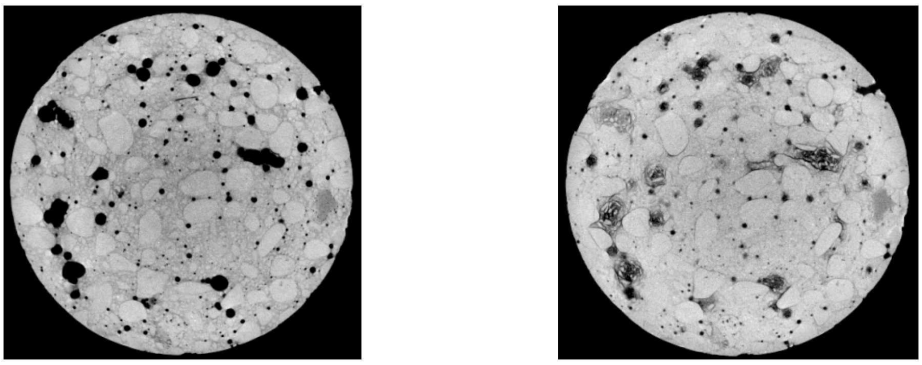

(a) (b)

Figure 3: Horizontal slice of concrete specimen submitted to hydrostatic loading (Poinard [**?**]
(a) undammaged state
(b) after 650 MPa

The manuscript is divided into four chapters.

Chapter 1 provides a bibliographic review, which in turn is integrated in three parts: the first briefly describes heterogeneities in concrete material; different aspects of concrete behavior under high triaxial loading are discussed in the second part, followed by a presentation of different approaches to concrete mesoscopic modeling in the last section of the chapter.

Chapter 2 presents the experimental study performed on four concretes differentiated by coarse aggregate type. The influence of both coarse aggregate shape and composition on concrete strength and failure mechanisms under confined compression loading is

investigated.

A mesoscopic model, formulated in DEM framework, is described in Chapter 3. The validation tests are presented.

The model is then employed in Chapter 4, to do a parametric study on aggregate and aggregate/mortar interface properties. The results are compared with main experimental observations.

At the end, final conclusions of this PhD work are drawn and research perspectives are discussed.

Chapter 1

Bibliographic study

The bibliographic review is divided into three parts. The first section will describe briefly the composite nature of concrete material and present research studies concerning characterization of the concrete mesostructure. Subsequently, mechanical behavior of concrete particularly under high triaxial loading will be reviewed. The response of concrete with respect to the meso-constituents will be discussed. The last part of this chapter will present different approaches to the mesoscopic modeling of concrete.

1.1 Concrete as a heterogeneous material

1.1.1 Concrete constituents

Concrete is basically made up of cement, aggregates and water. The fabrication process results in a composite material, conventionally represented as large aggregates embedded in a cohesive matrix, also called mortar (cement paste and fine aggregates), and characterized by the presence of porosity.

Cement paste

When the cement powder is mixed with water, hydration reactions occur which ultimately convert the water-cement suspension into a rigid porous material. Figure 1.1 presents a backscattered electron image of a Portland cement mortar with the microstructural constituents distinguished (Scrivener [57]). The hydrated cement paste can be thought of as consisting of four phases: unreacted cement, poorly crystallized hydrates of the various compounds (C-S-H gel), crystals of calcium hydroxide (CH) and capillary pore space. Two types of C-S-H can be distinguished: “outer” C-S-H formed in the initially water-filled space and “inner” C-S-H - more homogeneous product that forms rims within the original boundaries of cement grain (Taylor [60]). In addition, within the gel there exist interstitial voids called gel pores.

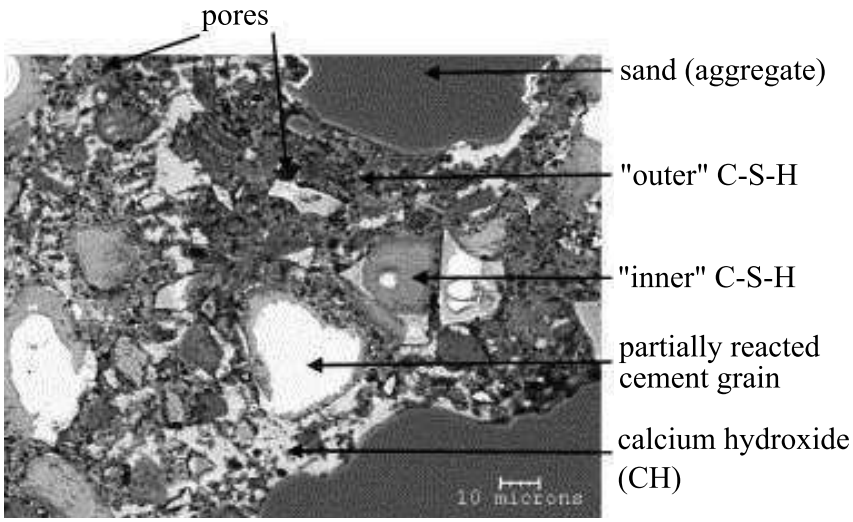

Figure 1.1: Typical BSE image of a Portland cement mortar (200 days old, w/c=0.4), with the microstructural constituents distinguished (Scrivener [57])

Aggregates

Aggregates make up a substantial part of the total volume of concrete (70 to 80 %) and naturally affect its properties in both fresh and hardened states. Originally, aggregates, much cheaper than cement, were considered as an inner material used for economic reasons. However, in addition to the lower cost, reducing the amount of cement paste provides considerable technical advantages, as the paste component is responsible for heat generation, shrinkage, creep and many durability problems.

Usually, two size groups of aggregates are used in concrete: coarse aggregates and fine aggregate. The European Standard classifies aggregates over 4 mm as coarse aggregates. The particles less than or equal to 4 mm in size are referred to as fine aggregates, often called sand. The particle size distribution within these two groups is defined by grading curves. Grading of the aggregates does not affect directly the strength of fully compacted concrete (Neville [46]). However, well-graded aggregate skeleton provides sufficiently workable mix and allows its compaction to the maximum density.

All natural aggregates originally formed a part of a larger parent mass. Its fragmentation is either a natural processes of weathering and abrasion, resulting in sand and gravel deposits, or a manufactured crushing. The type of formation process influences some of the features of natural aggregates, such as particle size and shape, surface texture and absorption. On the other hand, many properties of the aggregate depend entirely on the properties of the parent rock: chemical and mineral composition, specific gravity, hardness, strength, physical and chemical stability, porosity. All these various characteristics may have a considerable influence on the performance of concrete.

Porosity

There exist four types of pores in concrete: gel pores, capillary pores, entrained air and

entrapped air voids - referred to as macroporosity. As previously mentioned, gel porosity and capillary porosity are formed in the cement paste during the hydration process.
Gel pores are the interconnected interstitial spaces between the C-S-H gel particles characterized by a nominal diameter of about 2 nanometers. Their volume, independent of the progress of hydration, is characteristic for given cement (Neville [46]).
Capillary pores are the remaining water-filled space between solid phases. Their volume in hardened concrete thus depends on the water/cement ratio in concrete mix. Capillary pores generally range from about 0.01 to 0.1 micrometers in size and form an interconnected system randomly distributed throughout the cement paste (Verbeck [62]).
The entrapped air found in concrete is a result of the cement paste inability to join with the aggregates. It is formed in concrete during mixing, primarily because of inadequate consolidation. The entrapped air voids are characterized by the non-spherical shape and an important size (usually larger than 1 mm). In addition, air entrained concrete contains tiny air bubbles, introduced by the use of air-entraining cement or by the addition of an air-entrainment agent. The entrained air bubbles are smaller and more uniformly distributed than the entrapped air voids. The volume of all voids in concrete, as well as their distribution and type has a significant effect on the performance and durability of the material.

1.1.2 Interfacial transition zone

Concrete is often presented as a two-phase composite material. However, the cement paste in concrete cannot be considered as a homogeneous phase. The mesostructure of the cement paste is modified in the vicinity of the aggregate particles. This region, called the interfacial transition zone (ITZ), plays an important role in concrete behavior. As reported by Scrivener *et al.* [56], the origin of the ITZ lies in the so-called "wall" effect in the cement grains packing against much larger aggregates, schematically presented in Figure 1.2. A flat solid object placed at random in an assembly of cement grains would cut through grains. As this is impossible, the packing of grains is disrupted to give a zone of higher porosity and smaller grains in the zone close to the "aggregate" that leads to an increase in porosity and predominance of smaller cement particles in this region.

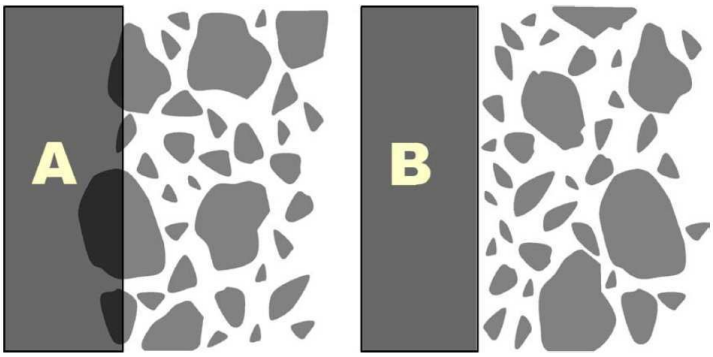

Figure 1.2: Illustration of the "wall" effect at the origin of the ITZ (Scrivener *et al.* [56])

The same author characterized the microstructural features of the ITZ by analysis

of backscattered electron images of concrete samples. Figure 1.3 displays the evolution of average porosity and of the distribution of unhydrated cement grains in the ITZ at various concrete ages. The effective width of the ITZ depends on the microstructural feature being considered and on the degree of hydration. The initial packing leads to high porosity zone of about 15 to 20 μm width. The deposition of hydration products over time leads to the densification of the zone, but even in mature paste the ITZ exhibits a significantly higher porosity than the "bulk" paste.

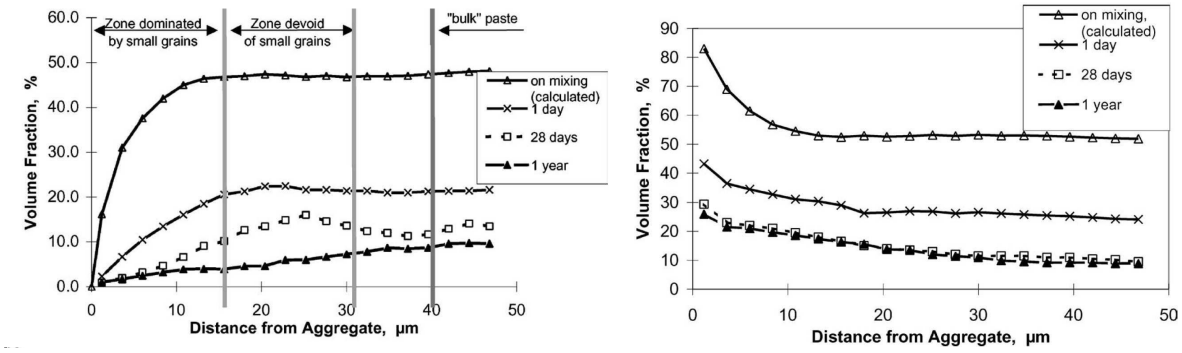

Figure 1.3: Characterization of some features of the ITZ in concrete at various ages (Scrivener *et al.* [56]):
(a) Distribution of unhydrated cement
(b) Average porosity

1.1.3 Recent techniques to characterize concrete heterogeneity

We have seen that concrete is a heterogeneous material with heterogeneities over very wide range of length scales, from nanometers, in the pore structure of the hydrates, to centimeters corresponding to the largest aggregates. Characterization of this complex, heterogeneous nature provides many interesting experimental challenges. Previously mentioned backscattered electron imaging of polished surfaces has become well-established method in the study of cement and concrete microstructures. However, this technique allows imaging only a two-dimensional section of a three-dimensional structure. Recently widely developed in material science, X-ray microtomography overcomes this limitation and provides relatively high resolution 3D images of the material.

X-ray microtomography is a non-destructive, 3D imaging technique that uses a series of radiographs to mathematically reconstruct a 3D map of the object X-ray absorption. This method is similar to the classical X-ray computed tomography except that allows much higher spatial resolution by combining extremely bright, monochromatic synchrotron radiation with high quality optics and X-ray detection.

Lu *et al.* [40] employed the X-ray microtomography to characterize the pore structure in concrete. The purpose of their work was to link the microstructural features with the chloride permeability in concrete. The pore network of four different concretes, the reference concrete and three modified concretes (admixtures: fly ash, silica fume, slag),

were characterized by size distribution and connectivity. No pore connectivity was found at a resolvable pore diameter of 1 μm. However, due to this limited resolution of the images, the authors were not able to make definite conclusions on the pore space connectivity. Therefore, the "disconnected pore space" defined as a maximum distance between the pore network connected to the top of the sample and the pore network connected to the bottom of the sample was used. The results proved a good correlation between this parameter and standard chloride permeability tests, which is an increase in the disconnected pore distance with a decrease of the permeability. The ongoing improvements in synchrotron-based microtomography may allow in the future to directly relate pore connectivity and transport properties.

Another interesting application of this technique was made by Burlion *et al.* [7]. This time, the microstructure analyses were performed on mortar samples subjected to a chemical attack. The porosity evolution due to leaching of cement was studied. Leaching is a process by which a liquid dissolves and removes the soluble components of the material. In concrete it is often caused by the hydrolysis of cement paste hydrates in pure water or in water with very low pH compared that of the pore fluid. It leads to an important increase of porosity. The authors analyzed different leaching states during a chemically-accelerated test that is able to reproduce the long-term behavior. Figure 1.4 presents a cross section of the sample after 24 hours of leaching. The sound zone as well as two different leached zones are distinguished. In order to determine the evolution of the calcium content in solid phase and the increase in porosity during leaching, the absorption coefficient of the cement paste was measured at various locations in the sample. The variations of this coefficient with respect to the time and the radius of the considered zone are displayed in Figure 1.4(b). The analysis of the results showed the ability of the applied method to evaluate the porosity increase due to the leaching of the cement paste.

X-ray tomography was applied by different authors to study the mechanical damage of concrete. Wong and Chau [68] investigated damage mechanisms under simple compression, in both ordinary and high performance concrete. We can cite also the work of Elaqra *et al.* [24], who used X-ray tomography and acoustic emission to study the mechanisms of damage and the fracture process during compressive loading on mortar specimens, or Landis *et al.* [38], who studied *in situ* (scanning during the test) the crack growth in mortar samples under compressive loading.

X-ray computed tomography can be employed to determine the shape of coarse aggregates used in concrete. Obtaining precise numerical information on the aggregate shape is not a simple but very interesting issue, important to realistically model and to predict the properties of concrete. Garboczi [31] used 3D tomographic images of aggregate particles to perform mathematical shape analysis using spherical harmonic functions. Therefore, the first aspect of this work concerns the acquisition of a 3D geometry of each aggregate. Two requirements are important to obtain correct shape data: aggregates should not touch spatially and embedding matrix material needs to differ significantly in X-ray absorption characteristics from the aggregates. In this preliminary work, the aggregate images were taken on real concrete samples and some image processing techniques were applied to extract individual particles. Figure 1.5 presents a final binary image of a portion of the concrete sample. Once aggregate particle was isolated, their voxels coordinates were used to generate a 3D surface function written as a series of spherical harmonic functions.

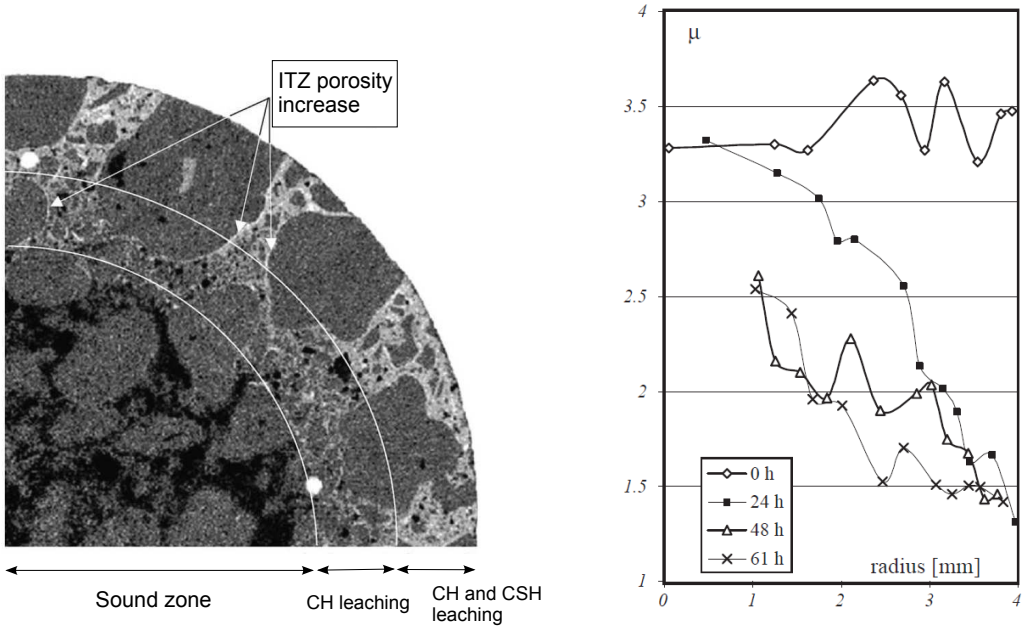

(a) (b)

Figure 1.4: Evolution of mortar microstructure during the leaching process (Burlion *et al.* [7]):
(a) Tomographic image of the part of the sample cross-section after 24 hours of leaching (negative view)
(b) Variations of absorption coefficient μ in the cement paste at different leaching stages vs. the radius of the considered zone

The number of spherical harmonic coefficients determines the particle shape complexity. Figure 1.6, extracted from the successive work (Erdogan *et al.* [25]), displays a series of 2D images taken from the particle reconstruction using different number of coefficients and a digital image of the real rock and proves a good ability of the proposed method to reproduce aggregate shapes.

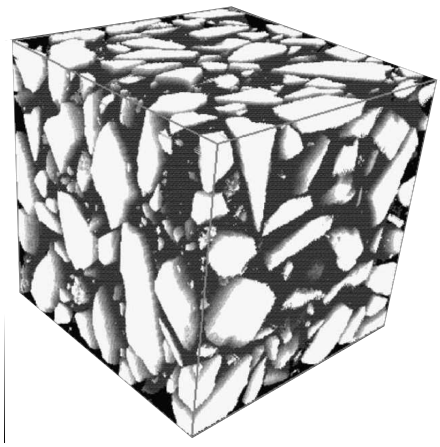

Figure 1.5: A part of a tomographic image of a concrete material (Garboczi [31])

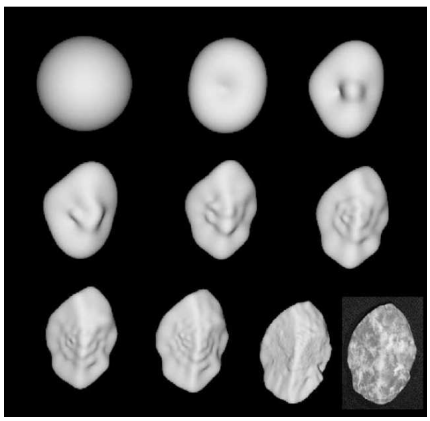

Figure 1.6: 2D images taken from the particle reconstruction of the reference rock. The final image on the bottom right is a digital camera image of the real rock in the same orientation (Erdogan *et al.* [25]).

1.2 Behavior of concrete under high triaxial loading

1.2.1 Material compaction

The compaction process, typical for mortar and concrete submitted to high mean stress level, is generated by two parallel phenomena: progressive damage of the cement matrix structure and porosity closure. Many authors studied this subject on mortar samples. Smaller size of the material heterogeneities allows testing smaller specimens and thus avoiding technical limitations in reaching high stress levels.
Burlion [6] investigated the compaction behavior of mortar with different water/cement ratios under hydrostatic compression test and oedometric test. The volumetric curves corresponding to mortar with W/C ratio equal 0.5 are presented in Figure 1.7. Three phases of the material behavior submitted to the hydrostatic compression can be easily distinguished: a short linear phase is followed by a progressive reduction of the tangent stiffness and a subsequent stiffening of the material at high mean stress level. It is interesting to compare the difference between volume changes during hydrostatic and oedometric tests. At the same level of the mean stress, the volumetric strain is higher for the sample under oedometric compression than under hydrostatic loading. Therefore, the presence of deviatoric stress facilitates compaction of mortar. This phenomenon is attributed to the coupling of the behavior of cement matrix and rearrangement of the granular skeleton during the test. Deviatoric stress generates a rearrangement of grain particles within the material, restrained under hydrostatic loading, what produces additional volumetric strains.

Coherent results were found by Gabet *et al.* [30] for an ordinary concrete R30A7. The composition of this concrete, used as a reference concrete in the study concerned by this report, is detailed in section 2.2.1. Comparison of volumetric behavior under hydrostatic and oedometric compression presented in Figure 1.8 shows the evolution of the tangent

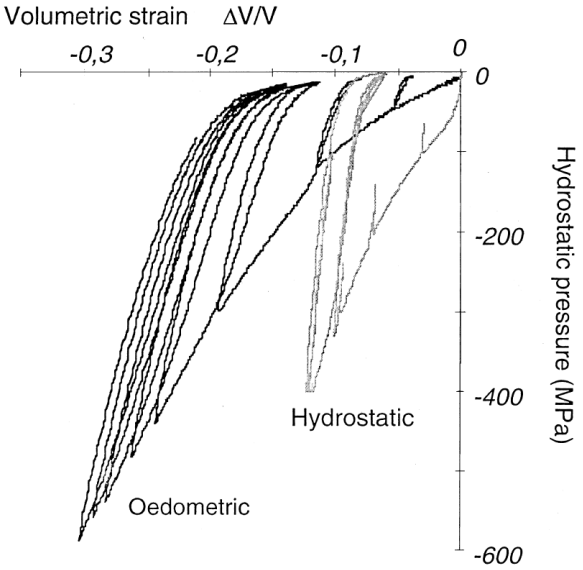

Figure 1.7: Results of hydrostatic and oedometric tests performed on mortar with W/C = 0.5 (Burlion [6]): mean stress σ_m vs. volumetric strain ε_v

stiffness similar to the one observed for mortar as well as the influence of the deviatoric stress on the material compaction.
It is worth to mention that unloading-reloading cycles do not cause any additional damage of the material. Moreover, the reloading behavior is practically identical to the preceding unloading when the viscous effects are eliminated. It is done by holding the maximum stress constant during a certain time interval in order to allow the material to creep, before each unloading (as done for example by Schmidt *et al.* [55]).

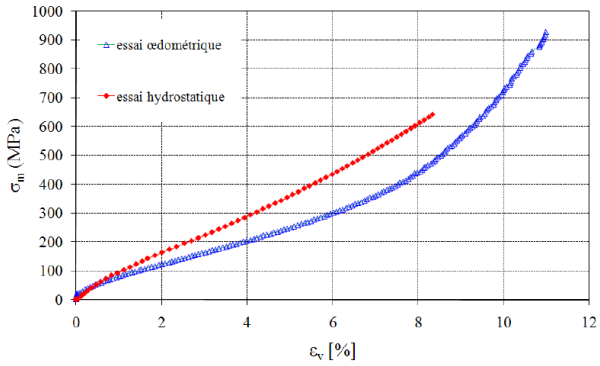

Figure 1.8: Results of hydrostatic and oedometric tests performed by Gabet on concrete with W/C = 0.64: mean stress σ_m vs. volumetric strain ε_v

The compactant behavior of the cement matrix materials depends on the loading path and on the material composition, however the same trend, schematically presented in Figure 1.9 is always followed. At the beginning of the test behavior is linear elastic. Be-

yond the elastic limit, the material undergoes plastic deformation which corresponds to the simultaneous damage the cement matrix and porosity closure. Initially, the cement matrix damage is predominant on the material densification, reduction of the tangent stiffness is then observed. As the mean stress increases, the effect of the closure of porosity becomes predominant what results in the stiffening of the material response until full consolidation is reached. This consolidation state requires very high stress level (probably a few GPa), that was, to the best of my knowledge, never reached experimentally. Performing unloading-reloading cycles allow better understanding of the material behavior (Fig. 1.10(a)). Beyond the elastic yield stress, the unloading phase may be divided in two parts: quasi-elastic part followed by the non-linear part with stiffness tending to zero at the end of unloading. The decrease of the unloading stiffness is attributed to the opening of cracks that was before inhibited by the confinement. In addition, the evolution of the unloading curve with the increase of confinement is characterized by an increase of the elastic stiffness and the strengthening of the following non-linearity. Figure 1.10(b) displays the evolution of the bulk elastic modulus corresponding to the linear part of the unloading cycle during hydrostatic compression at 600 MPa, performed by Poinard [49]. The value of elastic modulus increases monotically with pressure. This increase is significant up to confining pressure of 150 MPa, when the cement matrix becomes strongly damaged. Beyond this point, the increase of unloading modulus is very limited.

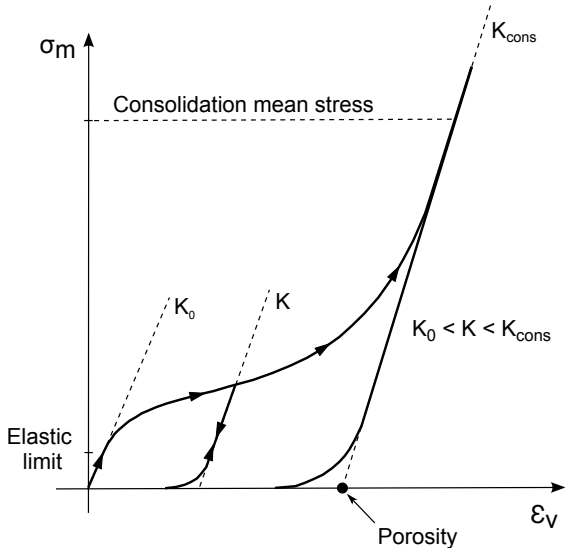

Figure 1.9: Schematic representation of mortar compaction: mean stress σ_m vs. volumetric strain ε_v

Cement matrix damage induced by the hydrostatic compression substantially diminishes uniaxial mechanical properties of concrete. Yang Ke (work not published yet) performed simple compression tests on concrete R30A7 loaded primarily under hydrostatic pressure of 650 MPa - 700 MPa. Figure 1.11(a) displays the axial behavior of two preconsolidated concretes, with different water/cement ratio, in comparison with concretes with the same composition but never tested before. The corresponding images of the samples are presented in figures 1.11(b) and 1.11(c). Strong decrease of the material

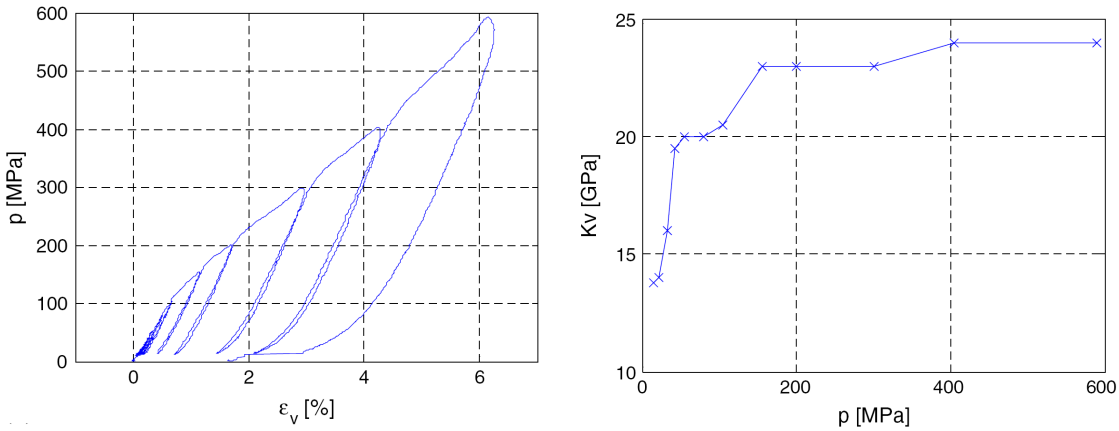

(a) (b)

Figure 1.10: Results of hydrostatic compression at 600 MPa conducted on a concrete sample (Poinard [49]):
(a) mean stress σ_m vs. volumetric strain ε_v
(b) bulk elastic modulus in unloading K_v vs. confining pressure p

strength and the Young's modulus for pre-consolidated concretes confirms an important loss of cohesion by the cement matrix under hydrostatic compression.

1.2.2 Triaxial behavior of concrete

Different studies on concrete triaxial behavior revealed the increase of concrete strength with the confinement and the transition from quasi-brittle to ductile behavior (Jamet *et al.* [36], Schmidt *et al.* [55]). At low confinement, a peak stress is observed, accompanied by a change in volumetric behavior from contraction to dilation. Under high confinement, a plateau stress or hardening behavior is observed with the material limit state characterized again by the contractancy-dilatancy transition. Figure 1.12(b) representing the results of Sfer *et al.* [58] points out these effects. Besides, the study of Sfer covers the development of failure patterns in concrete samples tested under confinement up to 60 MPa. The review presented in Figure 1.12(a) indicates a change in the failure mechanism with the increase of the confining pressure, from distributed cracking to few macrocracks that separate the specimen into two or three parts, accompanied by the considerable microcracking within the aggregates. These observations were completed by Gabet [29] and Vu [63] for higher confinement levels. The summary of failure patterns under confining pressure varying from 0 to 400 MPa is shown in Figure 1.13. For the confining pressure of 50 MPa, the results are coherent with the ones obtained by Sfer. At higher pressure levels, one ore several cracks perpendicular to the loading axis are observed. This behavior is strongly different to the behavior of mortar, characterized by the absence of microcracks under high confinement (Fig. 1.14), and thus underline the effect of coarse aggregates on the damage features.

These observations were completed by the tomographic analysis of samples tested at moderate and very high confinement carried out by Poinard *et al.* [50]. Tomographic

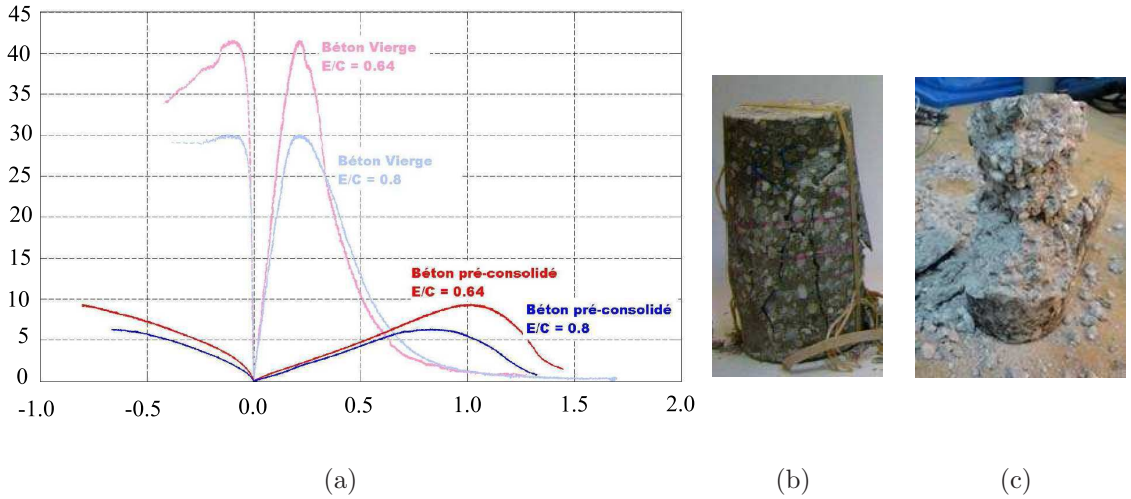

(a) (b) (c)

Figure 1.11: Comparison of simple compression tests performed on the reference concrete and on the pre-consolidated concrete:
(a) axial stress σ_x vs. strain components ε_x and ε_θ
(b) picture of the reference concrete sample after simple compression test
(c) picture of the pre-consolidated concrete sample after simple compression test

scans were performed after increasing loading-unloading cycles, to study the evolution of the mesostructural damage of concrete. Different damage phenomena were observed during triaxial compression at 50 MPa and 650 MPa of confinement. Under very high confinement (Fig. 1.15), mesostructural damage manifests itself over the entire specimen in the entrapped porosity closure, initiated in the hydrostatic part of the loading, and aggregates debonding and cracking. Material undergoes strong compaction before reaching the limit states. As the loading cycles progress, concrete reaches a maximum compaction state, which leads to extensive granular rearrangement and hence to dilative behavior. After the last unloading, horizontal cracks are produced. At 50 MPa of confining pressure (Fig. 1.16), the application of shear loading creates a localized microscopic damage, the growth of which leads to a failure on a sliding plane inclined at 60°. Outside the failure zone, concrete remains undamaged at the mesoscopic scale.

Another aspect of the triaxial behavior of concrete is the evolution of its elastic unloading characteristics. Poinard *et al.* [49] performed triaxial tests at confining pressures varying from 0 to 400MPa with several unloading-reloading cycles in order to better understand damage mechanisms of concrete. Figure 1.17 indicates how the elastic modulus and the Poisson's ratio change as the triaxial compression proceeds. At low confinement, a strong decrease in axial stiffness coupled with a rise of Poisson's ratio is observed, what is generated by the localized damage and loss of strain homogeneity. Contrarily, under high confinement, evolution of elastic characteristics during unloading becomes less important. Failure is thus associated with diffuse material damage leading to dilatant behavior without reaching a peak stress.

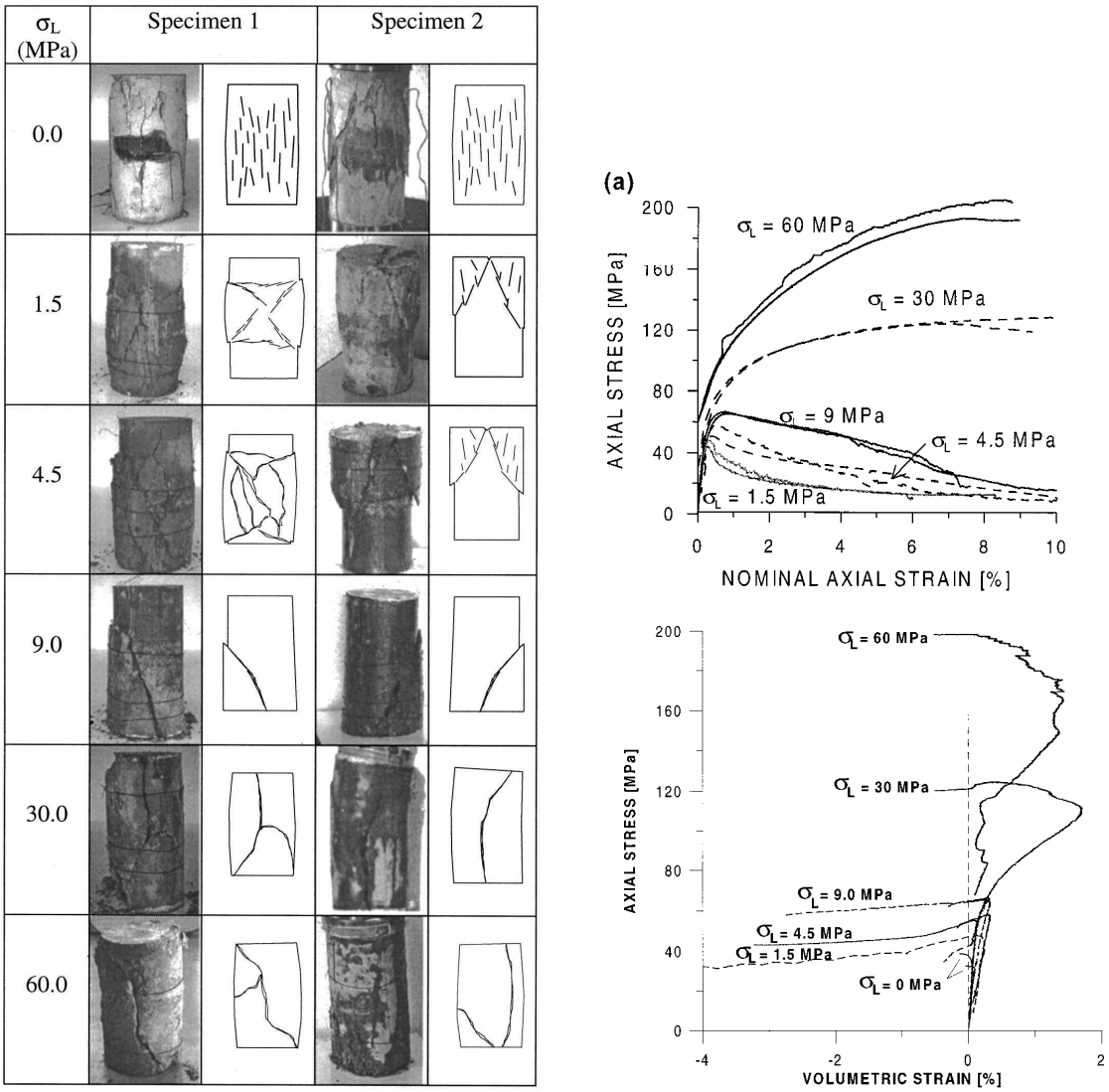

Figure 1.12: Results of triaxial tests conducted on concrete samples at low level of confinement (Sfer *et al.* [58])
(a) Failure patterns
(b) Axial and volumetric behavior

Figure 1.13: Failure patterns of concrete under triaxial compression at different levels of confinement (Vu [63])

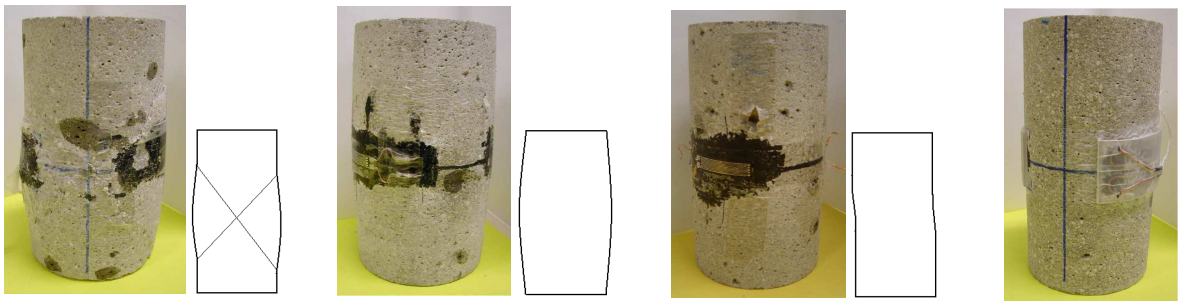

(a) p = 60 MPa (b) p = 120 MPa (c) p = 300 MPa (d) p = 650 MPa

Figure 1.14: Failure patterns of mortar under triaxial compression at different levels of confinement (Dupray [22])

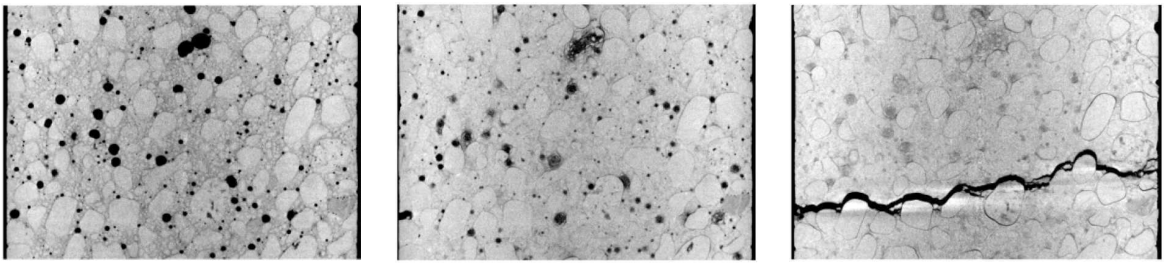

(a) undammaged (b) hydrostatic at 650 MPa (c) last triaxial cycle

Figure 1.15: Vertical slice of a concrete specimen tested under triaxial compression at 650 MPa of confinement (Poinard *et al.* [50])

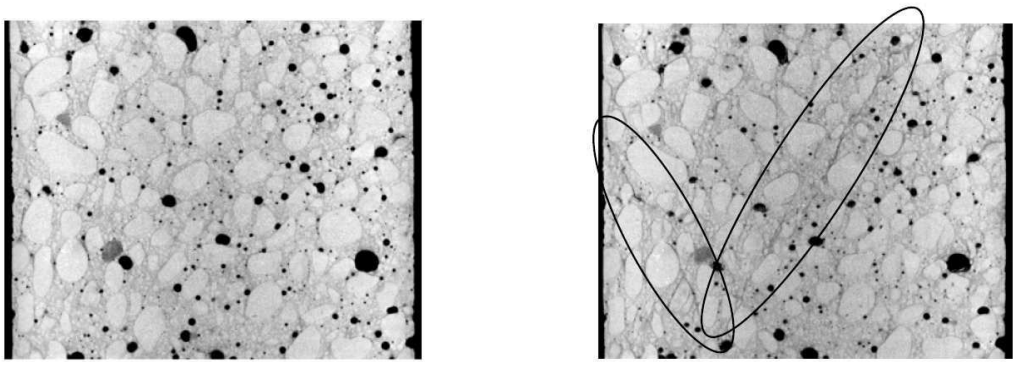

(a) undammaged (b) last triaxial cycle

Figure 1.16: Vertical slice of a concrete specimen tested under triaxial compression at 50 MPa of confinement (Poinard *et al.* [50])

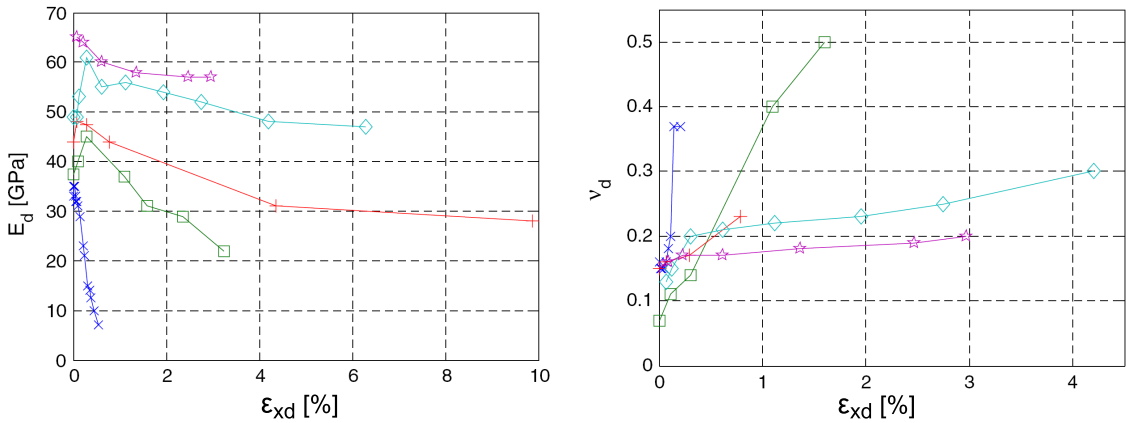

(a) elastic stiffnes (b) Poisson's ratio

Figure 1.17: Evolution in unloading properties of concrete with deviatoric axial strain at various confining pressures: (×) 0 MPa, (□) 20 MPa, (+) 50 MPa, (◊) 200 MPa, (⋆) 400 MPa (Poinard *et al.* [49])

Finally, it is interesting to look at the limit states of concrete tested under triaxial compression. The comparison of stress limit states (maximum deviatoric stress reached) of different concretes characterized by the uniaxial strength between 34 and 140 MPa, done by Buzaud [8], is presented in Figure 1.18. The increase of maximum deviatoric stress with the mean stress is observed. However, this effect is less pronounced at higher mean stress. These experimental results reveal that at low confinement the uniaxial strength affects the maximum deviatoric stress. This relation vanishes at high pressures. It is thus impossible to correlate the simple compression strength of the material with its stress limit state at high confinement.

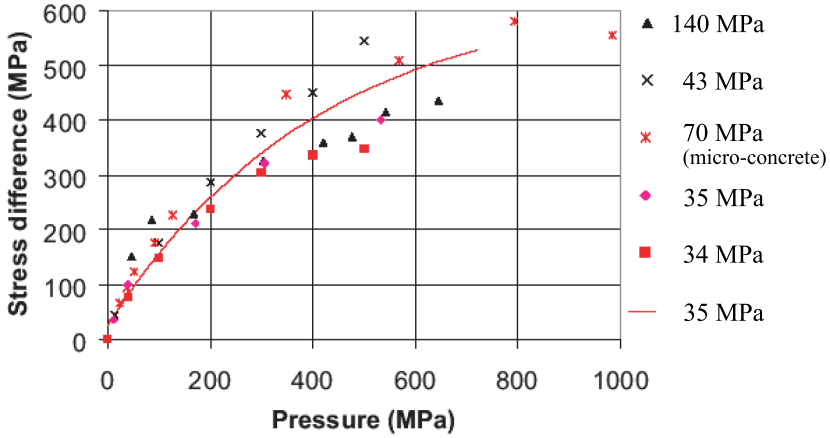

Figure 1.18: Comparison of stress limit-states of different concretes tested under triaxial compression (Buzaud [8]): deviatoric stress vs. mean stress

1.2.3 Influence of the concrete composition on the mechanical behavior

The relative influence of the coarse aggregates and of the cement matrix on the behavior of concrete considered as a combination of these two homogeneous materials was investigated by Akers and Phillips [3]. The author performed experimental tests on mortar, rock and concrete under different loading paths: simple compression, hydrostatic compression up to 500 MPa and triaxial compression at 300 MPa of confinement. Figure 1.19 compares the volumetric behavior of the three materials. Under hydrostatic loading, the rock exhibits very stiff linear elastic behavior strongly contrasting with the compactant behavior of two other materials. Therefore, the behavior of concrete affected by the one of aggregates is considerably stiffer than the one of mortar. The comparison of the results of uniaxial and triaxial compression presented in Figure 1.20 indicates strongly higher strength and stiffness of the rock than of the concrete and mortar. However, the ratio between rock strength and concrete strength decreases considerably from 5.8 for simple compression to 1.2 for triaxial compression. The behavior of mortar and concrete are relatively close with and without the confining pressure. Nonetheless, beyond a given strain level concrete exhibits plastic-hardening behavior, similarly to the rock, while slight softening is observed for mortar.

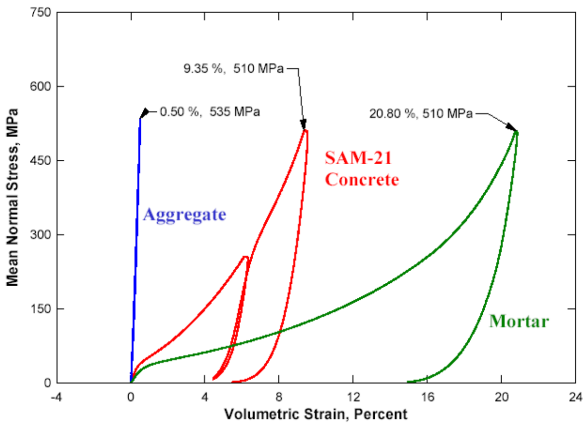

Figure 1.19: Volumetric behavior of rock, mortar and concrete: mean stress σ_m vs. volumetric strain ε_v (Akers and Phillips [3])

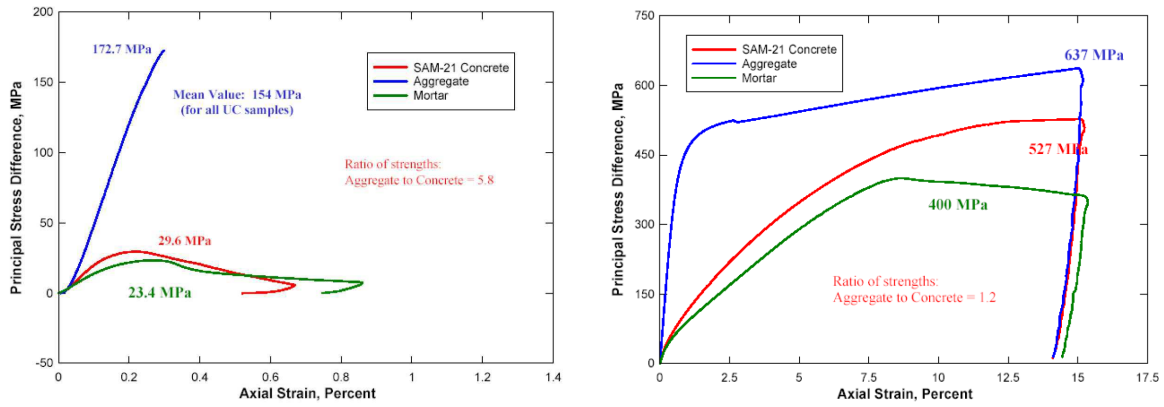

(a) (b)

Figure 1.20: Deviatoric behavior of rock, mortar and concrete: stress deviator q vs. axial strain ε_x (Akers [3])
(a) Simple compression test
(b) Triaxial compression at 300 MPa of confinement

1.2.3.1 Water/cement ratio

Uniaxial behavior of ordinary concrete is strongly controlled by the properties of the cement paste. The strength of the latter depends on the mass proportions of water and cement used in the mixture. Moreover, the cement paste composition strongly affects the porosity of the cement matrix within the hardened concrete, which is also related to the material compaction ability. Thus the influence of the W/C ratio on the concrete behavior is important in terms of concrete durability and vulnerability. The decrease of concrete strength in simple compression with higher water/cement ratio was reported by Neville [46]. A large experimental campaign was recently performed by Vu *et al.* [66] on concretes with different water/cement ratios under a wide range of triaxial loading. It was observed that regardless of the W/C ratio, the confinement strongly increases both ductility and loading capacity of concrete. Nevertheless, a drop in W/C ratio raises the confinement threshold corresponding to the brittle-ductile behavior transition. Furthermore, the compaction of concrete increases with the W/C ratio, particularly at low confinement levels. The volumetric strain of concrete is thus directly correlated with its porosity. Conversely, under high confinement, once the cement matrix has been strongly damaged and compacted, the volumetric and deviatoric behavior of concrete become both insensitive to the W/C ratio (Fig. 1.21).

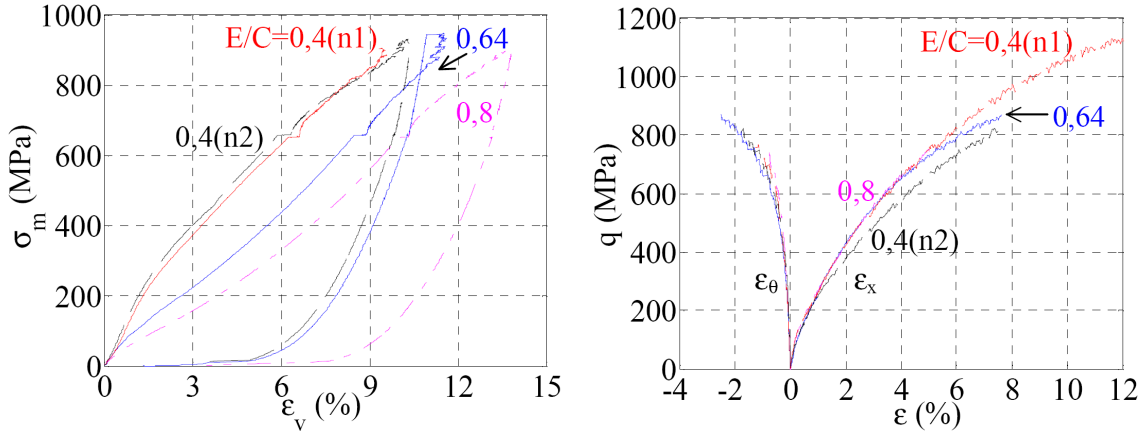

(a) (b)

Figure 1.21: Triaxial test at 650 MPa of confinement on concretes with W/C = 0.8, W/C = 0.64 and W/C = 0.4 (Vu [63]);
(a) mean stress σ_m vs. volumetric strain ε_v
(b) stress deviator q vs. strain components ε_x and ε_θ

1.2.3.2 Saturation ratio

Concrete porosity can be partially or fully filled with water. Triaxial behavior of concrete with respect to the saturation ratio was studied by Vu *et al.* [67]. Experimental tests performed at wide range of confining pressures revealed that the behavior of ordinary concrete is slightly dependent on the saturation ratio at low level of confinement. Only small variations of stiffness and strength were observed. In contrast, at high mean stresses, the presence of free water takes a major importance. Hydrostatic behavior of very wet and fully saturated concrete is significantly stiffer than that of dry concrete. Moreover, the shear strength of saturated concrete is limited to a maximum value, independently of confining pressure (see Fig. 1.22).

1.2.3.3 Cement paste volume and coarse aggregates size

In the same research framework, Vu *et al.* [64] investigated the effect of cement paste volume and coarse aggregate size on concrete behavior under triaxial compression. Tests performed on three concretes mixes with different cement paste volumes revealed that at low confinement, the concrete strength significantly increases with an increase in cement matrix volume. This effect is reduced as the confining pressure increases and at very high confinement, the cement paste volume has only a slight influence on concrete deviatoric behavior. Besides, the increase of concrete deformation capacity with the decrease of the cement paste volume was observed. The effect of coarse aggregate grading was studied on three concretes with different maximum aggregate size. Slight influence of the coarse aggregate size on concrete deviatoric behavior at confinement levels varying from 0 MPa to 650 MPa was observed. The concrete strength is somewhat higher for greater aggregate size distribution. On the contrary, coarse aggregate size has a significant

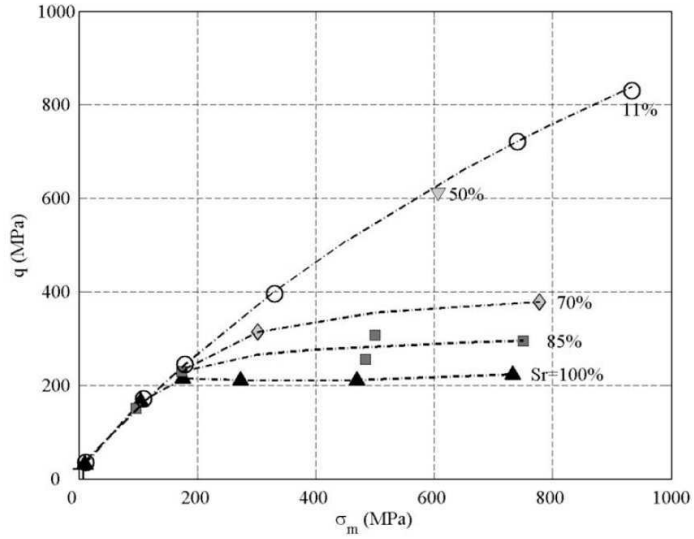

Figure 1.22: Stain limit states of concretes with different saturation ratios (Sr): deviatoric stress q vs. mean stress σ_m; (○) dried concrete, (+) Sr = 42%, (▽) Sr = 50%, (◆) Sr = 70%, (■) Sr = 85%, (▲) Sr = 100% (Vu *et al.* [67])

effect on concrete strain limit state. Higher coarse aggregate size results in lower mean stress level corresponding to concrete strain limit state which means lower deformation ability of concrete.

1.2.3.4 Coarse aggregates type

Other factors influencing the behavior of concrete are properties of coarse aggregates such as shape, surface texture, strength and stiffness. Many experimental studies have examined these effects under uniaxial loading, especially on high performance concrete *e.g.* [2, 70, 5], making evidence that the influence of the type of coarse aggregates on the strength properties of concrete varies in magnitude and depends on the water/cement ratio of the mix. The effect of the coarse aggregates type on the strength of concrete is more important for high strength concrete, *i.e.* concrete with low water/cement ratio and high cement content, what was pointed out, among others, by Ezeldin and Aitcin [27], Özturan and Çeçen [47] and de Larrard and Belloc [19]. Crushed aggregates with rough surface texture and high strength produce noticeably higher compressive and splitting tensile strengths for high strength concretes whereas their effect is limited for ordinary concretes. On the contrary, the use of limestone aggregates, which are quite weak, may produce relatively higher strength of the ordinary concrete (Neville [46]). This effect is attributed to the interfacial chemical reactions between the cement paste and the aggregate particles. In addition, high absorption of these aggregates may lead to a densification of the interfacial transition zone and thus to enhancement of its properties. Giacchio and Zerbino [33] investigated fracture mechanisms in conventional and high strength concretes which exhibit differences in shape and interface bond strength. Failure mechanisms, *i.e.* debonding or cracking through aggregates, differ for rolled, smooth aggregates, very angular and strong crushed aggregates or crushed but softer and less angular particles. These

variations are dependent on the cement matrix strength as well. These are some issues concerning this complex problem, which has been widely studied under uniaxial loading conditions. To the best of my knowledge, no similar study exists for triaxial behavior of concrete.

1.3 Mesoscopic modeling of concrete

Variety of heterogeneities in concrete and the complexity of its non-linear behavior result in multiscale modeling of concrete. Mesoscopic modeling (length scale of 10^{-3}m) may be a powerful tool for understanding and predicting the macroscopic behavior of concrete. It should be noted that the meso-scale description of concrete differs from one author to another. It may refer to a biphasic representation, that is cement matrix (cement paste and fine aggregates) and large aggregates with or without the existence of the interfacial transition zone. Another possibility is to introduce the macroporosity as a third phase of the material. Meso-scale models allow better estimation and understanding of the local mechanisms of deformation, (taking into account) highlighting the damage initiation and propagation. They enable parametric studies on different concrete compositions as well.
The first model present in the literature taking into account the mesostructure of concrete was proposed by Roelfstra *et al.* [51]. This was followed by a variety of models and approaches, most of the time developed in 2D due to high computational cost. However, thanks to the increasing computing power, more and more models are formulated in 3D.

1.3.1 Continuum models

Mesoscopic analysis of concrete can be performed using continuum mechanics based methods. The mesostructural components of concrete are modeled as a continuum using finite elements. In order to deal with the propagation of various discontinuities mesh refinements or joints elements are often introduced.

Caballero *et al.* [9] modeled concrete as large aggregates embedded in a matrix representing mortar and smaller aggregates, using a polyhedral geometry generated by standard Voronoï/Dalunay tessellation. Both continuum type components were assumed to be linear elastic. The non-linearity and failure were provided by the use of zero-thickness interface elements equipped with a non-linear fracture law. Interface elements were inserted along the potential fracture surfaces in the mesh before the simulation. An example of interface elements placed around the polyhedral aggregates and inside the matrix is presented in Figure 1.23. The proposed model provides realistic representation of the stress-strain curves and of the crack patterns under uniaxial tension and compression. The validity of the model was also confirmed under biaxial loading.

An interesting work has been done by Comby-Peyrot *et al.* [14], who proposed a 3D finite element model to investigate the mechanical consequences of the chemical degradation of concrete. Concrete was modeled as a biphasic material characterized by a realistic distribution of aggregate particles. A nonlocal version of damage model (Mazars [41]) was used to simulate the behavior of mortar while aggregates were assumed purely elastic. The contact between mortar and aggregates was considered as bilateral sticking. To take into

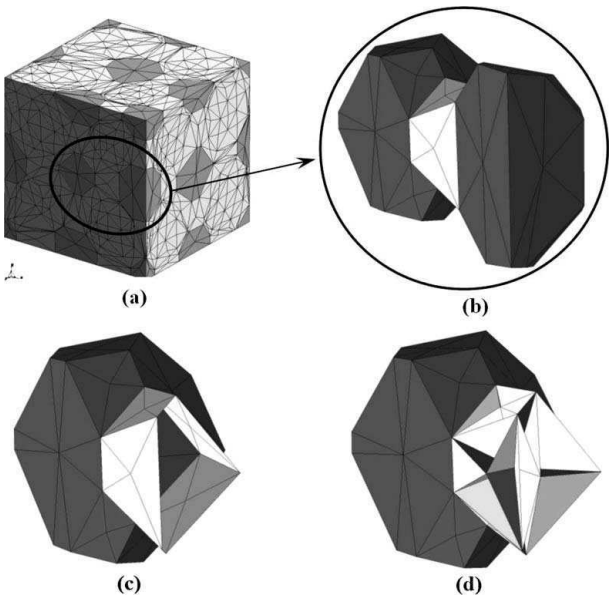

Figure 1.23: Inserting joint process: (a) exterior geometry, (b) zoom of two example aggregates, (c) interfaces between parallel edges of two opposite polyhedra and (d) interface among the space between two different polyhedra (Caballero *et al.* [10])

account the interfacial transition zone and microcracking due to shrinkage phenomenon, the damage model parameters were identified on the experiments performed on concrete. The model was applied to the alkali-silica reaction in concrete that is characterized at the meso-scale by a swelling of the granular skeleton. Thus, the constitutive equations were modified to take into account the pressure generated by the swelling aggregates. This pressure was proportional to the reaction advancement corresponding to volume variations of grains identified experimentally. The proposed model reproduces crack patterns and a progressive loss of material stiffness quite accurately.

Mesoscopic finite element models of concrete were also employed for example by Wriggers and Moftah [69] for unconfined compression tests, by Dupray *et al.* [23] to simulate the behavior of concrete under high triaxial loading and by Erzar et Forquin [26] to simulate dynamic behavior of concrete under impact.

At the end, it is interesting to mention a relatively new approach developed by Belytschko and coworkers [42] to model crack propagation in the finite element framework, called extended finite element method (XFEM). This approach was recently used by Du Min *et al.* [21] to study the effect of coarse aggregate distribution on concrete failure under uniaxial tension.

1.3.2 Discrete models

An alternative approach to continuum models is discrete modeling which relies on a discrete description of the material what provides an explicit representation of material discontinuities. The discrete element approach based on a particle representation of the mechanical system, called Discrete (or Distinct) Element Method (DEM) was initiated

in geomechanics by Cundall & Strack in 1979 [16]. The method consists in replacing the granular medium by an assembly of circular non-deformable particles interacting with each other through contact points. Particles have both translational and rotational degrees of freedom. The interaction forces are computed using Hook's law in the normal direction and elasto-plastic law with Coulomb criterion in the perpendicular direction. The governing equation is the Newton's second law of motion which is integrated using an explicit scheme. Since then, this initial formulation was largely enhanced and new methods within the discrete element framework were proposed.

A 2D DEM based particle model was used by Monteiro Azevedo *et al.* [44] to study fracture process in concrete under uniaxial tension and compression (see figures 1.24 1.25). The authors investigated the behavior of particle assemblies with different deformation and contact properties. The aggregates were considered either as rigid macro-particles or as deformable group of particles. Two types of inter-particle contact models were used. Simple brittle Mohr-Coulomb model, where the contact breaks when the tensile or shear force exceeds its maximum value, was compared with the extended Mohr-Coulomb model with bilinear softening. The effect of pure friction contacts working in compression, which are either previously broken contacts or newly detected contacts, was examined as well. The advantages of the consideration of aggregate deformability seem to be incommensurate with the computational savings while using rigid aggregates. The implementation of the softening increases the capacity of loading redistribution inside the particle assembly and affects the crack formation and growth. It has been shown that softening provides more ductile behavior in tension while the consideration of pure friction contacts increases the fracture energy under compressive loading. The high influence of pure friction contacts on to the crack formation was also revealed.

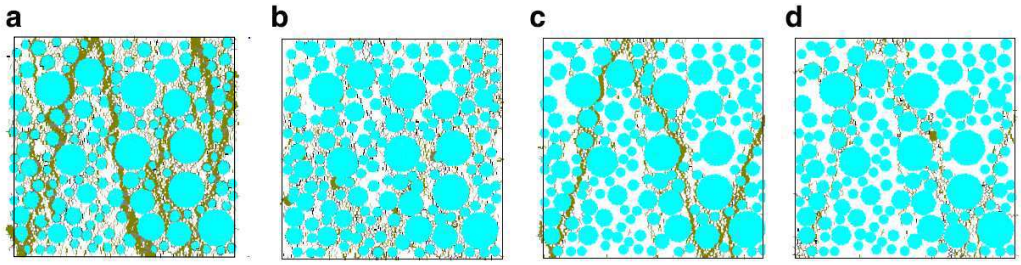

Figure 1.24: Compression, final crack pattern: rigid aggregate. (a) Brittle F, (b) Brittle NF, (c) Soft. F and (d) Soft. NF (Moneiro Azevedo *et al.* [44]); F/NF - with/without pure friction contacts

Fracture process in brittle materials was also studied a lot with the lattice models that are conceptionally very simple. In this kind of models medium is discretized as a network of beams transferring normal forces, shear forces and bending moments, usually assumed linear elastic up to a brittle failure when the bar elements are removed. The failure criterion is a limit condition related to the strength. The material heterogeneity is implemented by assigning different properties to beams.

The first lattice model applied to concrete was proposed by Schlagen and van Mier [54]. The heterogeneity was taken into account using a normal distribution of bar strength

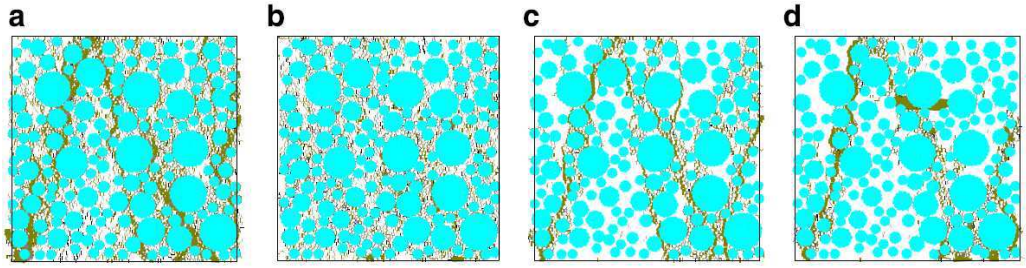

Figure 1.25: Compression, final crack pattern: deformable aggregate. (a) Brittle F, (b) Brittle NF, (c) Soft. F and (d) Soft. NF (Moneiro Azevedo *et al.* [44]); F/NF - with/without pure friction contacts

and stiffness or by projecting the lattice on a generated grain structure of concrete and in assigning different material properties to beams corresponding to the cement matrix, to the aggregate or to the interfacial transition zone. The comparison of simulations with experimental tests (uniaxial tensile test, four-point shear, pull-out of steel anchor test) showed that lattice models can reproduce micromechanisms of fracture like micro-cracking, crack branching and crack face bridging, as well as fracture mechanisms of larger structures (plates, beams).

Similar model to study the fracture process in concrete was developed by Liliu and van Mier [39] in 3 dimensions.

Another approach, called Lattice Discrete Particle Model (LDPM), was proposed by Cusatis *et al.* [18, 17]. The 3D mesostructure of concrete was simulated by an assembly of aggregate particles, according to the actual aggregate size distribution in concrete, connected by a lattice system obtained through a Dalaunay tetrahedralization of the aggregate centers. The mechanical interaction between the particles was characterized by normal and shear stresses defined at the contact surfaces obtained by a three-dimensional domain tessellation. Contrary to the classical lattice models, LDPM employs a complex constitutive law, applied at the level of lattice struts (aggregates are rigid), embodying nonlinearity and inelastic behavior. The model simulates accurately the behavior of concrete under uniaxial and multiaxial loading conditions in both tension and compression. Moreover, it captures the realistic crack patterns corresponding to different loading paths.

A limitation of the classical lattice models when studying concrete in compressive mode is that no new contacts are generated during the deformation process. Poinard [48] used a model that combined the lattice system of cohesive interactions with the classical DEM contact interactions created under compressive loading to reproduce concrete behavior under high confinement. A mesostructure of concrete was obtained from the 3D segmentation of tomographic images and superimposed on an assembly of different size spheres (see Fig. 1.26). Spheres corresponding to the pores were removed from the assembly. A local plastic-damage constitutive law, previously used for the macroscopic modeling of concrete [59], was now used at the meso-scale with different local parameters for mortar, aggregates and interface. The model was able to well represent the macroscopic behavior of concrete under different confinement loadings but did not permit to understand the failure mechanisms of concrete under high triaxial loading.

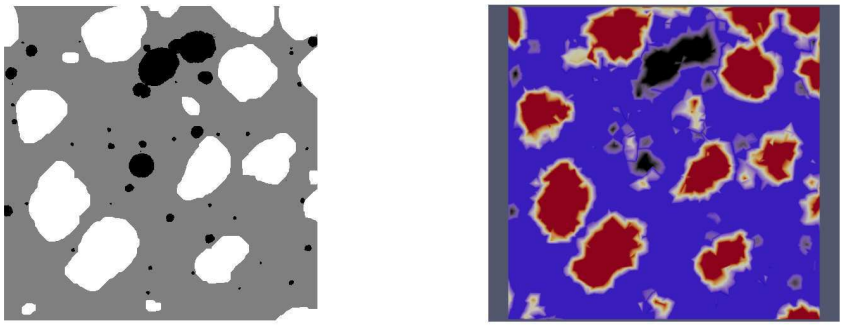

Figure 1.26: Vertical cut of a cube representing concrete mesostructure (Poinard [48])
(left) Segmented concrete cube: pores (black), aggregates (white), mortar (grey)
(right) Numerical concrete sample (spheres assembly visualized by Voronoï cells): pores (black), aggregates (red), mortar (violet)

Chapter 2

Experimental investigation

This chapter provides experimental characterization of concrete triaxial behavior at different levels of confinement regarding the influence of coarse aggregates. The main aspects of concrete behavior, particularly at high stress levels were presented in the previous chapter. An important finding was that under very high confinement, concrete behaves like a non-cohesive granular stacking, on one hand no more influenced by the cement matrix strength and on the other hand strongly affected by the presence of free water.

Therefore, it is important to better understand the role of this granular skeleton. The effect of coarse aggregates size on concrete triaxial behavior was reported in the bibliographic review. Another feature characterizing the granular skeleton is the type of coarse aggregates. It is generally known that it affects considerably the uniaxial strength of high performance concrete what is much less pronounced for ordinary concretes. No results are available concerning the influence of coarse aggregates type on concrete behavior when subjected to high triaxial compression loading. The present work focuses on this issue taking into account the shape and the composition of coarse aggregates.

The first section of this chapter will present the experimental set-up used to perform the current study. The composition of studied concretes and sample preparation will be then described. The last section will provide the test results and the main conclusions.

2.1 Experimental set-up: triaxial press

Triaxial tests were performed by the means of a high-capacity triaxial press, called GIGA, designed and made by the THIOT Ingénierie with the financial support of the CEA Gramat. The development of the testing procedure on concrete has been presented in details in [65], [63]. The press, illustrated in Figure 2.1, is able to generate a confining pressure up to 0.85 GPa and an axial stress reaching 2.3 GPa on cylindrical concrete specimens of 7 cm in diameter and 14 cm long. Figure 3 shows the main components of the press (a) and a cross sectional view of the confining cell, where the concrete sample is placed (b). The confining fluid, diethylhexyl azelate, a non-volatile organic, inert and slightly-compressible liquid, is injected into the cell through an upper opening. It is then pressurized by means of a pressure multiplying jack. The axial force is generated from a 13 MN jack located under the cell and then transmitted to the sample by a piston passing through the lower plug of the confining cell.

Figure 2.1: Overview of the triaxial press GIGA

2.1.1 Loading path

The specimen is loaded both hydrostatically and along its axis. The confining pressure and the axial jack displacement are controlled independently which allows different loading paths, schematically presented in Figure 2.3. The triaxial compression loading is applied in two phases: hydrostatic and deviatoric. The hydrostatic phase consists of applying a confining pressure all around the specimen at a constant stress rate of 1.67 MPa/s up to a desired value. Once the intended confinement has been reached, the specimen is loaded axially at a constant displacement rate of 20 $\mu m/s$ (*i.e.* a strain rate of approx. $10^{-4}/s$) while keeping the confining pressure constant. The unloading phase proceeds in the reverse order.

Uniaxial compression tests were performed on a different laboratory press, *i.e.* the 100-ton Schenk press. These tests were controlled in displacement with a strain rate of approx. $10^{-5}/s$.

2.1.2 Instrumentation and measurements

The press is equipped with different sensors that allow governing the tests and provide information about the state of the sample during loading. An axial displacement sensor is used to control axial jack displacement, while an axial force sensor and a pressure sensor positioned inside the confining cell yield the stress state on the specimen.
The pressure sensor, installed close to the entrance to the confinement cell, determines the pressure within the cell with a measurement accuracy of 1% over the operating range.

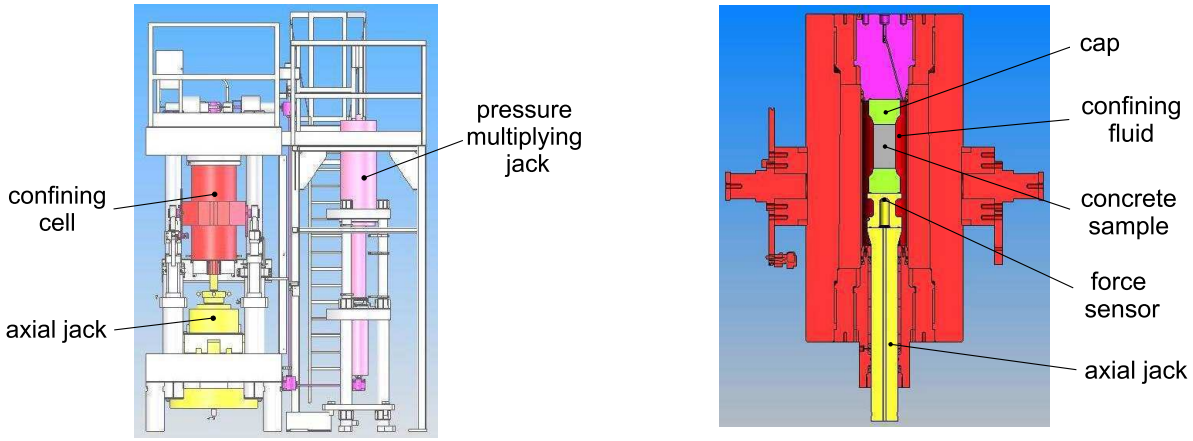

(a) (b)

Figure 2.2: Schematic illustration of the triaxial press GIGA
(a) General scheme of the press
(b) Cross-sectional view of the confining cell

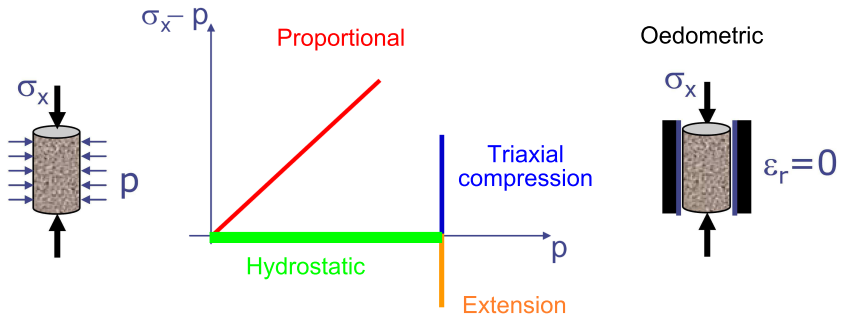

Figure 2.3: Available loading paths of the triaxial press GIGA

The sensor has to be calibrated, certified and replaced annually. The force sensor, positioned between the lower loading head and the piston (Fig. 2.2(b)), is a metal body that deforms elastically over the machine loading range. The force transmitted by the sensor is deduced from its strain. The results obtained by Vu [63] show that the deviatoric force is determined with a measurement accuracy of 3%.

The sample strain measurements is carried out using an LVDT (Linear Variable Differential Transformer) sensor, an axial gauge and two circumferential gauges (Fig. 2.4). The LVDT sensor gives the length variation of the specimen. Each part of the sensor is fixed on a loading head what leads to a global measurement of the axial strain. The axial gauge, bonded to the middle of the concrete sample, provides a local strain measurement. Comparison of both allows evaluating sample strain homogeneity. The circumferential strain is measured by means of two gauges, in order to increase the probability of maintaining at least one measurement up to the end of the test and check the strain homogeneity.

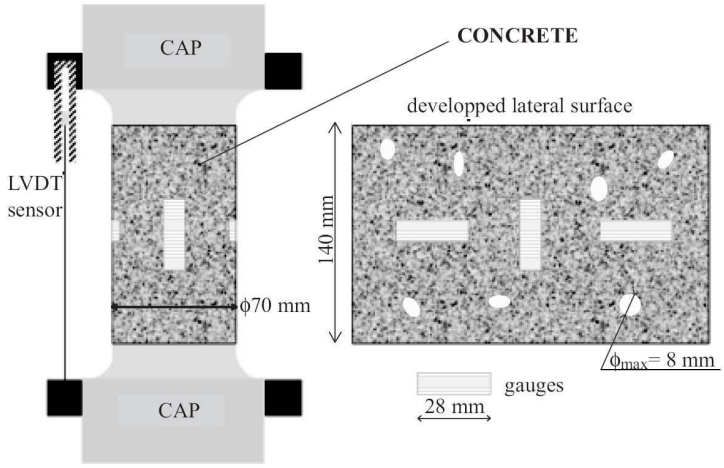

Figure 2.4: Scheme of strain measurement devices

2.2 Concrete composition and specimen preparation

2.2.1 Concrete formulation

The present study was performed on four concretes which are distinguished by the type of coarse aggregates:

- rolled aggregate concrete (SR)[1] - rolled siliceous aggregates derived from a natural deposit
- crushed aggregate concrete (SC) - crushed aggregates obtained from the siliceous rock
- glass ball concrete (GB)
- limestone aggregate concrete (LC) - crushed aggregates obtained from the soft limestone rock

The mix designs of each of these four concretes are presented in Table 2.1. The concretes are characterized by the same cement matrix composition and the same aggregates volume. A superplasticizer was used in crushed aggregate concrete to increase the workability of the fresh concrete mixture. Aggregates size distribution are chosen as close as possible for all concretes. Figure 2.5 displays granulometry curves of four sets of aggregates.

2.2.2 Fabrication of samples

A manufacturing procedure for concrete samples was developed with the aim of ensuring minimal variability in the mechanical properties of concretes. The choice of the specimen size, 7 cm of diameter and 14 cm of length, allows testing the specimens under high stress levels and considering concrete as a homogeneous material according to

[1]Concrete R30A7 - ordinary concrete in terms of both strength (30 MPa) and slump (7 cm)

Concrete	**SR**	**SC**	**GB**	**LC**
Gravel/Crushed rock D 0.5/8 $[kg/m^3]$	1008	1008	-	891
Glass balls D 1.5/9 $[kg/m^3]$	-	-	980	-
Sand D_{max} 1800 μm $[kg/m^3]$	838	838	838	838
Cement CEM I 52.5 N PM ES CP2 (Vicat) $[kg/m^3]$	263	263	263	263
Water $[kg/m^3]$	169	167.5	169	169
Superplasticizer "Sikafluid" $[kg/m^3]$	0	1.8	0	0
Density $[kg/m^3]$	2278	2278	2250	2161
Porosity accessible to water [%]	11.8	10.8	12.6	x
Porosity accessible to mercury [%]	12.6	11.9	?	?

Table 2.1: Composition and porosity of studied concretes

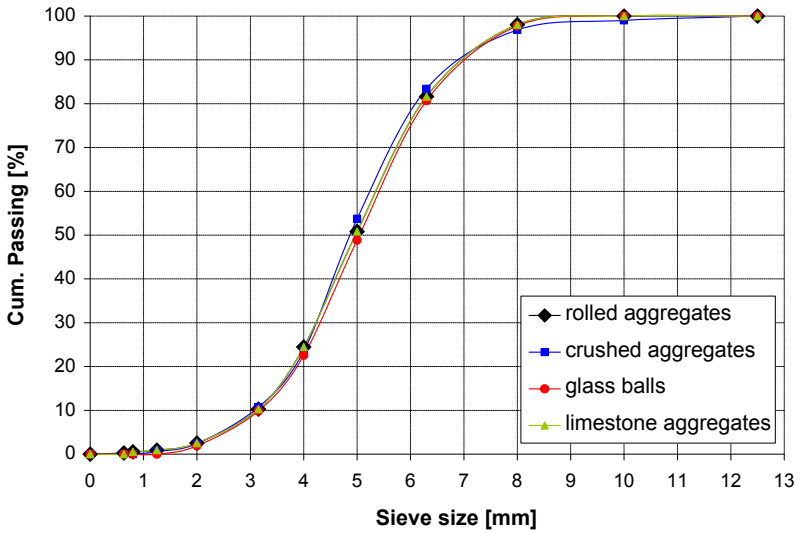

Figure 2.5: Granulometry curves of coarse aggregates used in the studied concretes

the maximum aggregate size (8 mm). The ratio length/diameter equal to 2, commonly used to characterize concrete and geomaterials, enables limiting the influence of boundary conditions on the specimen behavior and preventing from buckling.

Concrete is casted in a 13.5 liter parallelepiped mold. After 24 hours the concrete block is removed. It is then conserved for 28 days in a saturated environment inside waterproof bags immersed in water, to insulate concrete both physically and thermally during hydration process. The block is then cored, cut and ground under water to prevent specimens and tools from overheating. The defect in parallelism of two samples faces is less than 0.1 mm and small enough to ensure the homogeneous distribution of the stress during axial loading.

After machining, the samples are placed in a drying oven at a temperature of 50°C and a relative humidity of 8% until the stabilization of their mass. Mass is considered as stable when its daily variation does not exceed 0.1% what is achieved after one month of drying in the oven (Vu [63]). According to the work of Castellote *et al.* [11], at a temperature

higher than 50°C dehydration of the CSH gel and the ettringite is observed, what modifies the microstructure of the material. Thus, the drying conditions where chosen to restrict the drying process to the evaporation of the free water in the cement matrix.

2.2.3 Concrete porosity

Mechanical properties of concrete are strongly influenced by its porosity. Several pore types characterized by different sizes and shapes constitute the material porosity: entrapped air, capillary pores, gel pores and entrained air bubbles, if present. The volume of voids in concrete can be evaluated using different methods. Two measurements were employed to evaluate the porosity of concretes used in this study.

Porosity accessible to water

Porosity accessible to water is determined with the method recommended by Ollivier [34]. It consists in measuring the weight of the sample at three stages:
- saturated sample (M_{sat}),
- saturated sample under water (M_{hyd}) (hydrostatic weighing),
- dried sample (M_{dry}).

Hydrostatic weighing and weighing of saturated sample in the air are performed on concrete that has never been dried. The three measurements allow determining the porosity accessible to water. According to the Archimedes principle:

$$M_{hyd} = M_{sat} - \rho_{water} V \tag{2.1}$$

Then, the density of concrete, ρ_d, and its porosity, η, can be determined:

$$\rho_d = \frac{M_{dry}}{V} = \frac{M_{dry}}{M_{sat} - M_{hyd}} \rho_{water} \tag{2.2}$$

$$\eta = \frac{M_{sat} - M_{dry}}{M_{sat} - M_{hyd}} \tag{2.3}$$

Mercury intrusion porosimetry

Mercury porosimetry is a widely accepted method for the characterization of porous material with different-scale porosity. The measurement is based on the intrusion volume penetrating in a sample when subjected to the increasing pressure (up to 400 MPa). The smallest pore size that can be filled with mercury is of about 3.5 nm. The measurements were performed by the Laboratoire d'étude des Transferts en Hydrologie et Environement (LTHE) in Grenoble.

The mean values of porosities obtained with these two measurements were presented in Table 2.1. Both measurements provide consistent values. Only small differences, probably attributed to the measurement precision are observed. The porosities of concretes used in this study are considered to be close to 12%.

2.2.4 Specimen instrumentation

Triaxial testing of concrete at high levels of confinement requires special attention while preparing the samples. Material porosity and high pressure around the specimen may cause the penetration of the confining fluid into the specimen after the perforation of the membrane, what affects material properties and functioning of the gauges. In order to avoid this punching effect, a special procedure for the preparation of the surfaces of the specimens and for the setting of protection devices is carried out.

Surface preparation

The first step of the surface preparation consists of opening the subjacent porosity with a portable milling machine. Then, the opened pores are filled in with a mortar, whose mechanical properties are close to those of concrete. Once the surface is rubbed down and cleaned, the gauges are glued on the areas with the smallest amount of the previously filled pores using the Vishay M-Bond GA-2 adhesive, specially adapted for concretes. Immediately, a latex membrane is placed around the sample which provides a uniform pressure on the gauges during the binding time and a very thin layer of adhesive between the gauges and the sample. It is essential in order to represent accurately the concrete strains.

Protection devices

A 2mm plastic shield (Veralite 200) is locally set up on the gauges as an additional protection (Fig. 2.6). Gauges are connected to the copper mono wires passing through the shield which are next connected to the electrical wires. The specimen is then wrapped within a multilayer protective membrane in order to prevent the confining fluid from infiltrating the sample. First layers, with the overall thickness of 8 mm, are composed of latex that exhibits high shear strength and deformability. However, it can be easily dissolved by the confining fluid. The last two layers are thus made of neoprene used for its significant chemical resistance. The perforating of the membrane to pass the electrical wires is a possible source of infiltration of the confining fluid and requires a special attention. The holes through which the wires go out of the membrane are protected by silicone.

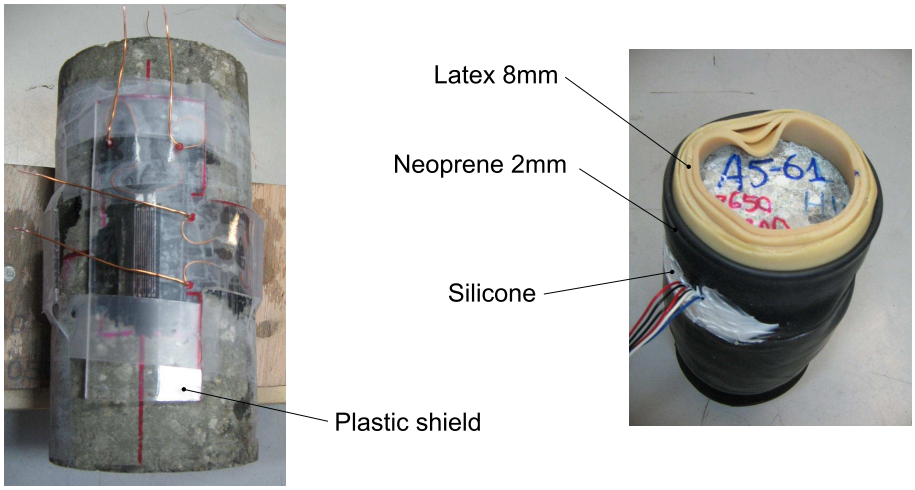

Figure 2.6: Protective device of concrete sample tested in the GIGA press

2.3 Testing program

Table 2.2 summarizes triaxial tests that will be discussed in following sections. All tested samples were conserved in the oven at a temperature of 50°C long enough to assume negligible effect of age on concrete strength.

Material	**Confining pressure p [MPa]**
Crushed aggregate concrete (SC)	$p_c = 0$
	$p_c = 50$
	$p_c = 100$
	$p_c = 650$
Glass ball concrete (GB)	$p_c = 0$
	$p_c = 50$
	$p_c = 100$
	$p_c = 200$
	$p_c = 650$
Limestone rock	$p_c = 0^{(1)}$
	$p_c = 50^{(1)}$
	$p_c = 200$
	$p_c = 600$
Limestone aggregate concrete (LC)	$p_c = 0^{(1)}$
	$p_c = 50$
	$p_c = 200$
	$p_c = 650$

Table 2.2: Summary of the tests performed in the study; (1) tests carried out by Ke Yang in the laboratory 3SR

2.4 Influence of coarse aggregate shape

A variety of aggregate properties, which are often difficult to measure, complicate the task of studying the effect of a single aggregate characteristic on concrete behavior. This section will attempt to evaluate the influence of coarse aggregate shape. Triaxial tests were performed on the three concretes made with different-shape aggregates: rolled, crushed and glass spheres. Figure 2.7 displays images of these three concretes obtained by the X-ray tomography. Table 2.3 then summarizes some of the physical properties for the three aggregate types, which which roughly resemble one another. In contrast, all three kinds of aggregates exhibit strong differences with respect to their shapes and surface textures. This study therefore has mainly focused on such external aggregate characteristics, while keeping in mind that glass is a somewhat different material than siliceous gravel or rock and features different elastic and strength properties. These aspects will be considered in Section 2.5, which will discuss the effect of coarse aggregate composition.

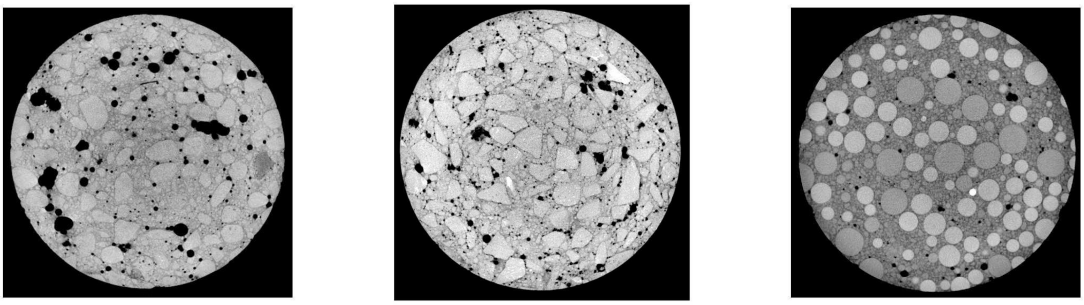

(a) Rolled aggregate concrete (b) Crushed aggregate concrete (c) Glass ball concrete

Figure 2.7: Tomographic cross-sectional view of three concretes varying by coarse aggregate shape

Aggregate type	**Rolled**	**Crushed**	**Glass balls**
Silica content [%]	99	97	60-74
Density $[g/cm^3]$	2.6	2.6	2.5
Bulk density $[g/cm^3]$	1.6	1.6	1.5

Table 2.3: Properties of rolled aggregates, crushed aggregates and glass balls

2.4.1 Triaxial tests results

In this section, results of triaxial tests performed on the three test concretes, SR, SC and GB, at various levels of confinement will be discussed.

For the unconfined compression test, volumetric behavior (mean stress σ_m vs. volumetric strain ε_v) and axial behavior (axial stress σ_x vs. axial strain ε_x and circumferential strain ε_θ) are output. For tests carried out under a confining pressure, in addition to the volumetric and axial behavior, the deviatoric part of axial behavior (deviatoric stress q vs axial strain ε_x and circumferential strain ε_θ) is determined. Each curve is offset such that strain ($\varepsilon'_{\theta,x}$) is equal to 0 when q equals zero.

Axial strain is obtained from the LVDT sensor, and circumferential strain is derived as the mean of the two circumferential gauges readings. Volumetric strain is calculated from these two measurements, in assuming that the concrete radial strain is similar to the circumferential strain:

$$\varepsilon_v = \varepsilon_x + 2\varepsilon_\theta \tag{2.4}$$

2.4.1.1 Unconfined compression test

Figure 4 shows the results of unconfined compression tests performed on the three studied concretes. The corresponding elastic properties and strengths are listed in Table 2.4. It can be observed that all three concretes display very similar elastic properties, though differences in the ultimate stress are noted. Glass ball concrete exhibits strength considerably lower than concrete made with rolled or crushed aggregates. The highest strength is found for the crushed aggregate concrete. The uniaxial strength of an ordinary

concrete is controlled by the strength at the mortar/aggregate interface, which is the weakest zone in concrete provided sufficiently strong aggregates (see typical crack pattern in Fig. 2.25(a)). Very smooth spherical aggregates produce weaker interfacial bonds, which results in a lower glass ball concrete strength. The weakness of the interface in glass ball concrete is confirmed by its tensile strength, as evaluated from the splitting tensile test at 2.7 MPa. This value is notably less than the direct tensile strength of rolled aggregate concrete, which equals 3.7 MPa. A slight increase in strength when introducing crushed aggregate is indeed observed. Let's assume that the nearly identical composition of rolled and crushed aggregates yields a similar microscopic surface roughness and, consequently, a comparable interfacial bond strength. On the other hand, crushed aggregates have higher mesoscopic roughness than rolled aggregates, and this finding results in the higher strength of concrete, most likely due to the mechanical interlocking of the aggregate and the cement matrix.

Concrete	**SR**	**SC**	**GB**
Young's modulus, E $[GPa]$	33	33	32
Poisson's ratio, ν $[-]$	0.16	0.16	0.19
Compressive strength, σ_c $[MPa]$	40	43	33

Table 2.4: Classical concrete characteristics identified from simple compression test

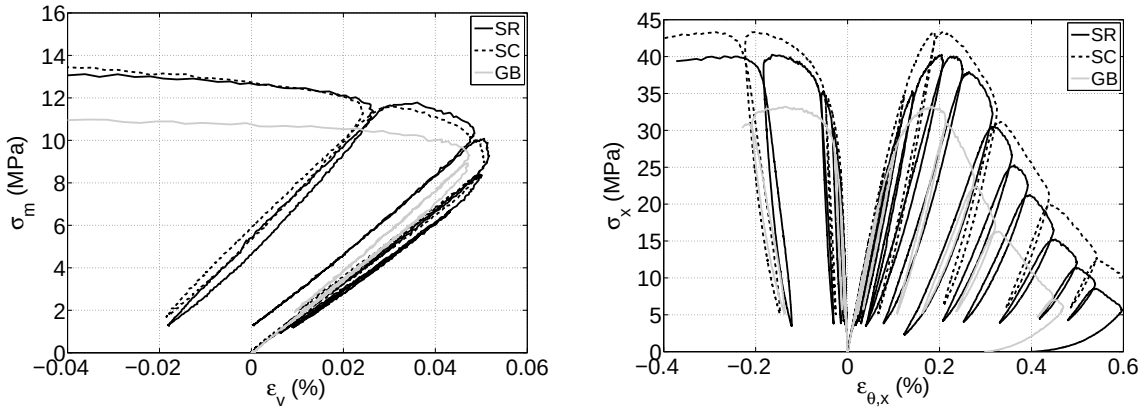

(a) (b)

Figure 2.8: Simple compression test on concretes with rolled aggregates (SR), crushed aggregates (SC) and glass balls (GB);
(a) mean stress σ_m vs. volumetric strain ε_v
(b) axial stress σ_x vs. strain components ε_θ and ε_x

2.4.1.2 Triaxial compression

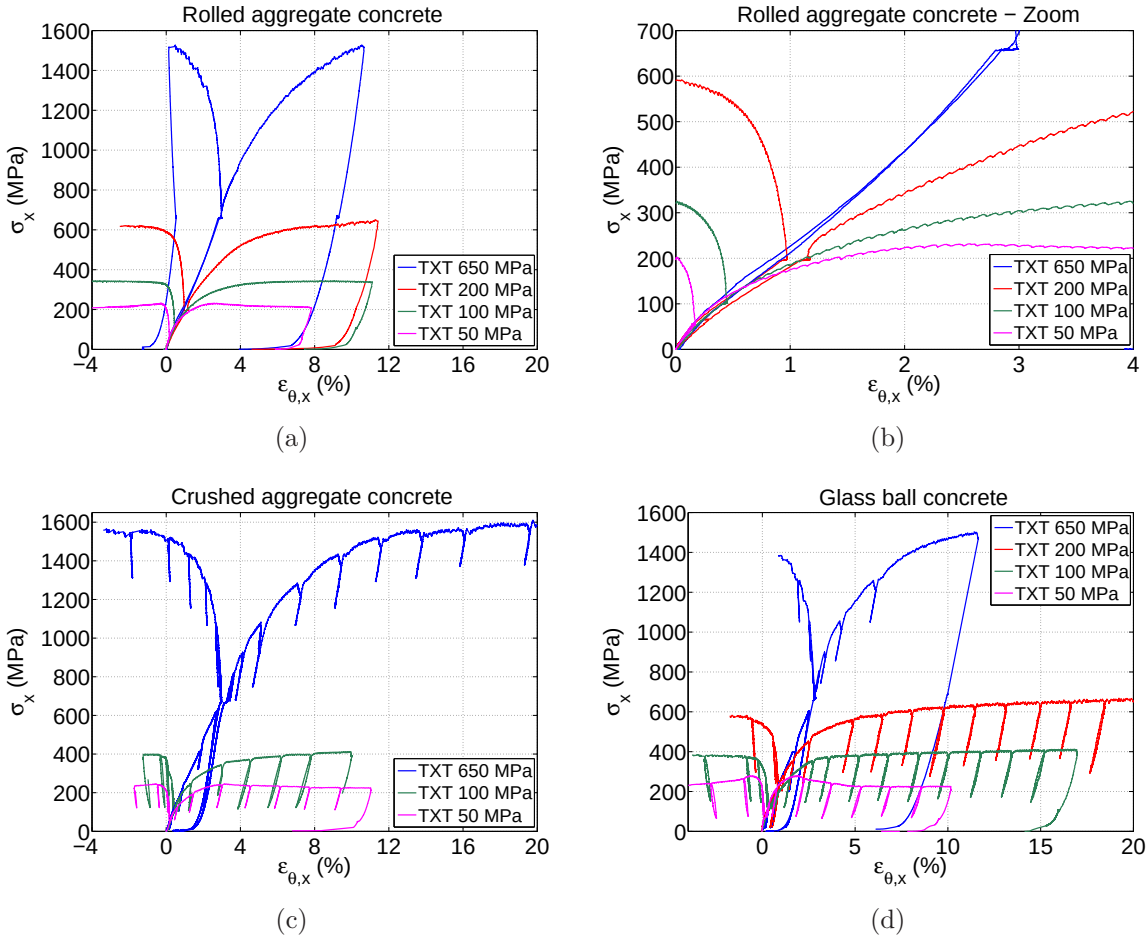

Figure 2.9: Triaxial tests conducted at different confining pressures; axial stress σ_x vs. strain components ε_θ and ε_x

Figure 2.9 shows the results of triaxial compression tests at different confining pressures. The axial behavior of each concrete is presented. During the hydrostatic phase the same trend is observed regardless of the type of aggregate. A short linear phase (up to 40 - 60 MPa of confinement) is followed by a decrease of the tangential stiffness. A progressive stiffening is observed from 200 - 300 MPa of confinement. The stiffness reduction may be explained by the cement matrix damage beyond the elastic phase, while stiffening by the material densification. The latter corresponds to the porosity closure when important hydrostatic strains are reached.

Concerning the deviatoric phase, the increase of confining pressure results in a significant increase of the loading capacity of three concretes. The transition from quasi-brittle behavior under unconfined compression to ductile behavior with the presence of confinement is observed. For 50 MPa of confinement, a softening behavior with a distinct peak stress is still observed while higher levels of confinement produce the stress-strain curves with a plateau.

Evolution of concrete behavior with the confining pressure results in different damage patterns, what is schematically presented in Figure 2.10. As reported in the bibliographic review, studies of Gabet [29] and Vu [63] revealed transition from quasi-vertical cracks under uniaxial compression to localization bands perpendicular to the main loading axis under high confinement (>100 MPa). In between, damage appears in a form of localization bands, inclined at an angle of 45° - 60° under confining pressure of 50 MPa, and almost perpendicular to the axial direction at 100 MPa of confinement.

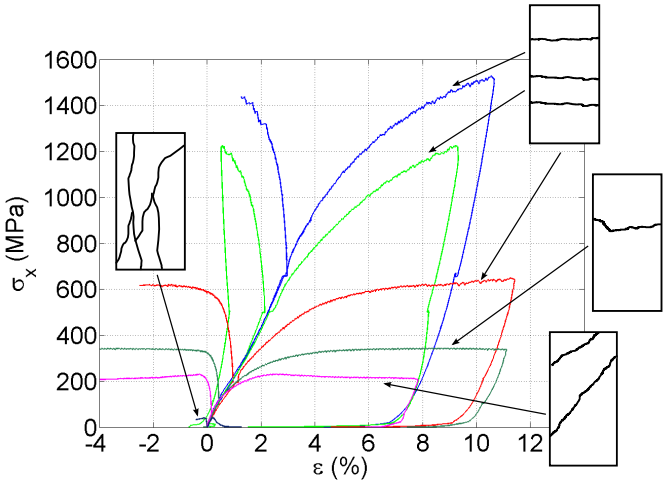

Figure 2.10: Evolution of failure patterns under triaxial compression loading for rolled aggregate concrete

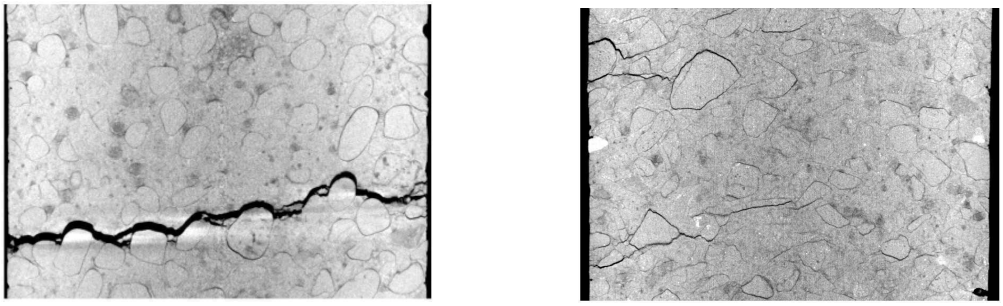

(a) rolled aggregate concrete (b) crushed aggregate concrete

Figure 2.11: Tomographic view of failure patterns in a concrete specimen tested under triaxial compression at 650 MPa of confinement (Poinard [50])

These observations were completed by the tomographic analysis of samples tested at low and very high confinement carried out by Poinard [50] on both rolled aggregate concrete and crushed aggregate concrete. The same failure mechanisms were observed regardless of the aggregate shape. Figure 2.11 displays tomographic images of the two concrete samples, with rolled and crushed aggregates, tested under triaxial compression at 650 MPa of confinement. Both images indicate strong compaction and localized damage

in a form of cracks perpendicular to the compression axis.

Different triaxial tests conducted on crushed aggregate concrete discussed in this chapter confirmed no difference in failure patterns with respect to the rolled aggregate concrete, whereas an unfamiliar phenomenon was observed for glass ball concrete at low confinement level. This result will be discussed in the following paragraph.

It appears that concretes with different aggregate shapes exhibit the same kind of overall macroscopic behavior. In order to capture the differences, the volumetric and deviatoric behavior curves for the three studied concretes at various confinement levels will be now compared.

Triaxial test at 50 MPa confinement

Figure 5 presents the results of triaxial tests conducted at 50 MPa of confinement on concrete samples with rolled aggregates, crushed aggregates and glass balls. The volumetric behavior is nearly linear during the hydrostatic phase for all three samples. The volumetric stiffness of glass ball concrete however is considerably greater than that of the other two samples, which are roughly the same. This result is attributed to the elastic properties of aggregates and glass balls; Section 2.5 will provide a more detailed discussion of this topic.

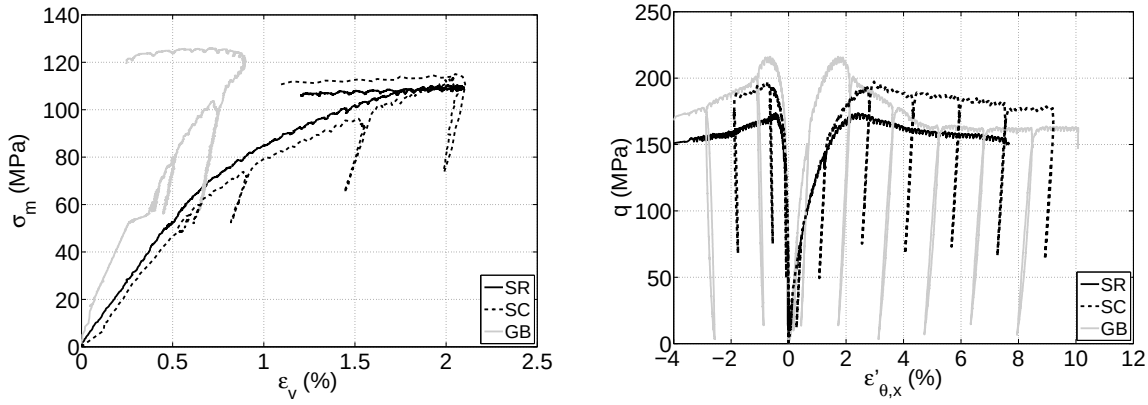

(a) (b)

Figure 2.12: Triaxial test at 50 MPa of confinement on concretes with rolled aggregates (SR), crushed aggregates (SC) and glass balls (GB);
(a) mean stress σ_m vs. volumetric strain ε_v
(b) stress deviator q vs. strain components ε'_θ and ε'_x

Figure 4.5(b) indicates the differences in maximum deviatoric stress. The lowest strength is found for rolled aggregate concrete and the highest for glass ball concrete. In addition, glass ball concrete exhibits stiffer behavior and a more pronounced peak stress than the other two concretes. The ultimate stress of crushed aggregate concrete is slightly higher than that of rolled aggregate concrete.

To explain these differences, it is instructive to compare the failure patterns observed for the three samples (see Fig. 6). Rolled aggregate concrete and crushed aggregate concrete both feature very similar crack patterns. The failure mechanism is highly localized in a few cracks inclined at 30° to the axial direction. Some large aggregates are broken, especially in the crushed aggregate sample. As with the unconfined compression, the higher strength of SC is probably due to the higher roughness of crushed aggregates, thus leading to a stronger aggregate/mortar bond at the mesoscopic scale.

The crack pattern in glass ball concrete is very different from the other two. Several cracks perpendicular to the axial direction can be observed; they are characterized by a glass ball debonding phenomenon. In all likelihood, this crack pattern is primarily due to the strength of glass balls and will be discussed further in Section 2.5.

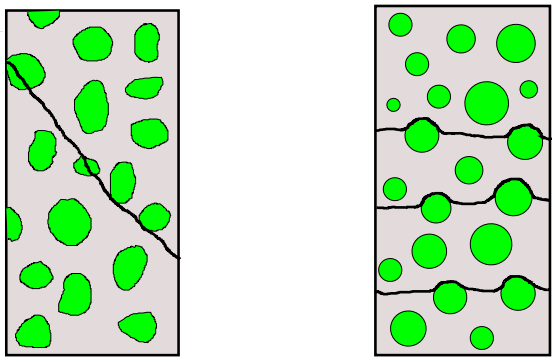

(a) (b)

Figure 2.13: Sketches of failure patterns in concrete samples at 50 MPa of confinement: (a) siliceous aggregate concrete (SR, SC), (b) glass ball concrete (GB)

Triaxial test at 100 MPa confinement

Volumetric and deviatoric behavior of the three studied concretes under triaxial compression at 100 MPa of confinement are presented in Figure 2.14. Remarkably higher volumetric strain is reached by crushed aggregate concrete before the transition from contractant to dilatant behavior. However, the measurement of volumetric strain by the means of strain gauges is problematical and not necessarily meaningful once the localization occurs.

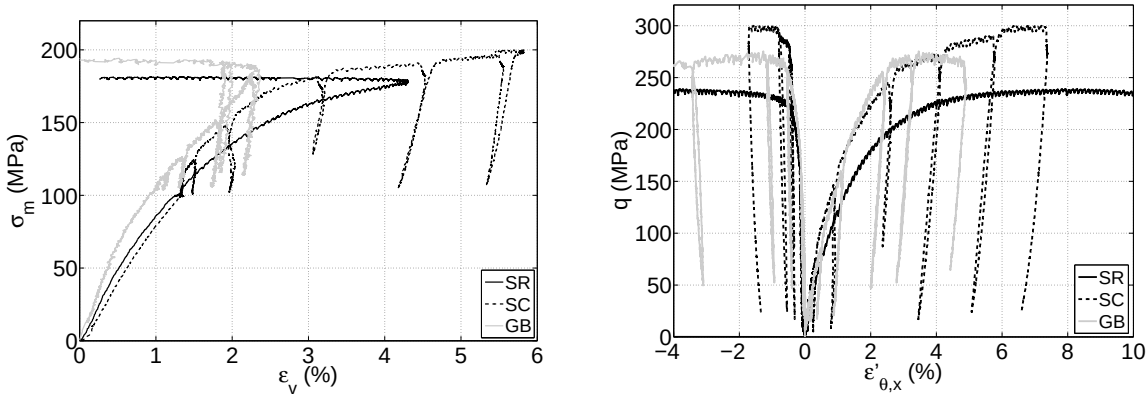

(a) (b)

Figure 2.14: Triaxial test at 100 MPa of confinement on concretes with rolled aggregates (SR), crushed aggregates (SC) and glass balls (GB);
(a) mean stress σ_m vs. volumetric strain ε_v
(b) stress deviator q vs. strain components ε'_θ and ε'_x

Figure 2.14(b) shows that at this level of confinement, crushed aggregate concrete reaches the highest deviatoric stress. The lowest strength is observed for rolled aggregate concrete. The higher value of strength of about 25% and the increase of tangential stiffness

of crushed aggregate concrete is probably linked to the shape of aggregates. At this level of confinement, when the cement matrix is strongly damaged the mesoscopic surface roughness of crushed aggregates may be an important factor that enhances shear capacity of the material. The difference in maximum stress for glass ball concrete and rolled aggregate concrete is limitted to 13%. We can suppose that the effect of aggregates strength is less important at this level of damage of the cement paste.

Triaxial test at 650 MPa confinement

Figure 7 presents the results of triaxial tests at 650 MPa of confinement conducted on the three studied concretes. The volumetric behavior displayed in Figure 4.7(a) suggests the slightly lower deformability of glass ball concrete.

The deviatoric behavior shown in Figure 4.7(b) indicates that under very high confinement, all three concretes behave nearly the same in terms of ultimate stress and tangential stiffness. Their respective failure patterns are also very similar. A series of cracks perpendicular to the axial direction with considerable debonding and a few broken aggregates are observed (see Fig. 2.16). At this level of confinement, concrete behaves like a non-cohesive granular stacking. Due to the presence of destroyed cement matrix between, the aggregate shape has no effect on the behavior of this granular assembly. Its behavior is likely being controlled by the compacted cement matrix between the largest aggregates.

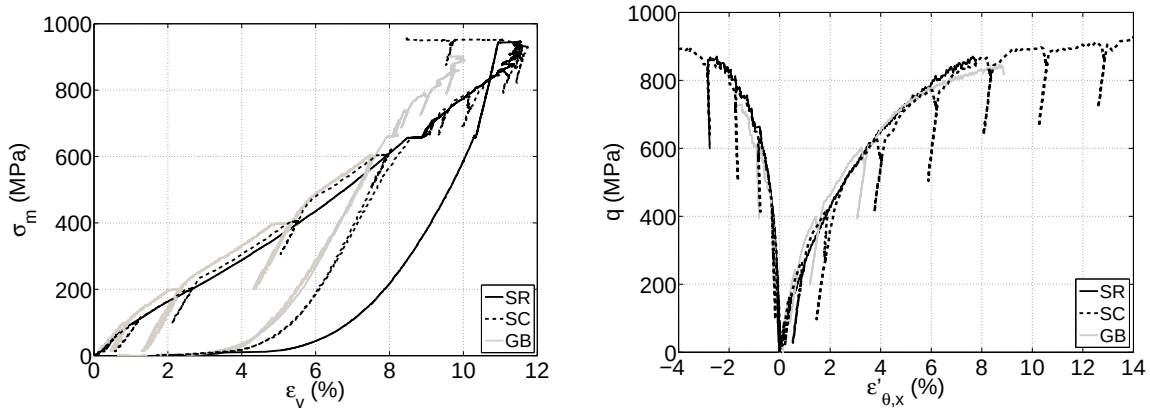

(a) (b)

Figure 2.15: Triaxial test at 650 MPa of confinement on concrete with rolled aggregates (SR), crushed aggregates (SC) and glass balls (GB);
(a) mean stress σ_m vs. volumetric strain ε_v
(b) stress deviator q vs. strain components ε'_θ and ε'_x

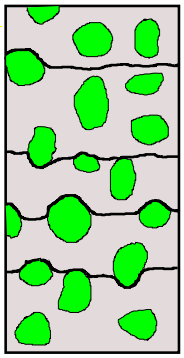

Figure 2.16: Sketch of failure patterns in concrete sample at 650 MPa of confinement for rolled aggregate concrete (SC), crushed aggregate concrete (SC) and glass ball concrete (GB)

2.4.1.3 Limit states

The evolution of concrete strength with the increase of confinement is expressed by a limit state curve. Two criteria may be used to identify the concrete limit states. The limit state can be either related to the maximum deviatoric stress that the material can support or to the stress state associated with the transition point from contractant to dilatant behavior of the material. The capacity of the experimental device does not allow a precise identification of the stress limit state for high confining pressures. Namely, the peak stress appears after the transition from contraction to dilatancy and often when the gauges signals are lost and the evolution of the sample's diameter is no longer taken into account in the stress evaluation. Often no peak stress is reached before the unloading.

Therefore, the following analysis refer to the strain limit state, corresponding to the maximum volumetric strain in terms of the material contraction. It's worth to notice that at low confinements, the strain limit state practically coincides with the stress limit state of the concrete.

Figure 2.17(a) displays the strain limit states of concretes with rolled aggregates, crushed aggregates and glass balls in the (σ_m,q) plane, corresponding to the performed triaxial tests. It can be observed that the loading capacity of concrete strongly increases with the increase of the mean stress, whatever the shape of coarse aggregates is. A parabolic law fitting $q = a(b+\sigma_m)^c$ is used to describe the failure surface of concrete with rolled aggregates. The fitting parameters where previously determined as a = 4.81, b = 1.82 and c = 0.758 (Vu *et al.* [66]).

Figure 2.17(b) presents the same limit states in a (σ_m,q/q_{SR}) plane, where q/q_{SR} is a ratio between the limit stress deviator of a given concrete to the limit stress deviator of concrete with rolled aggregates, used as a reference concrete, at the same confining pressure. This presentation provides a better perception of the differences between the three concretes. Under unconfined compression, the deviatoric stress is reduced a lot for glass ball concrete. The limit states are dependent on the on the strength of the mortar/aggregate interface. At low level of confinement (50 MPa), the limit states are close for the three concretes, however the increase of strength of glass ball concrete is observed. Concrete behavior seems to be governed by the cement matrix cohesion but

also by the volume of the mortar/aggregate interface. At this level of the mean stress, the contraction-dilatancy transition is associated to the opening of microcracks in the material during gradual damage of the cement matrix (Mazars [41]). As the confining pressure increases (100 MPa), the increase of shear strength for crushed aggregate concrete is observed. At high confinement (200MPa - 650 MPa), cement matrix cohesion is practically lost and concrete behaves like a granular stacking. The shear stress generates a rearrangement of the particles which initially produces material compaction. Once the maximum compaction has been reached, the sample dilates. The mean stress level corresponding to this strain limit state is considerably lower for glass ball concrete than for rolled aggregate and crushed aggregate concretes. The last two concretes behave in the same way.

Deformation ability of concrete seems to be related to the shape of aggregate particles. Irregular crushed aggregates may generate strong friction forces when the cement matrix is partially damaged what increases the shearing capacity of concrete. This effect is no more perceptible at high confinement, whereas spherical glass aggregates reduce the compaction of concrete when the cement paste is fully damaged.

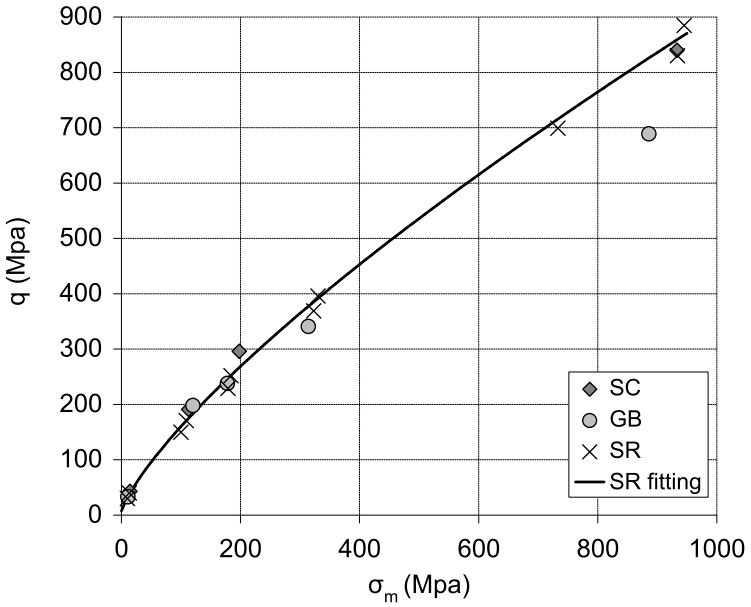

(a)

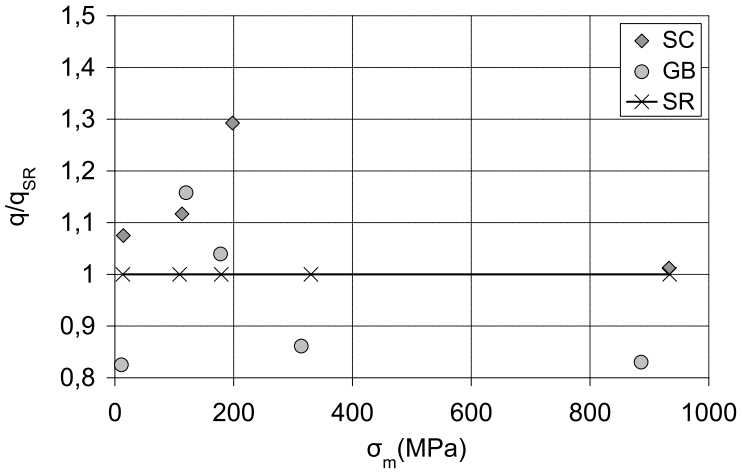

(b)

Figure 2.17: Limit states of concretes with rolled aggregates (SR), crushed aggregates (SC) and glass balls (GB):
(a) stress deviator q vs. mean stress σ_m
(b) relative deviator q/q_{SR} vs. mean stress σ_m, where q_{SR} is the deviatoric stress associated with the limit state of concrete with rolled aggregates

2.5 Influence of coarse aggregate composition

This section pertains to the effect of coarse aggregate composition on triaxial behavior of concrete. The previously introduced concrete with rolled siliceous aggregates (SR) and glass ball concrete (GB) will be analyzed herein, with emphasis placed on the effect of aggregate strength and elastic properties. These characteristics, as identified from the unconfined compression tests (Fig. 2.18) are summarized in Table 1. Glass exhibits very good mechanical properties, although they vary widely depending on mix design, production conditions, *etc.* Despite the very high theoretical compressive strength of glass, *i.e.* on the order of 10^4 MPa [1], this value cannot be used in practice since glass surface defects cause stress concentrations that generate widely varying failure stresses. The generally accepted value is 1 GPa; it is therefore considered herein that the compressive strength of glass balls highly exceeds that of siliceous aggregates (330 MPa).

Behaviors of concretes with crushed siliceous aggregates (SC) and crushed limestone aggregates (LC), which exhibit very different physical and mechanical properties (see Table 1) will be also compared. The porosity of limestone rock equal to 9.4% is very important in comparison with the porosity of siliceous rock $< 2\%$.

Aggregate type	**Siliceous**	**Glass**	**Limestone**
Density, ρ $[g/cm^3]$	2.6	2.5	2.3
Young's modulus, E $[GPa]$	78	70	51
Poisson's ratio, ν $[-]$	0.12	0.22	0.28
Compressive strength, σ_c $[MPa]$	330	$\approx$1000	150

Table 2.5: Physical and mechanical properties of coarse aggregates

2.5.1 Results of triaxial tests performed on rocks

In order to better understand the response of concretes, the triaxial behavior of rocks was investigated. Tests were performed on cylindrical samples, 50 mm in diameter and 105 mm high, instrumented in the same manner as for the previously described concrete specimens. A reduced sample size was preferred in order to reach high stress levels and avoid technical problems with use of the triaxial press. Opting for smaller samples is fully justified when taking into account the very small size of heterogeneities in these materials.

2.5.1.1 Unconfined compression test

Figure 2.18 presents the results of simple compression tests performed on siliceous and limestone rocks. Both materials exhibits linear elastic behavior until the peak stress followed by a brittle failure. However, siliceous rock is much stiffer and reaches much higher strength than limestone rock.

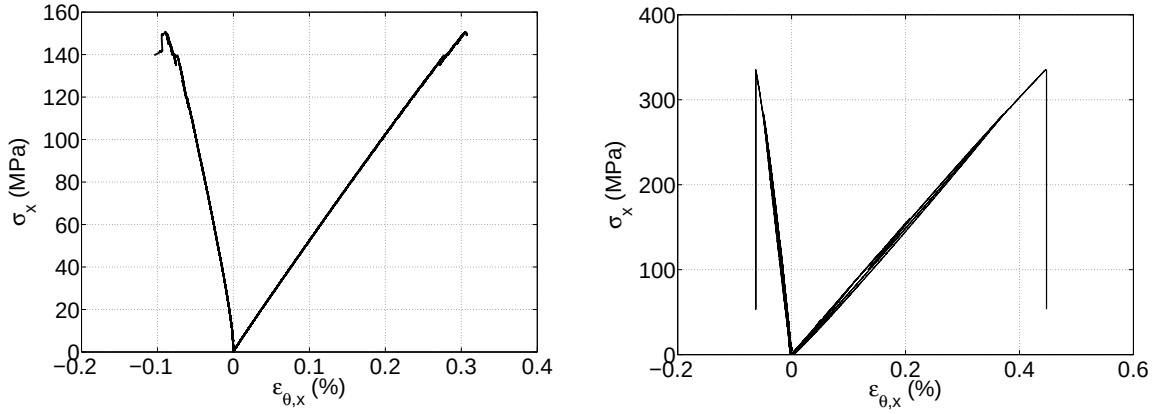

(a) (b)

Figure 2.18: Unconfined compression test on limestone (a) and siliceous (b) rock: axial stress σ_x vs. strain components ε_θ and ε_x

2.5.1.2 Triaxial compression

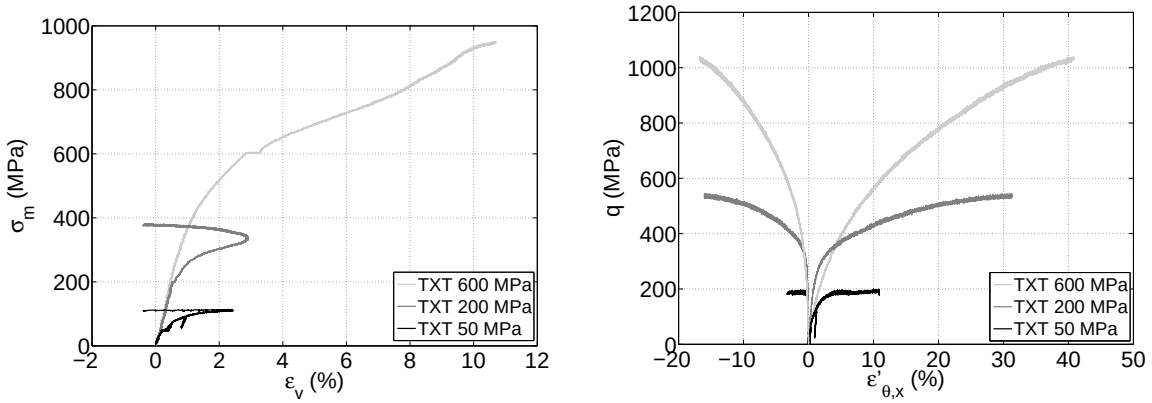

(a) (b)

Figure 2.19: Triaxial tests at different confining pressures performed on limestone rock;
(a) mean stress σ_m vs. volumetric strain ε_v
(b) stress deviator q vs. strain components ε'_θ and ε'_x

Figure 2.19(a) displays the volumetric behavior of limestone rock at different levels of confinement. The volumetric curve during hydrostatic phase is linear up to 200 MPa. Beyond this point, volumetric stiffness strongly decreases. At 50 MPa and 200 MPa of confinement, transition from contractant to dilatant behavior is observed. This state was not reached at 600 MPa of confining pressure. The high deformability of the rock exceeded the capacity of the machine and the gauges measure range. Of course, the volumetric behavior can not be analyzed after the orthoradial gauges signals are lost. At 600 MPa of confinement, the volumetric behavior in the deviatoric phase shows first an

important stiffness reduction, is followed by a stiffening, what may be attributed to the material densification.

Figure 2.19(b) presents the deviatoric behavior of limestone rock at different levels of confining pressure. The evolution of the material behavior with the confinement is similar to the one of cement-matrix composites. The increase of the loading capacity is observed as well as the transition from quasi-brittle behavior under uniaxial compression test, to ductile behavior with the peak stress in a form of plateau and to strain hardening at very high confinement.

Figure 2.20 presents the axial behavior of limestone and siliceous rocks tested at 50 MPa of confinement. The two rocks exhibit very different triaxial behavior. A much higher strength and stiffness of the siliceous rock in comparison with limestone is observed. The ultimate stress reached by the siliceous rock is nearly 1000 MPa. Volumetric behavior of quartzite sandstone presented in Figure 2.21(b) is bilinear up to 200 MPa of the mean stress. Beyond this point the increase of volumetric stiffness is observed until the transition from contractant to dilatant behavior which occurs a bit before the peak stress. After the peak stress material undergoes brittle failure along the shear plane and the specimen is cut into two parts (Fig. 2.22). On the contrary, the ductile behavior of the limestone rock corresponds to large deformations of the top part of the sample and several macrocracks distributed over the entire specimen. The corresponding image is presented in Figure 2.23(a). At very high confinement, limestone rock fails through large continuous deformations in the form of bar

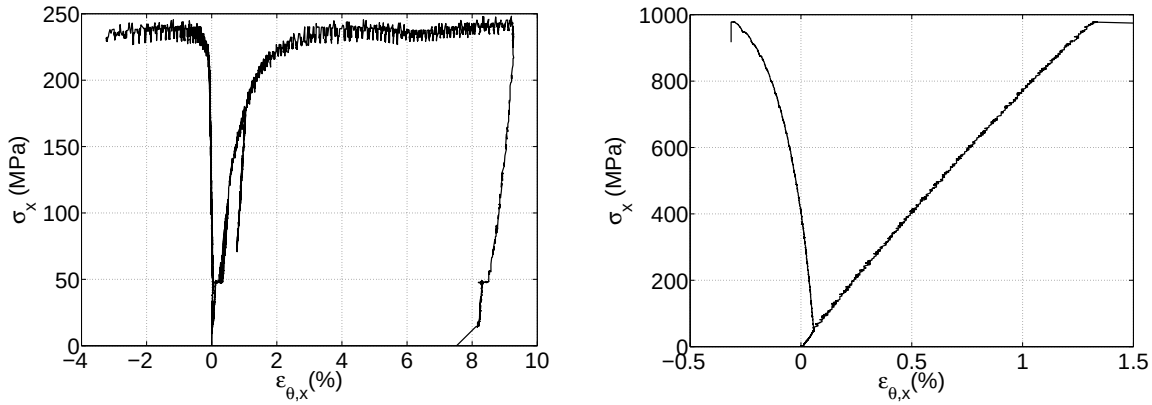

(a) (b)

Figure 2.20: Triaxial test at 50 MPa of confinement on limestone and siliceous rock: axial stress σ_x vs. strain components ε_θ and ε_x
(a) limestone rock
(b) siliceous rock (Poinard [48])

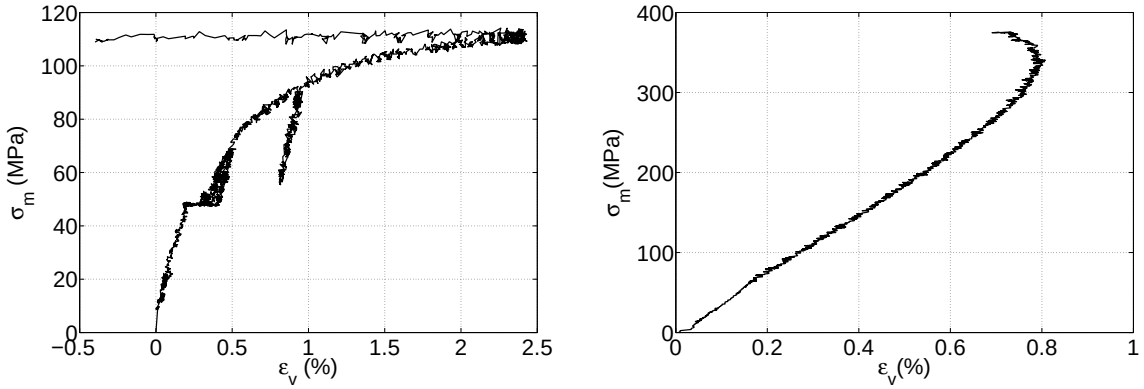

(a) (b)

Figure 2.21: Triaxial test at 50 MPa of confinement on limestone and siliceous rock: mean stress σ_m vs. volumetric strain ε_v
(a) limestone rock
(b) siliceous rock (Poinard [48])

Figure 2.22: Failure pattern of siliceous rock under triaxial compression at 50 MPa of confinement

(a) $p_c = 50$ MPa

(b) $p_c = 200$ MPa

(c) $p_c = 600$ MPa

Figure 2.23: Failure patterns in a limestone rock specimen after different triaxial compression tests

2.5.2 Results of triaxial tests performed on concretes

In the following discussion, a set of selected results from triaxial tests performed on the four types of concrete will be reviewed. On one hand, a comparison will be done between rolled siliceous aggregate concrete (SR) and glass ball concrete (GB) because their aggregate shape is comparable. On the other hand, concretes with crushed siliceous aggregates (SC) and with limestone aggregates (LC) will be compared.

2.5.2.1 Unconfined compression test

Figure 8 shows the results of uniaxial compression tests performed on concretes with siliceous aggregates and limestone aggregates. Two tests carried out on limestone aggregate concrete have provided consistent results. The Young's modulus and Poisson's ratio evaluated from the linear part of the axial behavior are respectively 22 GPa and 0.13; both these values are lower than those corresponding to the siliceous aggregate concrete (see Table 2.6). The Young's modulus values of concrete remain consistent with those of aggregates making up 40% of the concrete volume. The uniaxial strength, which lies between 55 and 59 MPa, is significantly higher than the corresponding value for siliceous aggregate concrete. Moreover, cracks pass through the limestone aggregates, whereas they tend to circumvent the siliceous aggregates (see Fig. 2.25). These observations confirm the importance of the interfacial transition zone in the uniaxial behavior of concrete. The stronger interfacial bond derived through the use of limestone aggregates is explained by its high porosity and absorption. In addition, some chemical bonding may take place between the limestone and the cement matrix due to a reaction between calcite in the aggregate and calcium hydroxide in the hydrated cement (Monteiro and Mehta [43]).

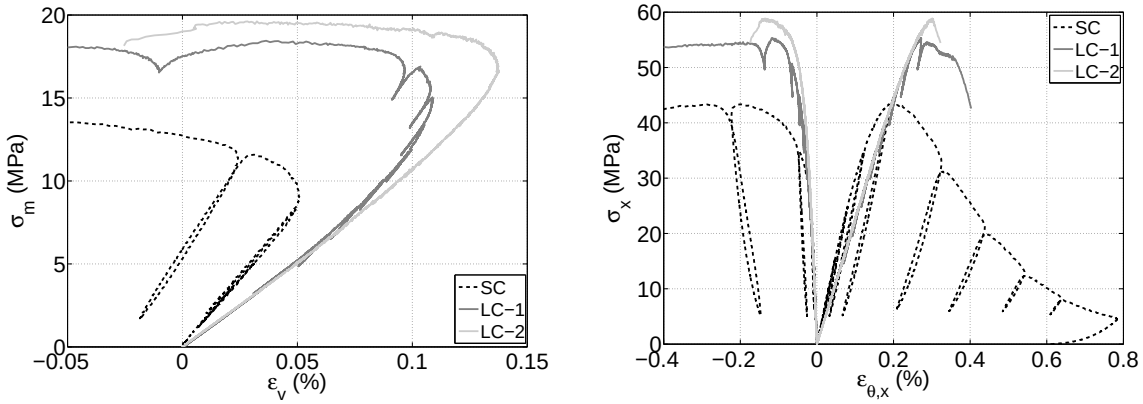

(a) (b)

Figure 2.24: Simple compression test on concretes with siliceous aggregates (SC) and limestone aggregates (LC);
(a) mean stress σ_m vs. volumetric strain ε_v
(b) axial stress σ_x vs. strain components ε_θ and ε_x

Concrete	**LC**	**SC**
Young's modulus, E $[GPa]$	22	33
Poisson's ratio, ν $[-]$	0.13	0.16
Compressive strength, σ_c $[MPa]$	57	43

Table 2.6: Classical concrete characteristics identified from simple compression test

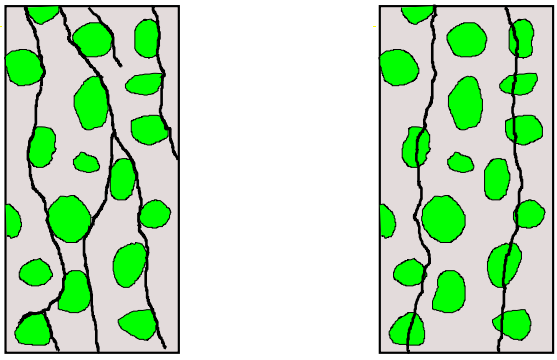

(a) (b)

Figure 2.25: Sketches of failure patterns in concrete samples at unconfined compression test
(a) siliceous aggregate concrete (SR, SC, GB)
(b) limestone aggregate concrete (LC)

2.5.2.2 Triaxial compression

Triaxial test at 50 MPa confinement

Figure 9 presents the axial behavior of concrete with rolled siliceous aggregates (SR) and glass balls (GB) tested under 50 MPa of confining pressure. The deviatoric strength of glass ball concrete is 24% higher than that of siliceous aggregate concrete. This ultimate stress difference is probably explained by the aggregate strength, which is considerably higher for glass balls than for siliceous aggregates. This strength difference protects glass ball aggregates from shear failure and moreover leads to a crack pattern completely different for glass ball concrete sample than that observed for the other concretes (see Fig. 6).

Figure 10 provides the results of triaxial test conducted at 50 MPa of confinement on siliceous aggregate concrete (SC) and limestone aggregate concrete (LC). The elastic volumetric stiffness is slightly higher for limestone aggregate concrete, which is consistent with the elastic properties of aggregates.

The stress-strain curve of the limestone aggregate concrete displayed in Figure 4.10(b) exhibits a plateau, whereas a peak stress occurs for the siliceous aggregate concrete. The maximum deviatoric stress reached by the siliceous aggregate concrete is about 11% higher than the maximum stress in limestone aggregate concrete. This finding is attributed to the composiiton of aggregates. Due to the strong interfacial bond and low aggregate strength in the LC sample, a large quantity of the aggregates is broken under shear loading; nonetheless, the decrease in strength due to the use of soft limestone aggregates

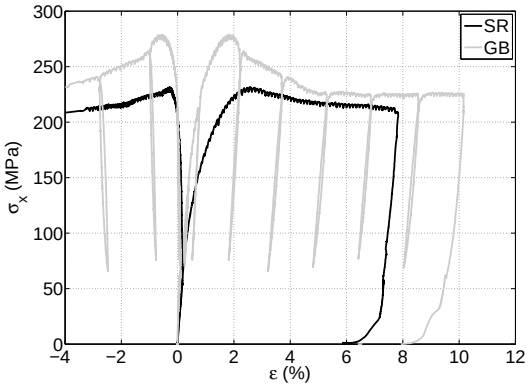

Figure 2.26: Triaxial test at 50 MPa of confinement on concretes with siliceous aggregates (SR) and glass balls (GB): axial stress σ_x vs. strain components ε'_θ and ε'_x

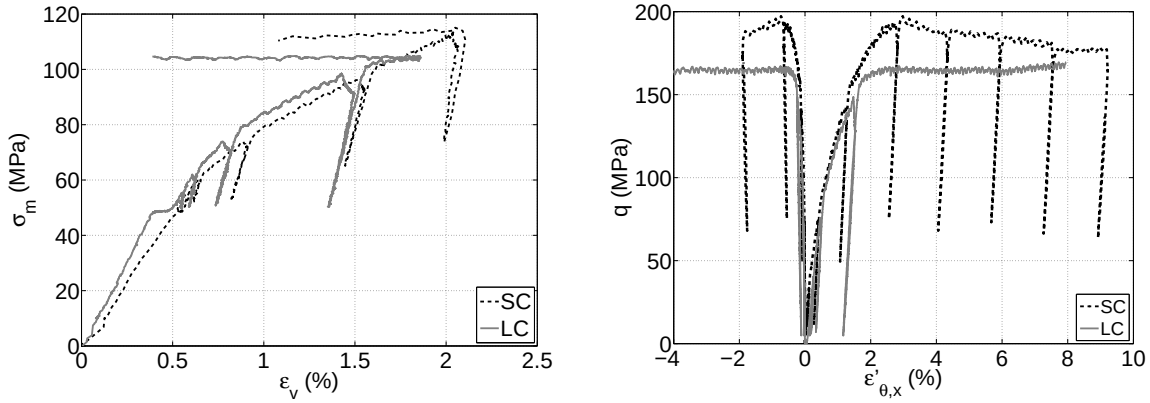

(a) (b)

Figure 2.27: Triaxial test at 50 MPa of confinement on concretes with siliceous aggregates (SC) and limestone aggregates (LC): (a) mean stress σ_m vs. volumetric strain ε_v, (b) stress deviator q vs. strain components ε'_θ and ε'_x

remains quite limited.

Triaxial test at 200 MPa confinement

Figure 11 displays the results of triaxial tests performed at 200 MPa of confinement on both siliceous aggregate concrete (SR) and glass ball concrete (GB). The volumetric stiffness of glass ball concrete is greater than that of siliceous aggregate concrete, an outcome due to the elastic properties of coarse aggregates, which make up some 40% of concrete volume. The Poisson's ratio ν of glass is much higher than that of siliceous rock, while their Young's modulus values E are comparable. These two characteristics control the elastic bulk modulus of the material K, such that:

$$K = \frac{E}{3(1-2\nu)} \tag{2.5}$$

Figure 4.11(b) reveals that the maximum deviatoric stress is exactly the same for rolled aggregate concrete and glass ball concrete. The tangential stiffness is nearly the same for both samples. At this level of confinement, the cement matrix loses its cohesive nature. The test has also revealed that the greater strength of coarse aggregates does not increase the deviatoric strength of concrete when the cement matrix is heavily damaged. This point was also confirmed by the triaxial compression test conducted at 650 MPa (Fig. 4.7(b)).

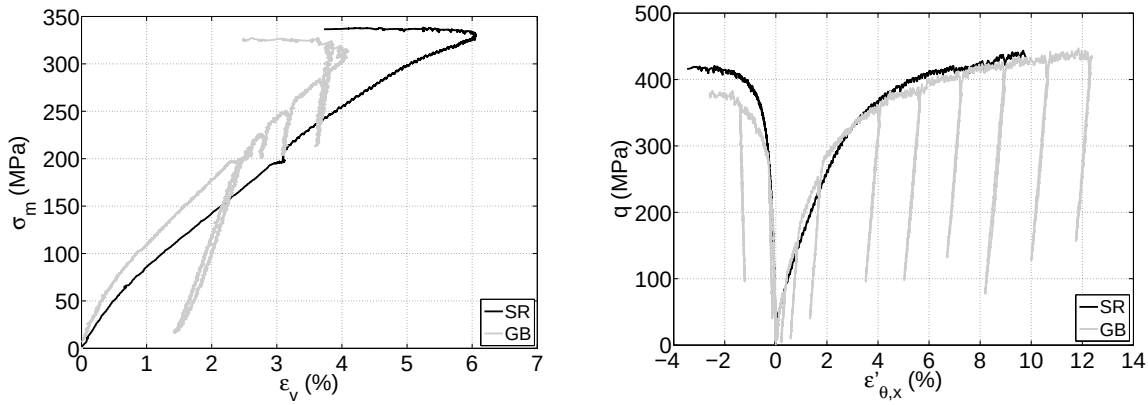

(a) (b)

Figure 2.28: Triaxial test at 200 MPa of confinement on concrete with siliceous aggregates (SR) and glass balls (GB): (a) mean stress σ_m vs. volumetric strain ε_v, (b) stress deviator q vs. strain components ε'_θ and ε'_x

Due to a lack of results for siliceous crushed aggregate concrete at 200 MPa of confinement, the limestone aggregate concrete (LC) will be compared with siliceous rolled aggregate concrete (SR). Figure 12 shows the results of triaxial testing performed at 200 MPa of confinement on these two concretes. In agreement with test results at 50 MPa, volumetric stiffness is slightly higher for limestone aggregate concrete at the beginning of the loading step. Beyond a mean stress of 50 MPa, a reduction in stiffness can be observed and thereafter the volumetric strain becomes higher for LC. This stiffness reduction is attributed to a gradual damage and compaction process (porosity closure) of the cement

matrix in both concretes. The reduction is even more pronounced in LC since at this level of mean stress, soft limestone aggregates undergo additional large plastic deformations due to their own porosity closure.

During the deviatoric phase, the behavior of siliceous aggregate concrete is considerably stiffer. Nevertheless, both concretes reach the same stress level. Aggregate strength does not affect the maximum deviatoric stress at this level of confinement.

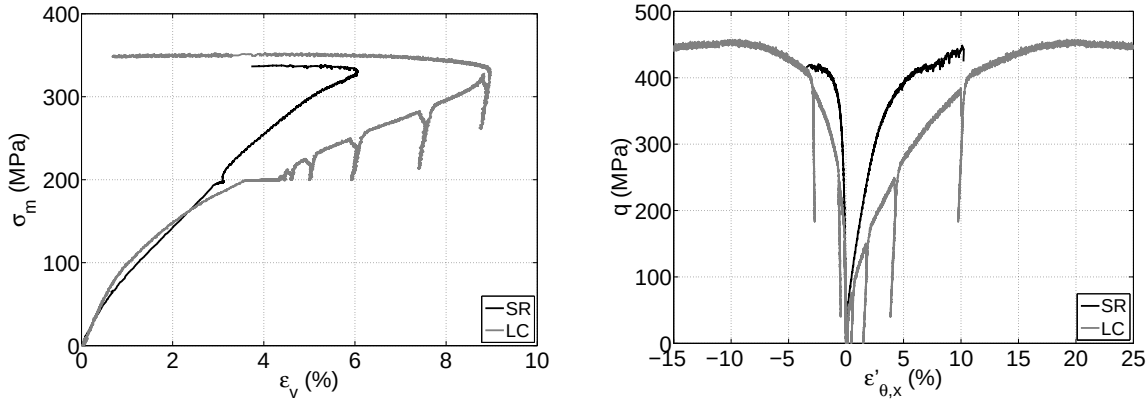

(a) (b)

Figure 2.29: Triaxial test at 200 MPa of confinement on concrete with siliceous aggregates (SR) and limestone aggregates (LC): (a) mean stress σ_m vs. volumetric strain ε_v, (b) stress deviator q vs. strain components ε'_θ and ε'_x

Triaxial test at 650 MPa confinement

Figure 13 presents the results of triaxial tests performed at 650 MPa of confinement on concrete with siliceous aggregates (SR) and glass ball concrete (GB). These tests demonstrate that the difference in volumetric strain is significant only at low confinement levels. Beyond 200 MPa of confinement, the tangential volumetric stiffness of the two test concretes are nearly identical. For such a confinement range, the differences in aggregate elastic properties are probably compensated by compaction of the cement matrix.

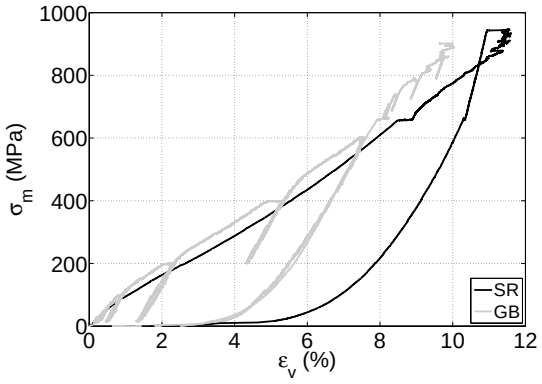

Figure 2.30: Triaxial test at 650 MPa of confinement on concretes with siliceous aggregates (SR) and glass balls (GB): mean stress σ_m vs. volumetric strain ε'_v

The results of triaxial compression conducted at 650 MPa of confinement on concretes with siliceous aggregates (SC) and limestone aggregates (LC) are showed in Figure 14. The limestone aggregate concrete was first loaded hydrostatically up to a pressure of 650 MPa. Due to a technical problem, the subsequent triaxial part, *i.e.* after the unloading and hydrostatic reloading, was performed at 600 MPa of confining pressure. The volumetric strain is much higher for limestone aggregate concrete, a finding that may be explained by the high porosity of the rock.

Figure 4.14(b) shows that tangential stiffness during the deviatoric phase is nearly the same for both samples. A large part of the limestone porosity was probably closed during the hydrostatic part of loading which would stiffen the limestone aggregates to a greater extent than for the 200-MPa test. To compare the maximum deviatoric stresses which are highly dependent on confining pressure, we analyzed a test conducted on rolled siliceous aggregate concrete at a 600-MPa confining pressure: the resulting deviatoric stress of 830 MPa exceeds the maximum deviatoric stress reached by the limestone aggregate concrete (730 MPa).

2.5.2.3 Limit states and failure patterns

Previously presented relative representation of the limit states is completed with the limit states of limestone aggregate concrete in Figure 2.32. High stress reached by the limestone aggregate concrete under unconfined compression test confirms the important role of the interfacial strength for such loading path. It can be observed that at low

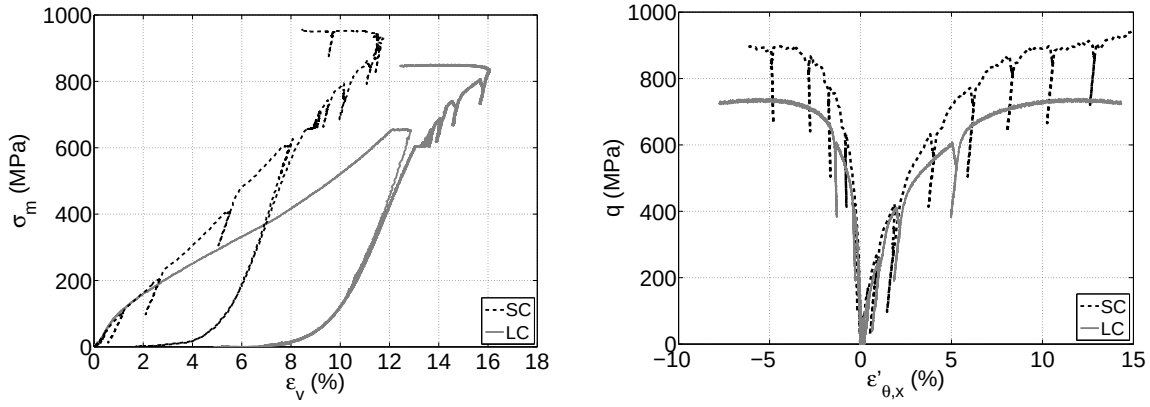

Figure 2.31: Triaxial test at 650 MPa of confinement on concretes with siliceous aggregates (SC) and limestone aggregates (LC): (a) mean stress σ_m vs. volumetric strain ε_v, (b) stress deviator q vs. strain components ε'_θ and ε'_x

and intermediate level of confinement the aggregate strength has almost no influence on the concrete limit states. The deviatoric stresses at the maximum compaction states are close for limestone aggregate concrete and siliceous aggregate concrete. In contrast, at high confinement the lower aggregate strength seems to reduce the concrete deviatoric strength.

Failure patterns

Figure 2.33(a) shows an image of limestone aggregate sample after the test at 50 MPa of confinement. An important increase of specimen diameter is observed as well as localized deformation. Two x-shaped shear bands crossing the whole volume of the specimen are clearly visible with a few smaller inclined cracks. Similarly to the reference concrete a specimen failure is induced by the shear stresses in a highly deformed region.

The final failure pattern of the specimen tested at 200 MPa of confining pressure is illustrated in Figure 2.33(b). One horizontal crack that passes through both mortar and aggregates is observed. At 650 MPa of confinement (Fig. 2.33(c)) a branching crack is produced: with one horizontal branch and one inclined branch. Similarly to the results at 200 MPa, the crack passes through both mortar and aggregates.

Aggregates composition thus strongly influences the failure pattern in concrete samples at high confinement (see Fig. 2.34). In limestone aggregate concrete, a single crack passing through both mortar and aggregates appears, while few horizontal cracks, along with predominantly debonded aggregates are observed in siliceous aggregate concrete as well as glass ball concrete specimens.

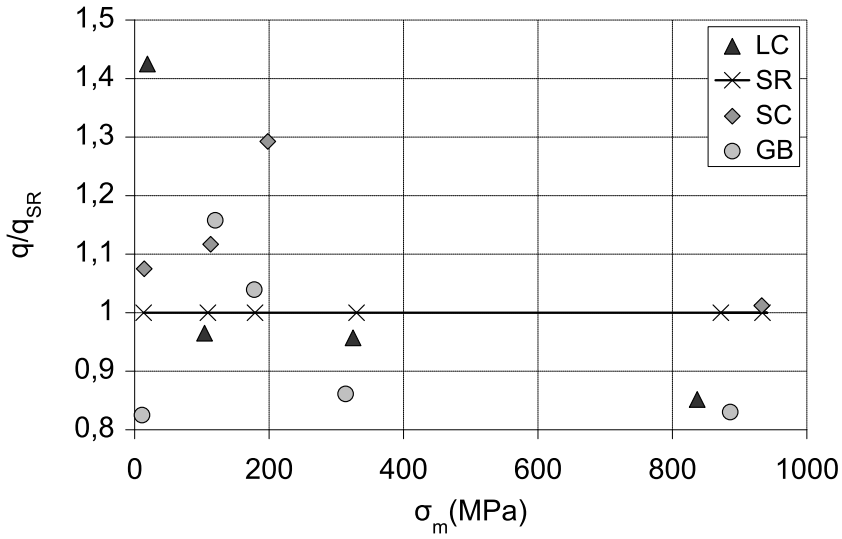

Figure 2.32: Limit states of concretes with siliceous rolled aggregates (SR), siliceous crushed aggregates (SC), glass balls (GB) and limestone aggregates (LC): relative deviator q/q_{SR} vs. mean stress σ_m; q_{SR} is the deviatoric stress associated with the limit state of concrete with siliceous rolled aggregates

(a) $p_c = 50$ MPa (b) $p_c = 200$ MPa (c) $p_c = 650$ MPa

Figure 2.33: Failure patterns in LC specimen under different triaxial compression tests

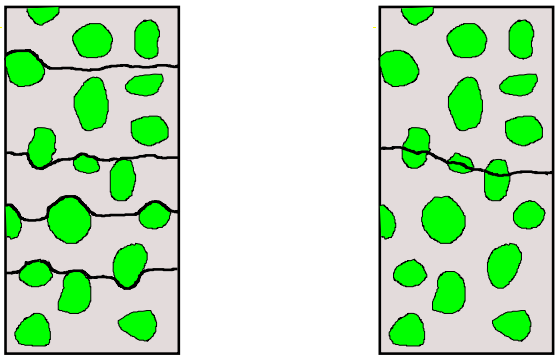

(a) (b)

Figure 2.34: Sketches of failure patterns in concrete samples at high confinement (>200 MPa)
(a) siliceous aggregate concrete (SR, SC, GB)
(b) limestone aggregate concrete (LC)

2.6 Chapter conclusion

This experimental investigation examined the effects of coarse aggregates on concrete behavior under high triaxial loading. Triaxial tests were performed at confining pressure levels between 0 and 650 MPa on four concretes distinguished only by the type of coarse aggregate. The influence of aggregate shape was first evaluated on three of the concretes, containing rolled aggregates, crushed aggregates and glass balls. Next, concretes with siliceous aggregates, glass aggregates with limestone aggregates were introduced to study the influence of aggregate composition. Concretes with similar aggregate shapes were compared in pairs: glass ball concrete was compared with siliceous rolled aggregate concrete, and then siliceous crushed aggregate concrete was compared with limestone crushed aggregate concrete. Table 2.7 summarizes main observations of this study.

Confining pressure p	**Aggregates shape**	**Aggregates composition**
0 MPa	+ strength of ITZ	+
50 MPa	+ irregular shape	+ strength elastic properties
100 MPa	+ irregular shape	
$\geq$ 200 MPa	-	+ porosity strength

Table 2.7: Effect of aggregate properties on concrete behavior at different levels of confining pressure

The aggregate/mortar interface strength proved to be the main factor governing the behavior of concrete in an unconfined compression test. This phenomenon is well-known for ordinary concrete, in which aggregate strength is much greater than mortar strength. Irregularly-shaped coarse aggregates slightly increase the strength generated at the aggregate/mortar interface.

At moderate confinement levels (50 MPa), the shear strength of concrete is mainly controlled by the aggregate strength; however, along the same lines as what was observed for unconfined compression, rough angular aggregates enhance the concrete strength.

At high confinement ($\geq$ 200 MPa), the shear strength of concrete seems to be controlled by the compacted cement matrix provided aggregate strength sufficiently higher than the mortar strength. Otherwise, a lower-strength aggregate reduces overall concrete strength at very high confinement (600 MPa). The coarse aggregate shape does not therefore seem to exert any influence under high confinement.

Chapter 3

Numerical modeling at the mesoscopic scale

Different approaches to concrete modeling at the meso-scale were presented in the bibliographic review. Extensively developed in the last few years, discrete-based models provide a suitable framework for modeling of geomaterials. They handle the discontinuous and heterogeneous nature of the material, which induces the complex mechanical behavior. The model proposed in this work combines the cohesive DEM (Delenne *et al.* [20] with a lattice-type discretization of the material, which means that discrete elements are the material points belonging to each phase instead of rigid body particles. A 2-D approach is adopted for reducing time and computational cost. The aim is to reproduce at least in a qualitative sense different phenomena that occur in concrete at the mesoscopic level.

The first section of this chapter will provide a description of the model. In the second part, the response of the model under biaxial stresses will be presented. The influence of confining pressure on the numerical macroscopic response will be examined by comparison with experimental measurements.

3.1 Discrete model of concrete

3.1.1 Principles of the method

Concrete is modeled as a material composed of aggregate particles, cement matrix and voids. The space is discretized as a regular or disordered triangular grid of points (nodes) connected by line elements (bonds), which exhibit a cohesive character. Each bond can transfer normal force and tangential force up to a given force threshold. Upon failure, cohesive bond is replaced by the standard frictional contact. A line element can thus be in two different states, bond or contact. The bond to contact switch at the microscopic level is translated to damage, at the macro-level.

The aggregates and voids are randomly distributed over the specimen's area. The distribution procedure will be described in section 3.2.1. Mechanical properties of the lattice elements depend on the type of the connected nodes, that is their positions in the three-phase medium (Fig. 15). Nodes belonging to the void phase are removed and the following types of lattice bonds are distinguished:

- aggregate (a): two nodes placed in the same aggregate
- matrix (m): two nodes placed in the matrix
- interface aggregate-matrix (am): one node placed in the matrix and one in the aggregate

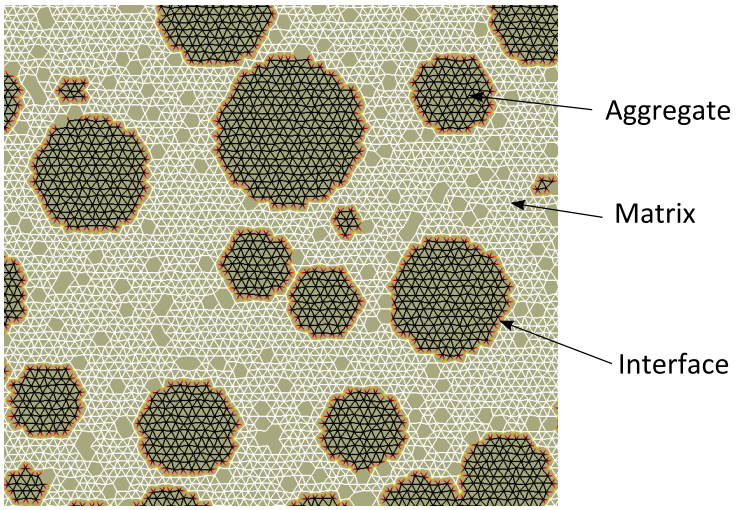

Figure 3.1: An example representation of a three-phase medium by the triangular lattice

Once the sample is discretized, the collection of material points connected by bonds is submitted to some external loading. The calculation algorithm executed at each time step is the following:

- Actualization of the positions and velocities of each node
- Application of the contact law in order to determine the interaction forces
- Computation of the accelerations from the resultant forces acting on each node using the Newton's second law.

To take into account the compaction phenomenon, characteristic for cement matrix materials and corresponding to the porosity closure, the list of bonds is updated during the simulation time. However, instead of the cohesive law, usual contact and dry friction law are applied to the new bonds.

3.1.2 Behavior of the lattice elements

Material is represented by a grid of nodes connected by cohesive bonds. Kinematics of the nodes is described in the global frame $(0,\vec{x},\vec{y})$. N_i is the position of the node i. The nodes can undergo both translation and rotation. In order to reproduce rotational movements, a rotation angle θ_i is defined for each node i. The material contact points, P_i and P_j, attached to nodes i and j respectively, are defined in the mid-point between two adjacent nodes (i and j) in the initial configuration. At this reference state, the contact points corresponding to the two interacting nodes coincide (Fig. 3.2(a)). The positions

of these points change with deformations of sample (Fig. 3.2(b)). The local displacement characterizing the cohesive bond is described in a local orthonormal frame ($\vec{n}$, $\vec{t}$). The normal vector of the contact between two nodes is defined by:

$$\vec{n} = \frac{\overrightarrow{N_j N_i}}{\|\overrightarrow{N_j N_i}\|} \tag{3.1}$$

For a node i we denote $\vec{v}_i$ its velocity and $\vec{\omega}_i$ its angular velocity. Then, the normal and tangential components of the relative velocity of two interacting nodes i and j are:

$$\begin{aligned} v_n^{rel} &= (\vec{v}_j - \vec{v}_i) \cdot \vec{n} \\ v_t^{rel} &= (\vec{v}_j - \vec{v}_i) \cdot \vec{t} + \tfrac{1}{2}(\|\overrightarrow{N_j N_i}\|\omega_j + \|\overrightarrow{N_i N_j}\|\omega_i) \end{aligned} \tag{3.2}$$

The total displacement is decomposed into a normal component d_n and tangential component d_t, expressed by:

$$d_n = \|\overrightarrow{N_j^0 N_i^0}\| - \|\overrightarrow{N_j N_i}\| \tag{3.3}$$

$$d_t = \overrightarrow{P_j P_i} \cdot \vec{t} \tag{3.4}$$

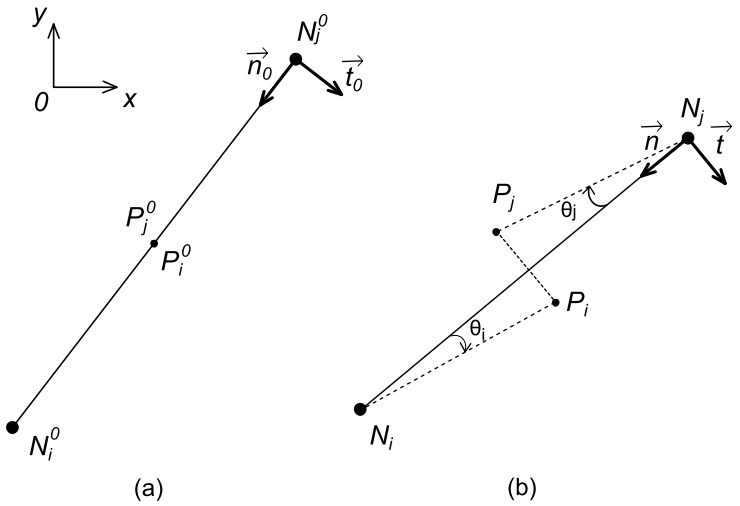

Figure 3.2: Local displacements involved in a bond: (a) initial state, (b) deformed state

The corresponding mechanical actions are the normal force $\vec{F_n}$ and the tangential force $\vec{F_t}$ calculated using the local stiffness parameters, k_{n_comp}, k_{n_trac} and k_t, corresponding to the phase represented by the bond. Therefore, the force-displacement relationships are:

$$F_n = \begin{cases} k_{n\_comp} d_n, & \text{if } d_n \geq 0 \text{ (contraction)} \\ k_{n\_trac} d_n, & \text{if } d_n < 0 \text{ (extension)} \end{cases} \tag{3.5}$$

In our simulations k_{n_comp} and k_{n_trac} have the same value and will be simply denoted k_n.

$$F_t = k_t d_t \tag{3.6}$$

A local failure criterion governs the transition between the cohesion state and the sliding-contact state. The failure may occur either in tension or in shearing. The criterion is expressed through a power-law function in the form of:

$$\zeta = \left| \frac{F_t}{F_t^0} \right|^n + \frac{F_n}{F_n^0} - 1 = 0 \tag{3.7}$$

where F_n^0 and F_t^0 are the tangential yield force and normal yield force respectively.
The exponent n controls the shape of the curve $\zeta = 0$ (Fig. 16). As a first guess it was set to 5. We will see in the next chapter that the rupture criterion (exponent n and $\frac{F_t^0}{F_n^0}$ ratio) plays an important role in the mechanical behavior at high confining pressure.

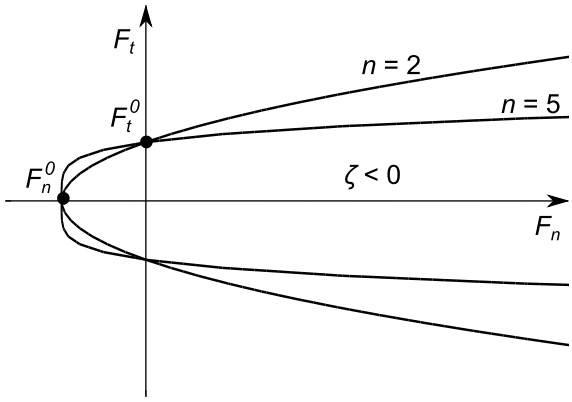

Figure 3.3: Failure criterion for cohesive interactions

A cohesive bond between two nodes is active for $\zeta < 0$, otherwise the bond fails and the contact becomes frictional without cohesion. The same contact law is used for both contacts originated from bond rupture and "new contacts", not existing before as bonds, detected during the simulation. A linear elastic law is used to describe the normal contact interaction:

$$F_n = \begin{cases} k_n d_n, & \text{if } d_n \geq 0 \\ 0, & \text{if } d_n < 0 \end{cases} \tag{3.8}$$

with the normal stiffness of the contact k_n.

The tangential component of the contact force is determined using an elastic-plastic formulation. The force is incremented at each time step i using the tangential contact stiffness k_t, relative sliding velocity at the contact point v_t^{rel} and the value of the time step Δt:

$$F_t^i = F_t^{i-1} + k_t v_t^{rel} \Delta t \tag{3.9}$$

The plastic threshold is imposed by the Coulomb criterion:

$$|F_t| \leq \mu F_n \tag{3.10}$$

where μ is the friction coefficient.

3.1.3 Motion integration

In order to describe the evolution of the system, the positions and velocities of each node are updated at each time step by integrating the Newton's 2nd law (4.16), once the resultant forces are known.

$$m_i \frac{d^2\vec{x}_i}{dt^2} = \vec{F}_i, \qquad i = 1, ..., N \tag{3.11}$$

where N is the number of nodes, m_i is the mass of the node i, $\vec{x}_i$ is its position, and $\vec{F}_i$ is the resultant force acting on this node.

Positions, velocities and accelerations of nodes at time t are used to compute the positions at time $t + \Delta t$. An explicit algorithm, named Velocity Verlet, is used:

$$\vec{x}_i(t + \Delta t) = \vec{x}_i(t) + \vec{v}_i(t)\Delta t + \frac{1}{2}\vec{a}_i(t)\Delta t^2 \tag{3.12}$$

Computation of the velocities is made in two stages. The half-step velocities are first calculated:

$$\vec{v}_i(t + \frac{1}{2}\Delta t) = \vec{v}_i(t) + \frac{1}{2}\vec{a}_i(t)\Delta t \tag{3.13}$$

Then, the accelerations at time $t + \Delta t$ are calculated using the interaction efforts determined from positions $\vec{x}_i(t + \Delta t)$ and half-step velocities $\vec{v}_i(t + \frac{1}{2}\Delta t)$. Finally, velocities at time $t + \Delta t$ are obtained using the formula:

$$\vec{v}_i(t + \Delta t) = \vec{v}_i(t + \frac{1}{2}\Delta t) + \frac{1}{2}\vec{a}_i(t + \Delta t)\Delta t \tag{3.14}$$

It is assumed that the contact forces are exerted at the contact points, P_i and P_j. This implies an existence of the torque acting on the two nodes:

$$\begin{array}{l} \vec{\Gamma}_{ij} = 0.5\overrightarrow{N_iN_j} \times \vec{F} \\ \vec{\Gamma}_{ji} = 0.5\overrightarrow{N_jN_i} \times (-\vec{F}) \end{array} \tag{3.15}$$

These torques modify the angular velocities of the nodes. Thus, it is necessary to add to equation 4.16 the equations for the angular coordinates of the grains:

$$I_i \frac{d\vec{\omega}_i}{dt} = \vec{\Gamma}_{ij} \tag{3.16}$$

where I_i is the moment of inertia of node i.

Choice of the time step

The stability of the explicit integration scheme depends on the time step. It must be smaller than a critical time step related to the maximum angular frequency ω of the system. For single mass-spring system described by a point mass, m, and spring stiffness, k, the critical time step is:

$$\Delta t_{crit} = \frac{2}{\omega} \qquad \text{with} \qquad \omega = \sqrt{\frac{k}{m}} \tag{3.17}$$

The system modeled can be seen as a two-dimensional collection of nodes, having the same mass, and springs with different stiffness. The time step is estimated in a simplified manner using the highest stiffness k_{max} and a safety coefficient p as follows:

$$\Delta t = p\sqrt{\frac{m}{k_{max}}} \tag{3.18}$$

with $p = 0.05$.

3.1.4 Damping

In numerical simulations, we often seek to reach a static equilibrium state of the numerical sample from an initial, non-balanced state. From this initial state, dynamic evolutions of the system should lead to the final static state. If no plastic mechanisms occur in the sample (for example, no sliding takes place in any interaction), the system would oscillate forever between two extreme states and no final equilibrium state would be reached. To avoid this, damping forces are added to resultant forces in the Newton's law (equation 4.16). Consequently, some energy is always dissipated, so that equilibrium states could be easier obtained. Different kinds of damping can be used.

"Viscous" damping, used by Cundall & Strack [16], introduces forces proportional and oposite to the velocities of each node. A drawback of such damping is that it could perturbate simulations where a steady flow (with constant non-null velocities) is aimed. Viscous damping forces can be introduced also as contact forces at each interaction (depending in this case on the relative velocities of the nodes), as done by Iwashita and Oda [35]. However, this might be disturbing if the physics of the real interaction that is simulated does not include viscous aspects.

"Local" damping, as proposed by Cundall [15], introduces damping forces proportional to the accelerations of the nodes and opposite to their velocities. The i-th component of damping force $\vec{F^d}$ added to the resultant force acting on each node $\vec{F}$ is expressed by:

$$F_i^d = -D\,|\Sigma F_i|\,sign(v_i) \tag{3.19}$$

where $sign(v_i)$ is equal to 1 if $v_i \geq 0$, else -1.
This local damping is not added as soon as acceleration vanishes, even if velocities are non-null.

In all cases, damping forces correspond generally to nothing real; therefore, it has to be checked that they do not modify the obtained mechanical states.

The local damping is used in our simulations with $D = 0.7$. For example, this coefficient equals 0.8 in some commercial codes (Itasca).

3.2 Application of the model to confined compression tests

3.2.1 Numerical concrete sample

First step of creation of a numerical sample consists in generating a regular triangular grid of points (nodes), which initially are of the matrix type. Initial distance between the nodes was set to $\ell = 5 \cdot 10^{-}4$ m. It corresponds to 1/80 of the sample's size (40 mm per 40mm), which is a compromise between the calculation time and a realistic representation of the material mesostructure.

The circular aggregates are then randomly placed into the specimen, following an aggregates size distribution curve and an aggregate fraction. A normal distribution of particle sizes is used, with a mean diameter of 7 mm (14ℓ) and a standard deviation of 2 mm (4ℓ). This aggregate size is of the order of experimental values. Aggregate particles occupy about 45% of the sample's area. This input value corresponds to the area of spherical aggregates, not to the number of aggregate bonds or nodes. The aggregate distribution procedure is an iterative process. A random position and diameter of an aggregate are chosen and the potential superposition with already existing aggregates is verified. If there is no superposition, the nodes belonging to the aggregate's area become the aggregate type. The process is repeated until the desired area of aggregates is reached.

A similar procedure is applied to distribute voids over the specimen. Mean diameter of voids is 0.5 mm (ℓ) and a standard deviation equals to 0.25 mm (0.5ℓ). Voids area occupies about 8% of the sample's area. The superposition with previously placed aggregates and voids is checked and avoided. If there is no superposition, the nodes belonging to the void's area are removed. Taking into account the length scale, this porosity can be considered as macroporosity.

Subsequently, the remaining nodes are connected to form a triangular lattice. Depending on the type of the connected nodes different mechanical properties, corresponding to the mortar, the aggregate and the interface, are assigned to the lattice elements.

At the end, in order to introduce a mesh disorder a random deviation over all positions of nodes is performed. As illustrated in Figure 3.4, each node is randomly replaced within the square centered on its original position and of size $2\alpha\ell$; ℓ is the initial length of bonds and α is the perturbation coefficient: $0 \leq \alpha \leq 1$. It is however important to stress that this disorder in the node positions induces better isotropy of the bond orientations while the heterogeneity of the material stiffness is increased. The latter is desired but unfortunately hard to control.

The sample used in this study consists of 6350 nodes (6521 before removing empty nodes) what results in 18301 lattice bonds. The percentage of different type bonds is presented in table 3.1.

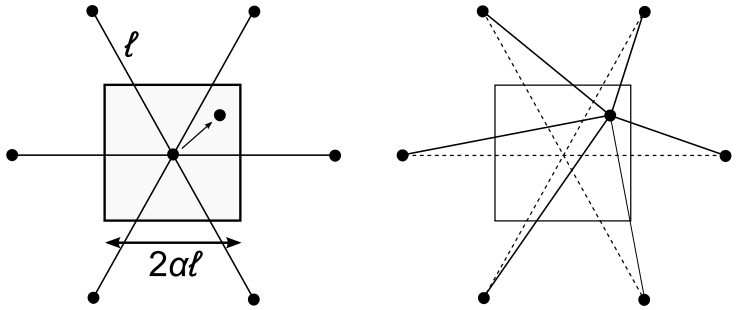

Figure 3.4: Irregular mesh obtained by a random deviation of the nodes positions within a square area

Type of elements	**Percentage**
Mortar	(10149) 53%
Aggregate	(6813) 35%
Interface	(1339) 7%
Voids (removed links)	(939) 5%

Table 3.1: Percentage of different type line elements in a concrete sample

3.2.2 Boundary conditions

Boundary conditions are applied directly on the outer nodes of the specimen. The horizontal displacement of the left boundary nodes and the vertical displacement of the bottom nodes are constrained. Biaxial loading is applied in two steps.

First, the sample is isotropically compressed until the desired pressure p_c is reached. Then, it is subjected to vertical load while keeping the lateral pressure constant.

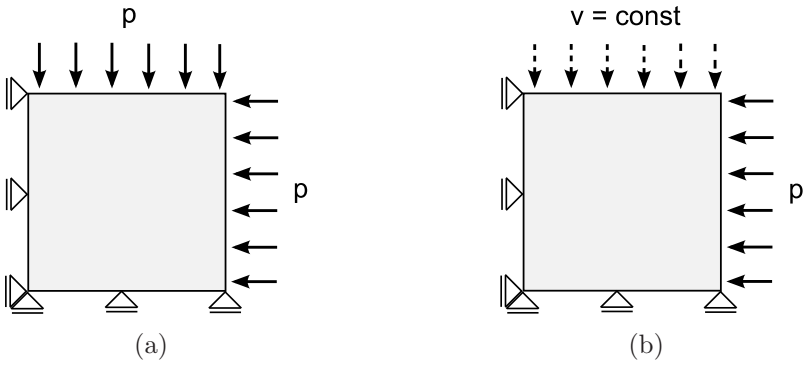

Figure 3.5: Schematic presentation of boundary conditions during (a) isotropic part and (b) deviatoric part of the loading

During the first phase (Fig. 3.5(a)), a force is applied incrementally on each node belonging to the top and the right boundaries of the sample. The sum of these forces divided by the size of the related specimen side corresponds to the intended pressure. The pressure increment δp equals 0.1 kPa per time step.

During the second phase (Fig. 3.5(b)), a force is applied on nodes belonging the right boundary in order to keep the lateral pressure equal to p_c and a constant velocity is applied on the top boundary nodes.

Since the study concerns the material behavior in quasi-static conditions, the axial loading rate $\dot{\varepsilon}$ must be sufficiently small to ensure the absence of dynamic effects. On the other hand, the loading rates which are used in the laboratory tests would lead to a very long computation time. Thus, the axial strain rate $\dot{\varepsilon} = 0.25$ was chosen as a good compromise to provide reasonable computation time and eliminate dynamic effects. Figure 3.6 presents deviatoric behavior under 100 MPa of confining pressure at different strain rates and proves that decreasing strain rate below the chosen value does not change significantly the material response.

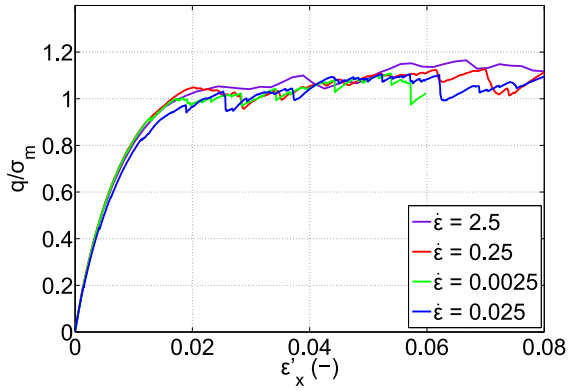

Figure 3.6: Biaxial compression performed with different strain rates: stress deviator q vs. axial strain ε_x

An other indicator that may be used to check that dynamic effects are negligible in such numerical simulations is inertial number I (GDR MiDi [32], Roux and Chevoir [53]), that I expresses the ratio of the inertial forces to imposed forces as follows:

$$I = \dot{\varepsilon}\sqrt{\frac{m}{p_c}} \tag{3.20}$$

where m is the mean mass at the nodes and p_c is the confining pressure. $I \to 0$ corresponds to the quasi-static state. In the following simulations the inertial number is lower than $7 * 10^{-6}$.

3.2.3 Determination of model's parameters

In order to perform simulations, a set of parameters describing the material must be determined: size of lattice elements ℓ, mass density ρ, contact stiffness k_n and k_t, cohesion forces F_n^0 and F_t^0, and friction coefficient μ.

The behavior of contacts is determined using some dimensionless parameters (Roux and Chevoir in [52]). A stiffness parameter κ is used to calculate the normal stiffness k_n

for a given confining pressure p_c. K compares k_n to the stress level (confining pressure) p_c and it is defined in 2D by:

$$\kappa = \frac{k_n}{p_c} \tag{3.21}$$

As a baseline, $\kappa = 500$, corresponds approximately to an assembly of wood cylinders, 6 cm long, tested under 50 kPa of the confining pressure (Combe [12]).

In order to estimate the level of stiffness for a concrete sample under confining pressures used in the present study, a formula 3.22 proposed by Combe [12] is used. κ is defined for a 3D assembly of monodisperse spheres and the interactions between the spheres are calculated using the Hertz law (Johnson [37]).

$$\kappa = \left[\frac{3\pi}{8(1-\nu^2)^2\phi_0 z}\right]^{1/3} \left(\frac{E}{p_c}\right)^{2/3} \tag{3.22}$$

where:
- E and ν are the Young's modulus and the Poisson's ratio of the material constituting the spheres
- p_c is the confining pressure
- ϕ_0 is the density of an assembly of monodisperse spheres
- z is the coordination number

The highest density of a close-packing of monodisperse spheres is $\phi_0 = 0.74$ and the coordination number is $z = 12$. Taking $E = 25$ GPa and $\nu = 0.2$, we obtain for concrete at 50 MPa of confinement $\kappa \simeq 40$.

This value is somewhat approximative but gives an order of magnitude of the stiffness level in concrete at that confining pressure. It was thus a starting point to deduce the normal stiffness k_n in a numerical sample, submitted to 50 MPa of confining pressure. This point is essential for high confining pressures to be correctly encountered in the simulation: high confinements are expressed by small κ. Comparison of elastic stiffness of experimental specimen with that of numerical sample led to a change in k_n and thus modification of κ from 40 to 250. In our simulations, κ varies from about 20 for 650 MPa confining pressure to 250 for 50 MPa of confining. These values remain close to the ones estimated from the equation 3.22.
Tangential stiffness k_t was set arbitrarily to $k_t = 0.65k_n$.

Another indicator, a cohesion number η is used to characterize the intensity of cohesion forces compared to the level of confining pressure:

$$\eta = \frac{F_n^0}{d \cdot p_c} \tag{3.23}$$

where d is a mean particle size. In this study, a mean length of the lattice bonds is taken instead. When $\eta \ll 1$, the confining forces dominate and the effect of cohesion is very small. In the opposite case, when $\eta \gg 1$, the effect of cohesion forces is predominant. The estimation of cohesion forces was set to best approximate the experimental results. Corresponding η varies from about 0.4 for $p_c = 50$ MPa to 0.03 for $p_c = 650$ MPa for a

mortar phase. As an initial guess, tangential cohesion force is taken the same as normal cohesion force, $F_t^0 = F_n^0$.

Due to the mesoscopic character of the model, the contact parameters are determined for three phases: matrix, aggregate and mortar/aggregate interface. In this chapter, aggregates are chosen three times stiffer than mortar (3.24), what corresponds approximately to the ratio of their Young's modulus in a reference concrete. Cohesion forces in aggregates are chosen 10 times higher than in mortar (3.25). Interface elements have the same elastic parameters as mortar elements (3.26) but they are differentiated by a lower cohesive threshold (3.27). The friction coefficient μ is arbitrarily set to 0.3 for all phases.

$$\frac{k_n^a}{k_n^m} = \frac{k_t^a}{k_t^m} = 3 \tag{3.24}$$

$$\frac{F_n^{0a}}{F_n^{0m}} = \frac{F_t^{0a}}{F_t^{0m}} = 10 \tag{3.25}$$

$$\frac{k_n^{am}}{k_n^m} = \frac{k_t^{am}}{k_t^m} = 1 \tag{3.26}$$

$$\frac{F_n^{0am}}{F_n^{0m}} = \frac{F_t^{0am}}{F_t^{0m}} = 0.2 \tag{3.27}$$

3.2.4 Postprocessed data

3.2.4.1 Node stresses

In order to analyze the stress distribution in a sample, a stress tensor $\boldsymbol{\sigma}^i$ is calculated for each node i of the lattice system (Topin *et al.* [61], Moreau [45]). The space is tessellated into hexagonal elementary cells whose sides are bisectors of the lattice bonds connecting the nodes (Fig. 3.7). For the node i, the stress component $\sigma_{\alpha\beta}^i$ is determined as the tensorial moment $M_{\alpha\beta}^i$ divided by the surface S_i affected to the node i:

$$\sigma_{\alpha\beta}^i = \frac{1}{S_i} M_{\alpha\beta}^i = \frac{1}{S_i} \sum_j r_\alpha^{ij} f_\beta^{ij} \tag{3.28}$$

where the sum is made over all neighboring nodes j and
- S_i is the surface of the elementary cell corresponding to node i
- r_α^{ij} is the α component of the position of the midpoint of the bond ij
- f_β^{ij} is the β component of the force in the bond ij (action of j over i)

In the stress maps, each component of $\sigma_{\alpha\beta}^i$ is represented by a proportional color assigned to the node i. These colors are linearly interpolated over the rest of the space.

The macroscopic stress $\sigma_{\alpha\beta}$ is calculated as a sum of tensorial moments over all nodes divided by the total surface S of the domain:

$$\sigma_{\alpha\beta} = \frac{1}{S} \sum_j M_{\alpha\beta}^i \tag{3.29}$$

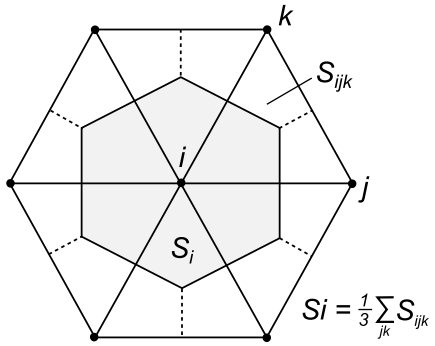

Figure 3.7: Elementary cell used to calculate node stresses

3.2.4.2 Volume changes

For the purpose of representing graphically local deformations in a sample, a logarithmic volumetric strain δ^i is calculated for each elementary cell corresponding to node i:

$$\delta^i = ln\left(\frac{S_i}{S_i^0}\right) \tag{3.30}$$

where S_i^0 and S_i are respectively the initial and the current surface of the elementary cell i.

3.2.5 Response of the model to biaxial loading

A peculiarity of the model used in this study lies in its simple nature. Simple constitutive law used at the microscopic level is combined with the mesoscopic description of concrete material, so that complex phenomena can be reproduced. The material is represented as a triangular lattice of bonds described with different material parameters, depending on the phase (mortar, aggregate, interface). In this section, some aspects of the model's application to biaxial compression loading are presented. However, performed simulations will reveal strong geometric concerns of the model under such loading type (3.2.5.3). Hence, at the end of the chapter, an alternative strategy will be proposed.

3.2.5.1 Influence of confining pressure

The influence of confining pressure on model's behavior was studied on concrete sample described in Section 3.2.1. Four biaxial tests were performed at different confining pressures: 50 MPa, 100 MPa, 200 MPa and 650 MPa. The levels of stiffness were chosen by setting κ in accordance with the real concrete as explained in Section 3.2.3. The force thresholds were calibrated at 50 MPa and kept the same for all confining pressures.

Figure 3.8(a) shows corresponding macroscopic curves. Below (Fig. 3.8(b)), experimental results of triaxial tests performed on reference concrete at the same confining pressures are presented. Figure 3.9 compares more precisely numerical and experimental tests performed at 50 MPa and 200 MPa of confinement.

Bearing in mind the very simple nature of the model, the emphasis is not on the exact reproduction of experimental results but on capturing the basic phenomena that occur in concrete under confined compression. Therefore, numerical results are in a good agreement experimental observations concerning evolution of concrete behavior as a function of the confinement. The ratio q/p_c decreases as the confining pressure increases (as for soils). Moreover, both numerically and experimentally, the peak stress is observed at low confinement while the stress-strain curves have a form of plateau under high pressure.

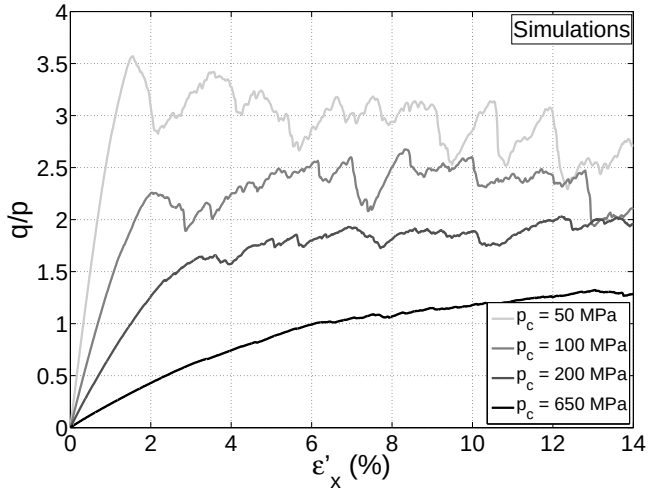

(a)

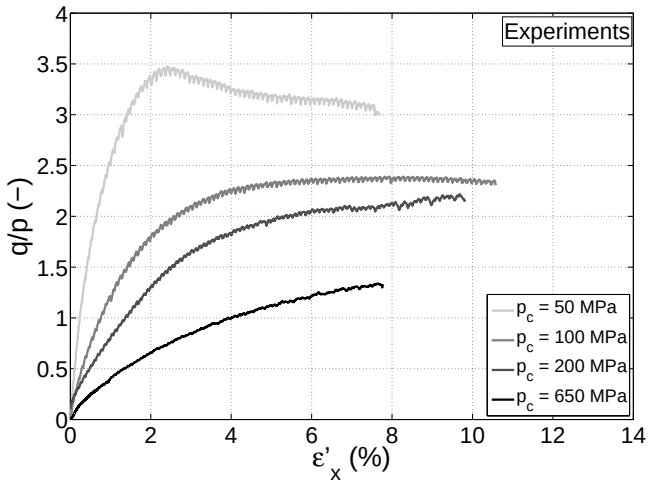

(b)

Figure 3.8: Biaxial and triaxial compression tests conducted at different confining pressures on (a) numerical specimen and (b) experimental specimen respectively: stress deviator q to confining pressure p_c ratio vs. axial strain ε'_x

Figure 3.9 indicates that numerical sample undergoes very high lateral strains under biaxial loading what may be a combined effect of the mesh fabric and 2D nature of the model.

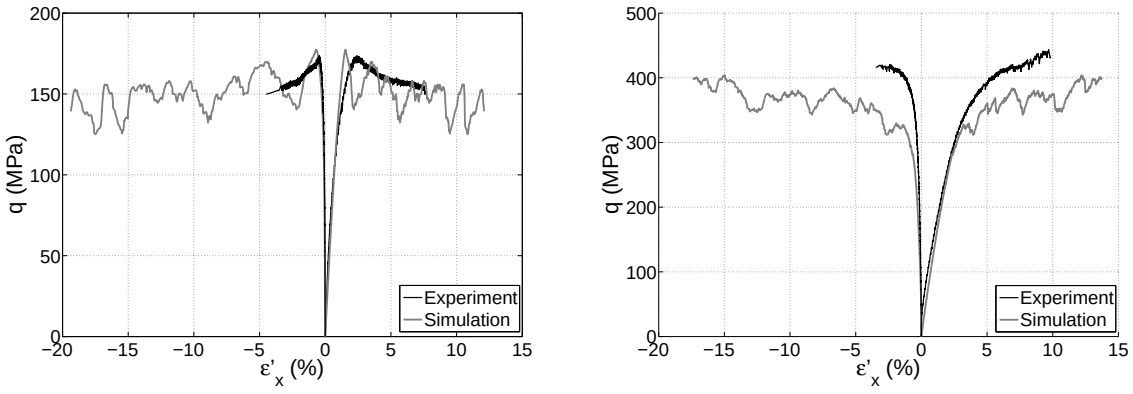

Figure 3.9: Biaxial and triaxial compression tests conducted on numerical and experimental specimens respectively: stress deviator q vs. axial strain ε'_x
(a) $p_c = 50$ MPa
(b) $p_c = 200$ MPa

Let us now analyze the distribution of local stresses and volume changes in a sample tested at 50 MPa of confining pressure. Figure 3.10(a) represents a map of vertical stress distribution at the end of the isotropic loading. This plot clearly indicates an inhomogeneous stress state due to the presence of aggregates which are stiffer than matrix and thus concentrate higher stresses. The large stresses are also located in a matrix phase, between the aggregate particles and around the pores.

The local volume changes presented in Figure 3.11(a)) indicate smaller volumetric deformations within aggregate particles. Matrix is more compressible but its deformations are less uniform.

Similar maps but corresponding to the peak stress situations are also plotted. We can see in Figure 3.10(b) that the large stresses pass through the aggregates across the specimen, forming well-defined chains. Figure 3.11(b) in turns, reveals localization of several shear zones with high dilation in a sample.

The mesh form and size has probably strong influence on the creation of these localization zones, since the similar patterns were observed in samples submitted to higher confining pressures. On the contrary, in the experiments, few cracks perpendicular to the main loading direction are observed in concrete samples tested at high confinement; however, these cracks opens during the unloading and in fact, no information about the specimen's state at the peak stress is available experimentally. These vertical "compressive cracks" are not observed in the simulations after the unloading. This may be due to the fact that these kind of cracks results from very high reduction in the local volumes, which is not accounted in the model. Indeed, the high confining pressure is only reflected by the small κ. To include this feature, irreversible compressive strains could be introduced in force-displacement relation.

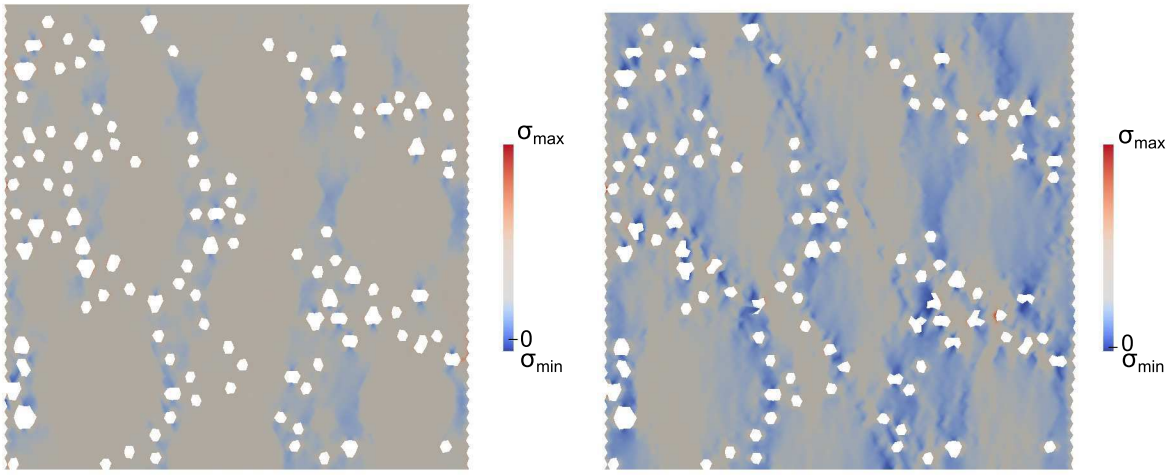

(a) (b)

Figure 3.10: Map of the vertical stresses in biaxial compression at 50 MPa of confinement
(a) Local stress state at the end of isotropic compression up to 50 MPa
(a) Local stress state at the macroscopic peak stress

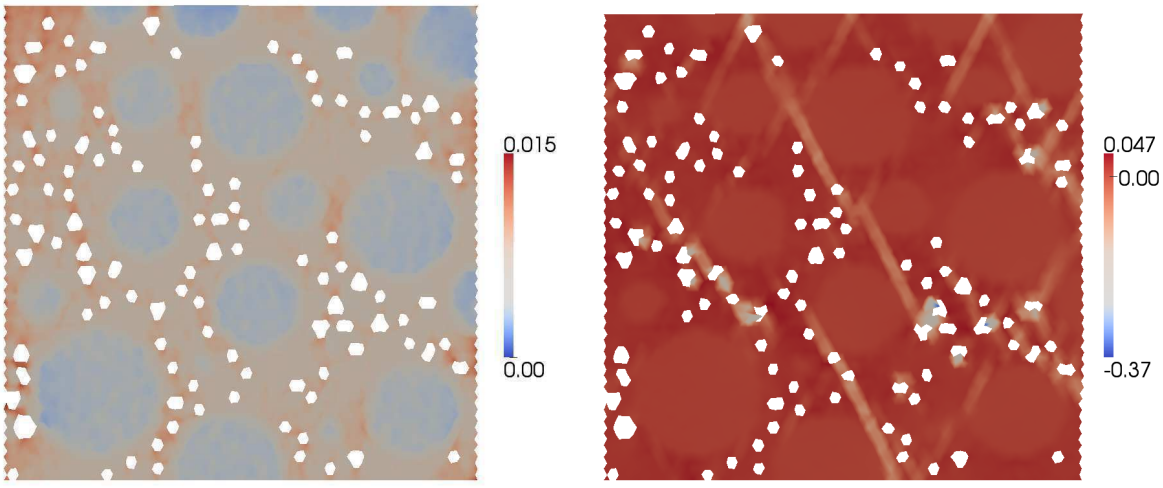

(a) (b)

Figure 3.11: Map of the local volume changes in biaxial compression at 50 MPa of confinement: positive values correspond to contraction
(a) Local deformations at the end of isotropic compression up to 50 MPa
(a) Local deformations at the macroscopic peak stress

3.2.5.2 Influence of voids

Geometrical disorder in a numerical sample is introduced by adding voids in a matrix phase, which means removing a certain number of bonds. A study was performed to show the influence of the void volume fraction on the model's behavior. Simulations were performed on homogeneous sample, representing only mortar phase. Porosity ϕ is defined as a ratio of number of bonds removed from the specimen n_v to the initial number of bonds n_0:

$$\phi = \frac{n_v}{n_0} \tag{3.31}$$

Confined compression tests were performed on 4 samples characterized by different porosities: $\phi = 0.00$, 0.03, 0.06, 0.12. The corresponding numbers of initial bonds are: 19240, 18631, 18041, 16965. Figure 3.12 illustrates two of the tested samples: $\phi = 0$ and $\phi = 0.12$ at the initial state. Deviatoric stress-strain curves are presented in Figure 3.13. Decrease of maximum deviatoric stress and transition from a peak stress to a common plateau as the porosity increases is observed. The analogy to behaviors of dense and loose sands is thus obtained.

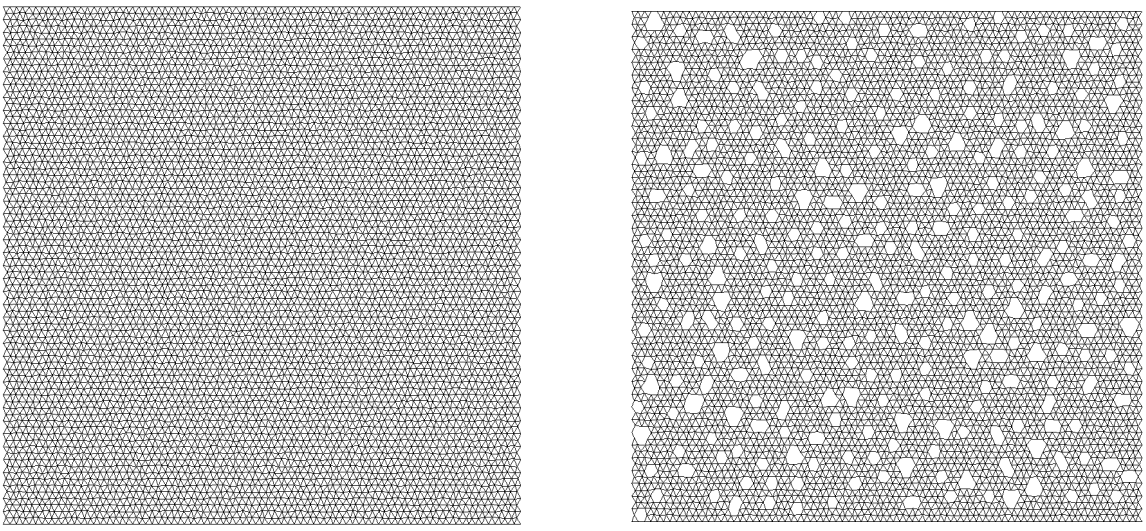

(a) (b)

Figure 3.12: Numerical samples representing homogeneous material with different void ratios ϕ; (a) $\phi = 0$, (b) $\phi = 0.12$

It is interesting to analyze the evolution of damage in tested samples. Damage is defined as a loss of cohesion and in order to quantify it, a damage parameters D is introduced. D expresses a percentage of broken cohesive links in a sample, as follows:

$$D = \frac{n_{broken}}{n_0(1-\phi)} \tag{3.32}$$

where n_{broken} is a number of broken cohesive links.

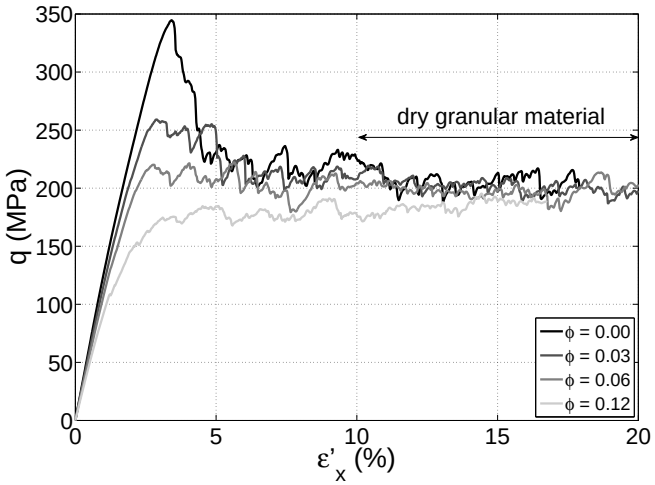

Figure 3.13: Biaxial compression conducted at 50 MPa of confinement on samples with different void ratios: stress deviator q vs. axial strain ε'_x

The evolution of damage parameter with the axial strain for samples with $\phi = 0$, $\phi = 0.06$ and $\phi = 0.12$ is presented in Figure 3.14. In the nonporous sample, damage appears later than in porous samples. However, its growth is faster and the maximum value of D is reached at lower deformation than for other samples. In porous samples the increase of damage seems to be more gradual.

Depending on the distance of the connected nodes, broken links become either inactive which means transfer no forces, or work as usual contacts with friction. During the simulation, new frictional contacts, not existing before as cohesive links, can also appear. This feature, together with representing voids in a numerical sample, was introduced as an attempt to simulate the compaction process without using complex behavior laws at the microscopic level. Compaction is a typical phenomenon for cement matrix materials under high hydrostatic loading and is characterized by a stiffness reduction due to porosity closure followed by subsequent stiffening due to material densification.

Figure 3.15 displays the response of two numerical samples: nonporous and porous, under isotropic loading. Strongly nonlinear macroscopic behavior is obtained in the porous sample despite of using a very simple behavior law at the contact level. The nonlinearity comes from geometrical rearrangements in the sample, due to the presence of voids, and the creation of new contacts. The lattice model is however not able to sustain high confining pressures and has other drawbacks that will be listed afterwards; another approach overcoming these difficulties will be proposed. Therefore, a more exhaustive study on the influence of void features will be performed with this second approach and presented in Chapter 4.

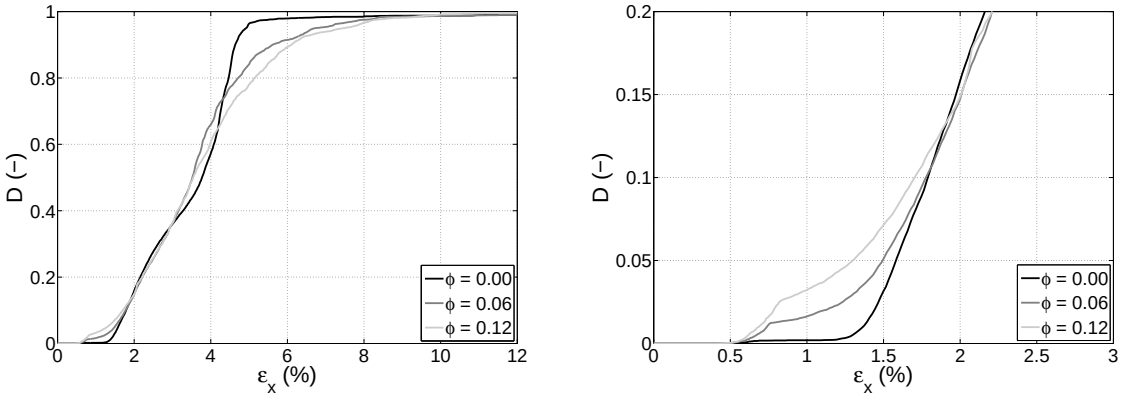

Figure 3.14: (a) Evolution of damage parameter during biaxial compression conducted at 50 MPa of confinement on samples with different void ratios
(b) Zoom on the initial part of the curves

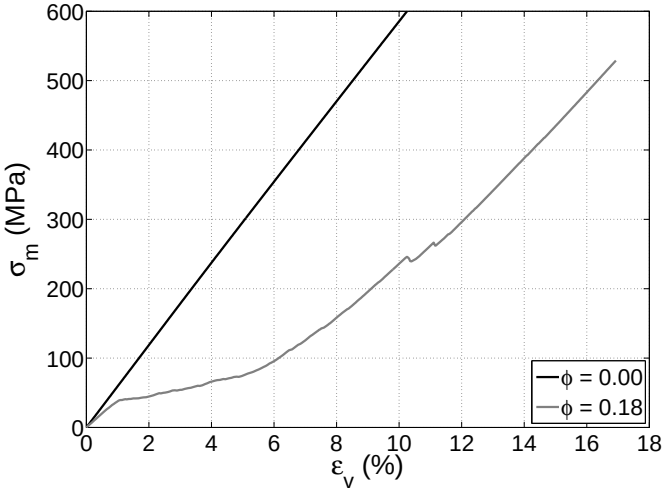

Figure 3.15: Isotropic compression conducted on two samples with different void ratios: mean stress σ_m vs. volumetric strain ε_v

3.2.5.3 Limitations of the model

This section intends to describe problems which appeared while employing the model in confined compression tests. Most of them are linked to the mesh fabric. Mesh generation procedure provides a mesh that is strongly anisotropic. Even with high perturbation of node positions (see Section 3.2.1), during an isotropic compression, vertical and lateral strains are considerably different. Figure 3.16 presents distributions of bonds orientations for different values of perturbation coefficient α. It can be seen that an increase in α makes the mesh more isotropic. On the other hand, the use of a high α value to preserve isotropy results in very big differences in bonds lengths. This in turn creates technical problems in contact detection algorithm and in postprocessing.

The contact detection in a lattice type model appeared problematic itself. In this kind of model, medium is represented by means of material points connected by bonds (line-elements), which is somewhat different than representing the material by interacting disks. Detection of frictional contact between two nodes previously linked by a cohesive bond is simply based on their initial distance, whereas detection of new contacts is not so obvious. In classical DEM, contact detection is based on the distance in-between disks. In our model, since no radius are attributed to the nodes, a single distance value (d_{cut}) is used to detect new contacts. This apparent simplification has in fact probably important consequences on the behavior of the sample, making it more geometrically inconsistent as the deformation increases.

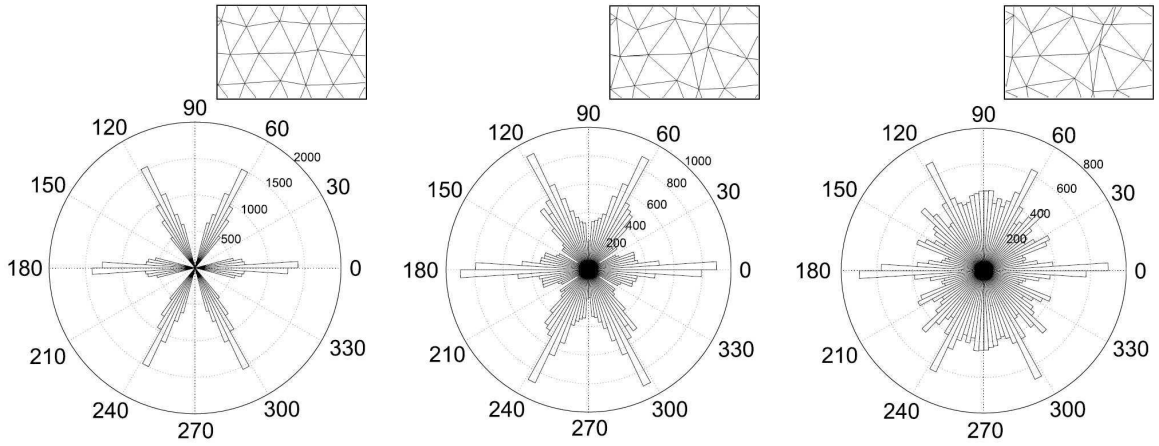

(b) (c)

Figure 3.16: Distribution of contact orientations in a triangular lattice for different perturbation coefficients (fragments of corresponding lattices are shown in rectangles): (a) $\alpha = 0.25$, (b) $\alpha = 0.50$, (c) $\alpha = 0.75$

Above mentioned geometrical problems appeared to be very difficult to solve in the proposed model. After some unsuccessful trials, the decision was made to form the lattice from granular assembly, by connecting disk centers, instead of triangular grid of nodes. Generation of a homogeneous and isotropic granular assembly is based on methods proposed by Combe and Roux in [13]. The method consists in isotropic compression of a grain collection enclosed in rigid walls. Initially, the system is made of polydisperse disks

(according to a homogeneous distribution of volumes) whose centers are placed on the regular triangular lattice. Disks do not touch each other. Such sample is confined without friction, until the equilibrium configuration is reached (resultant force for each node is lower than a small value compared to the mean force with the intended pressure on the walls. Compression is performed with stress control.

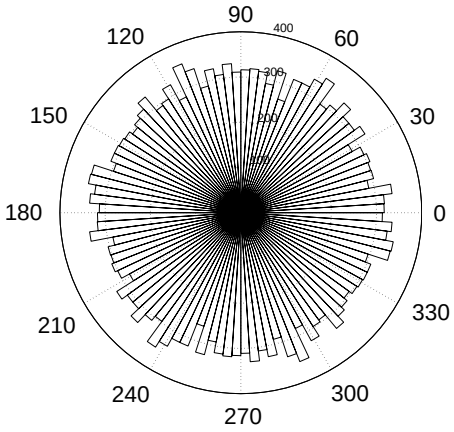

Figure 3.17: Contacts orientations in a granular assembly

Figure 3.17 shows contact distribution in a sample prepared with described procedure, which proves sample isotropy. Moreover, the use of disks provides specific geometrical constraints and results in an isotropic specimen for which the geometric consistency will be maintained during the deformation.

Figure 3.18 displays a comparison of biaxial tests performed at 50 MPa of confinement on two samples prepared with the two introduced methods. The two specimens consist of approximately the same number of bonds. It can be observed that using the same material parameters results in different macroscopic behaviors, except for large strains, where microscopic friction coefficient μ controls the mechanical response. The elastic behavior of sample constructed on triangular grid of nodes (s1) is stiffer than that of granular assembly (s2). A peak stress with a greater value of the maximum stress is reached in sample s1. Macroscopic Young's modulus depends on the normal interaction stiffness. In our model, the latter does not account for discrete element sizes and packing configuration. These both features are somewhat different for the two samples, s1 and s2, hence differences in macroscopic stiffness. The absence of peak stress in the second sample (s2) is explained by its lower density. The use of disks assembly provides an "initial" porosity induced by geometrical constraints, which is not the case with triangular grid (see Fig. 3.19).

In the next chapter, "granular" sample will be used. Due to its initial porosity, the fraction of void phase will be reduced compared to the void fraction in the triangular lattice.

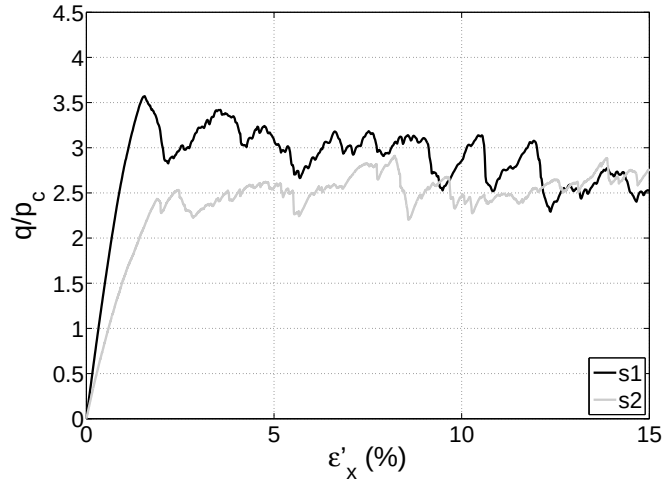

Figure 3.18: Biaxial compression test conducted at 50 MPa of confinement on the sample built from triangular grid of nodes (s1) and from disks assembly (s2): stress deviator q vs. axial strain ε'_x

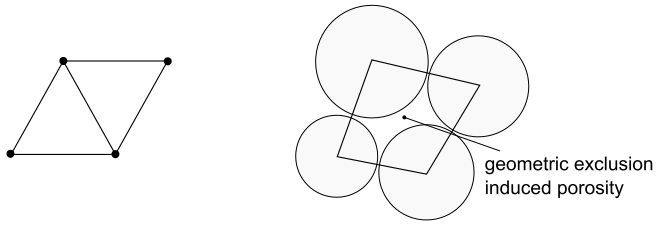

(a) (b)

Figure 3.19: Schematic illustration of the "initial" porosity
(a) triangular lattice of bonds
(b) lattice of bonds formed on granular assembly

3.3 Chapter conclusion

A 2D mesoscopic model of concrete was developed within the framework of the discrete element method. The model was intended to combine simple interaction law with material heterogeneity at the mesoscopic level. Therefore, two types of interactions are recognized in the model: cohesive links, whose behavior is described by a linear elastic-brittle law, and frictional contacts detected during the simulation, with Coulomb's friction law. The latter are either broken cohesive links, or new contacts. On the other hand, three phases described with different mechanical parameters are present in a concrete sample: matrix, aggregate and interface. In addition, a sample's mesostructure is modified by introducing voids in a matrix phase.

After first calibration efforts, the model was used to simulate the biaxial behavior of concrete at different levels of confinement. Two important results were obtained with this simple approach:

- the increase of concrete strength and transition from peak stress to stress plateau as the confining pressure increases
- strongly nonlinear behavior under isotropic compression induced by the presence of voids.

These and other aspects of numerical concrete sample behavior will be examined in closer details in the following chapter.

Chapter 4

Numerical study: influence of concrete mesostructure

The first part of this chapter will focus on the influence of void configuration on macroscopic behavior of a single phase numerical specimen. In the second part, we will come back to the primary goal of this thesis, which is the influence of coarse aggregate on concrete behavior. The effect of aggregate (a) and interface (am) mechanical properties on both macroscopic response and damage mechanisms, will be investigated. The effect of aggregate shape will not be concerned by this study. Since the model is in its early development stage and new objectives always bring new ideas and difficulties, this section provides, rather than final results, a discussion on the model in the scope of coarse aggregate effects.

4.1 Influence of void morphology

One of the model's peculiarities is the consideration of voids as a mesostructural entity. Their introduction was proved to satisfactorily model the compaction of concrete despite using linear constitutive laws at the bond level. Due to calculation time and thus mesh size constraints, it is not possible to introduce small scale porosity (so called microporosity that size is well below the bond length) which makes up an important part of the concrete porosity. The porosity introduced in the model thus corresponds to the macroporosity in a concrete sample; however, as it has been shown in the previous chapter, the stress strain curve obtained with porous numerical sample under isotropic loading has a characteristic S-shape as that of real concrete under hydrostatic compression. In this section, we examine more precisely how the properties of voids influence the response of a numerical sample. A sensitivity study is done to evaluate the effect of the two following parameters:

- void volume ratio ϕ - expressed as the number of bonds removed from the sample divided by the initial number of bonds,

- void size d^* - expressed as the ratio of mean void diameter $< d_{void} >$ to mean diameter of discrete particles in a sample d_{mean}.

A normal distribution of voids sizes is used with a mean value equal to $< d_{void} >$ and a standard deviation equal to $0.5d_{mean}$, what means that the variation of void size in a sample is very small.

In this primary study, numerical samples consist of only one material phase - mortar, with different void volume fractions and different void sizes. The variations of ϕ and d^* in performed simulations are presented graphically in Figure 4.1. The algorithm to place voids in a sample assumes their circular shape; moreover, the percentage of voids, which is an input parameter in the procedure, is calculated using the area of circles, not the number of bonds. It is thus not possible to fully control ϕ while changing the void features. Figure 4.1 indicates that the precision of the algorithm used to build the sample increases as voids become larger. This is in fact obvious if we consider that ϕ is a "Monte Carlo estimation" of the void volume fraction. The procedure could be certainly adjusted for the future studies.

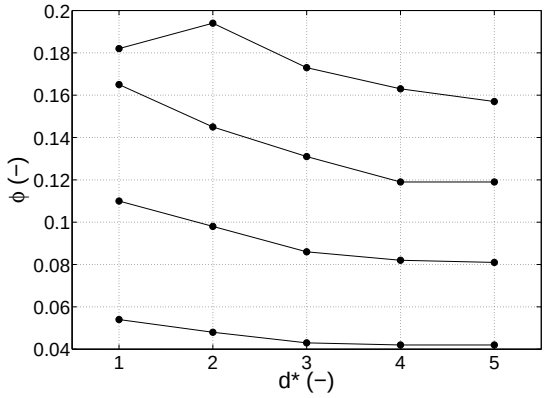

Figure 4.1: Different sets of void parameters used in the study placed in the $\phi - d$ space

Figure 17 shows the evolution of initial volumetric stiffness as a function of ϕ and d^*. The initial modulus of each tested sample is compared to the initial modulus of nonporous sample. It can be observed that the elastic stiffness is strongly affected by the volume of voids in a sample: the stiffness drops as the porosity increases. This observation is in agreement with experiments performed by Vu *et al.* [66] on concretes with different water/cement ratios, and thus different porosities (see Fig. 1.21(a)). On the other hand, the void size has only a slight effect on the initial volumetric stiffness: the lower the size of voids is, the higher is the specimen's stiffness.

The effect of void ratio for one void size ($d^* = 3$) is more precisely illustrated in Figure 18 representing mean stress σ_m as a function of volumetric strain ε_v. The increase in porosity induces higher volumetric strains. In the nonporous sample, a monotonous, quasi-linear raise of tangent bulk modulus is observed. This stiffening is due to newly created contacts as the loading proceeds. At the end of the test, the number of interactions in a sample has increased of about 15%. When voids are introduced in a sample, a volumetric stiffness reduction is first observed. It is followed by an increase of the tangent modulus. The stiffness reduction originated from the presence of voids is controlled by their properties. It is interesting to note that this feature results directly from the meso-scale structuring of voids. No parameter has been used to "control" the macroscopic curve,

except the way voids are spread within the mortar phase. This is an asset of the model: macroscopic features arise from the meso-scale geometry and basic mechanical properties. Results presented in Figure 19 indicates that the curvature of the stress-strain curve at low mean stress level is more affected by the size of voids than the void volume fraction. The volumetric stiffness reduction is more marked for samples with big pores ($d^* = 3$ and $d^* = 5$) than for sample with small pores ($d^* = 1$), despite smaller void volume fraction.

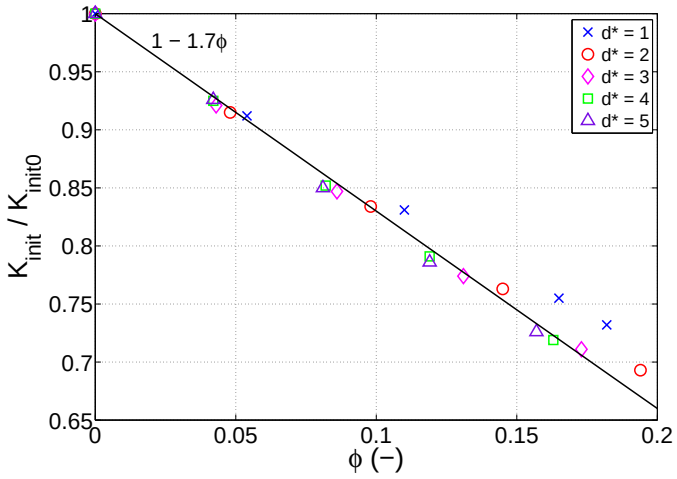

Figure 4.2: Initial bulk modulus K_{init} to the initial bulk modulus of nonporous sample K_{init0} ratio as a function of void ratio ϕ, for different void sizes d^*

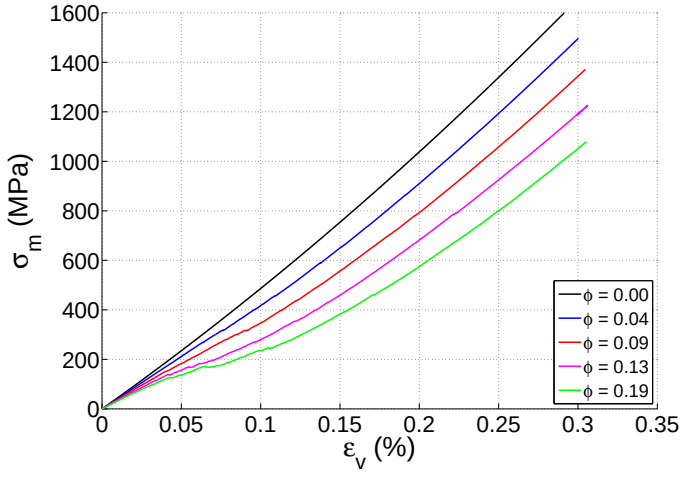

Figure 4.3: Isotropic compression conducted on samples with different void ratios ϕ and with a void size d^* equal to 3: mean stress σ_m vs. volumetric strain ε_v

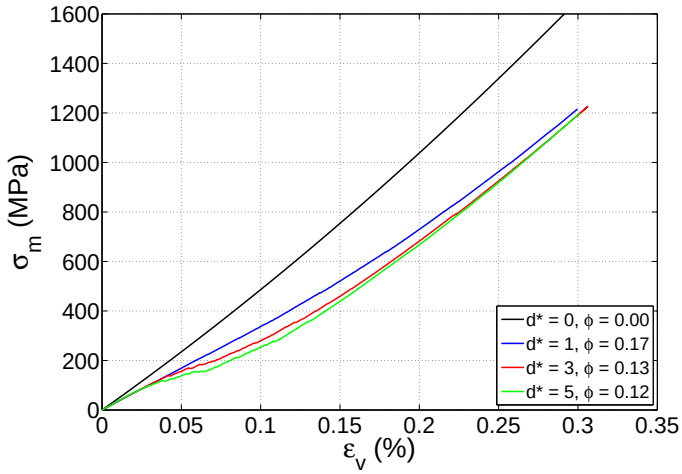

Figure 4.4: Isotropic compression conducted on samples with different void ratios ϕ and different void sizes d^*: mean stress σ_m vs. volumetric strain ε_v

In order to describe the curvature of the stress-strain curve, S is defined as the ratio of the maximum to the minimum tangent modulus (see Fig. 20):

$$S = \frac{K_{max}}{K_{min}} \tag{4.1}$$

For the range of parameters in the current study, S is greater than 1 and increases for more pronounced curvatures. Figure 21 displays a color map representing the value of S as a function of void ratio ϕ and void size d^*, interpolated from 20 performed tests. Black corresponds to the minimum value obtained for the nonporous sample. It can be observed again that both void volume fraction and void size influence the curvature of hydrostatic curve; the function $S(\phi, d^*)$ declines quasi-linearly. It is interesting to note, that for high void ratios, the presence of small pores does not affect considerably the shape of stress-strain curve. On the other hand, big voids seem to strongly reduce the volumetric stiffness even at lower void ratios.

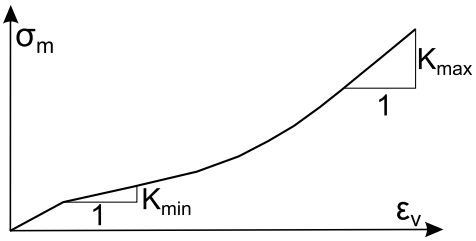

Figure 4.5: Sketch showing the tangent moduli K_min and K_max used in the definition of the curvature parameter S

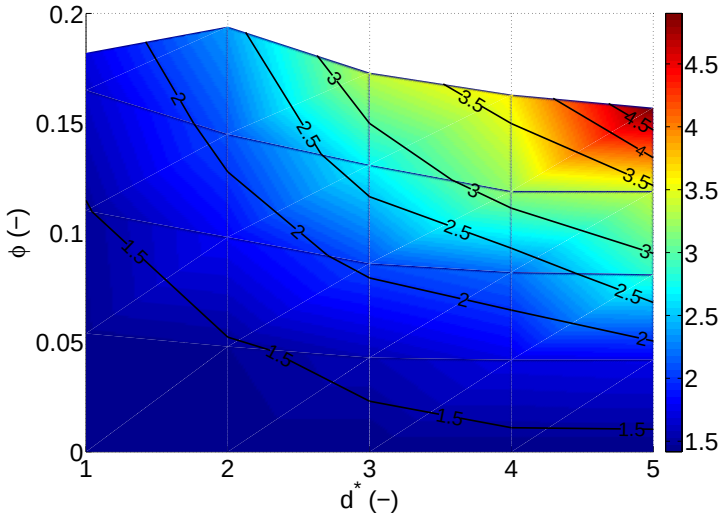

Figure 4.6: Color map representing the evolution of curvature parameter S as a function of void ratio ϕ and void size d^*

4.2 Influence of aggregate and interface properties

The influence of mechanical parameters corresponding to aggregate phase and aggregate/mortar interface is investigated on a numerical sample consisted of 6784 particles connected by 16643 line elements. Spherical aggregates are randomly distributed over the specimen (as described in section 3.2.1). Percentage of bonds representing mortar, aggregate and interface is listed in table 2.

Type of elements	**Percentage**
Mortar	55%
Aggregate	38%
Interface	7%

Table 4.1: Percentage of different type line elements in a concrete sample

Thanks to a simple nature of the model, the number of parameters describing mechanical behavior of material phases is very limited. Each phase is characterized by stiffness parameters k_n and k_t, cohesive thresholds F_n^0 and F_t^0, describing cohesive links, and a friction coefficient μ, used for contacts.

In all the tests presented in this section, the stiffness parameters are the same as in previous chapter; their relative values are recalled below:

$$\frac{k_n^a}{k_n^m} = \frac{k_t^a}{k_t^m} = 3 \tag{4.2}$$

$$\frac{k_n^{am}}{k_n^m} = \frac{k_t^{am}}{k_t^m} = 1 \tag{4.3}$$

Regarding cohesive threshold, we define a reference sample as following:

$$\frac{F_n^{0a}}{F_n^{0m}} = \frac{F_t^{0a}}{F_t^{0m}} = 3 \tag{4.4}$$

$$\frac{F_n^{0am}}{F_n^{0m}} = \frac{F_t^{0am}}{F_t^{0m}} = 0.2 \tag{4.5}$$

The value of aggregate cohesive threshold to mortar threshold ratio was reduced from 10, used in the previous chapter, to 3, which seems to be more adequate to simulate ordinary concrete.

Although it is very difficult to deduce microscopic model's parameters from experiments performed on concrete or on concrete constituents, available experimental data may be used as an indicator to characterize the model. Table 3 lists uniaxial strength properties of the reference concrete, mortar and coarse aggregate obtained from experiments. Tensile strength of mortar was estimated from 3-point bending tests, that of aggregate - from tensile splitting test, and that of concrete was measured from direct tensile test.

Material	**Mortar**	**Siliceous aggregate**	**Concrete**
σ_c [MPa]	60	330	42
σ_t [MPa]	9	23	3.6

Table 4.2: Uniaxial strength properties of concrete and its mesoscopic constituents (collected from [29, 22, 48])

The interfacial transition zone (ITZ) between cement paste and aggregate (cement matrix and large aggregates at the mesoscopic scale), is well known as a weak link in concrete. In the reference sample, its strength was arbitrarily set to 20 % of the mortar strength. Besides, in all the phases, the normal and tangential breaking forces are equal, which is a simplification adopted in the first attempt.

The first objective of this preliminary study is to analyze the behavior of the model depending on aggregate and interface properties and capture the main tendencies. A direct comparison with experiments, would be a much more challenging task, especially because in the experiments, it is not possible to control different aggregate and interface properties separately.

4.2.1 Effect of aggregate and interface strength at very low confinement

In this section, we examine the effect of aggregate and interface cohesive thresholds on concrete behavior. These parameters correspond to the strength of aggregate and interface at the macroscopic scale.

We are first interested in the behavior of the numerical sample under 1 MPa of confining pressure. The confinement was applied due to technical reasons, but its very low value allows comparing, in a qualitative manner, numerical results with observations from simple compression tests performed on concrete.

The response of the reference sample is presented in Figure 4.22(a). This figure also shows a comparison of stress-strain curves for matrix, aggregate and concrete. Quasi-linear elastic behavior followed by a sudden failure is observed for homogeneous samples of matrix and aggregate. In a concrete composite sample, a stiffness reduction before the peak stress is found despite of the elastic-brittle nature of the model. This phenomenon is thus due to the material heterogeneity and as in a real concrete specimen, comes from multiple microcracking predominantly in the ITZ. Figure 4.22(b) shows the evolution of broken links in the reference concrete sample, in its three phases: matrix, aggregate and interface. Damage appears first at the aggregate/mortar interface and continues to develop in the mortar, between the aggregates. Aggregate do not break as the axial displacement increases. At some point, the sample undergoes a brittle failure characterized by several quasi-vertical cracks around the aggregates. Figure 23 shows the sample at the end of the test. Green dots mark broken cohesive links. This failure pattern, characterized by aggregate debonding, is typical for ordinary concrete, made with aggregates considerably stronger than mortar, tested under uniaxial compression.

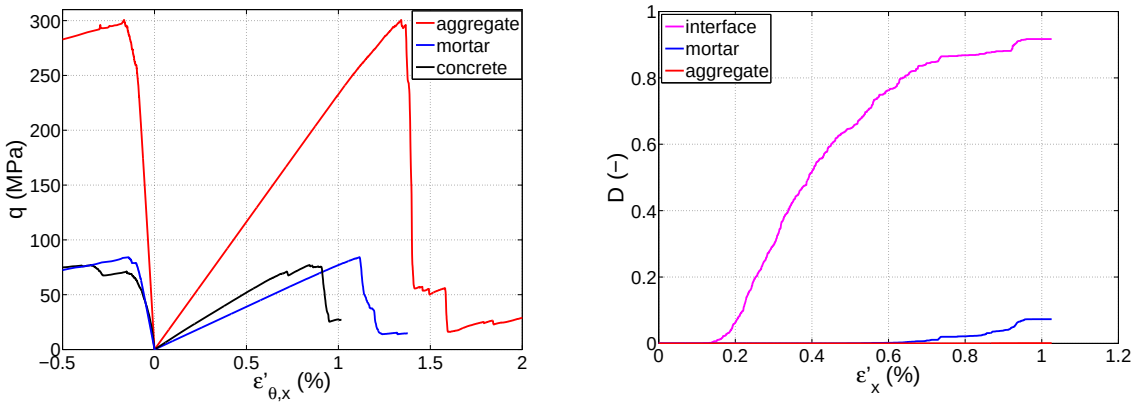

(a) (b)

Figure 4.7: Biaxial compression at 1 MPa of confinement
(a) behavior of the reference concrete sample ($F^{0a}/F^{0m} = 3$, $F^{0am}/F^{0m} = 0.2$), mortar sample and aggregate sample: stress deviator q vs. strain components ε'_θ and ε'_x
(b) evolution of damage parameter D vs. axial strain ε'_x in the reference concrete sample

Several tests were performed using different breaking properties for aggregate F^{0a} and interface F^{0am} phases. In order to analyze the influence of this two parameters separately, the following tests are detailed:

- S1: $\frac{F^{0a}}{F^{0m}} = 3$, $\frac{F^{0am}}{F^{0m}} = 0.2$ (reference sample)
- S2: $\frac{F^{0a}}{F^{0m}} = \mathbf{9}$, $\frac{F^{0am}}{F^{0m}} = 0.2$
- S3: $\frac{F^{0a}}{F^{0m}} = \mathbf{1}$, $\frac{F^{0am}}{F^{0m}} = 0.2$

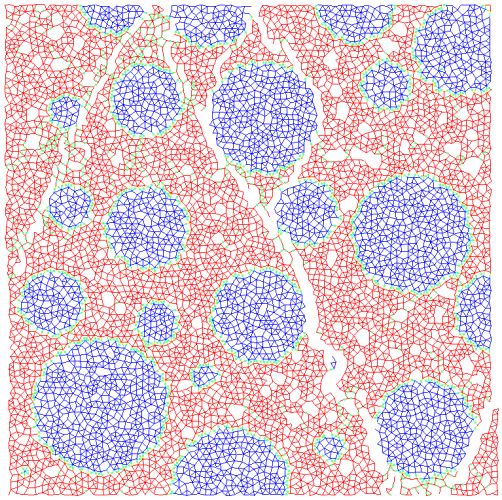

Figure 4.8: Crack pattern at 1 MPa of confinement in the reference concrete sample: $F^{0a}/F^{0m} = 3$, $F^{0am}/F^{0m} = 0.2$

- S4: $\frac{F^{0a}}{F^{0m}} = 3$, $\frac{F^{0am}}{F^{0m}} = \mathbf{1}$
- S5: $\frac{F^{0a}}{F^{0m}} = 3$, $\frac{F^{0am}}{F^{0m}} = \mathbf{0.05}$

Figure 24 displays stress-strain curves obtained for these five numerical samples. Left graph, indicates the maximum stress differences due to different cohesive thresholds in aggregate phase, right - due to different cohesive thresholds in the interface. Both these parameters influence the maximum stress value; however, within the studied range, the differences in concrete strength compared to the reference sample are generally quite limited (up to 20%).

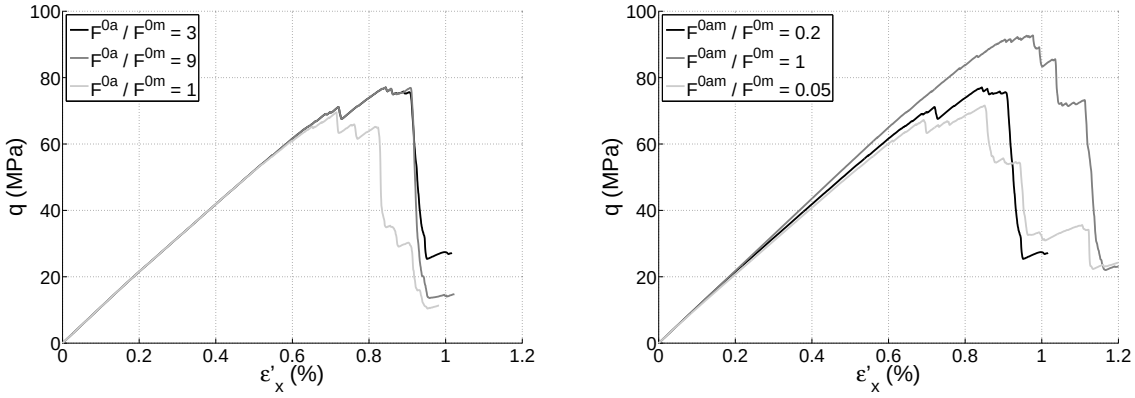

(a) (b)

Figure 4.9: Influence of (a) aggregate and (b) interface strength on concrete behavior at 1 MPa of confinement: stress deviator q vs. strain components ε'_θ and ε'_x

Since no aggregates are broken in the reference sample, raise in aggregate cohesive threshold in the sample S2 does not influence the results. In contrast, high breaking force attributed to interface in the sample S4 increases remarkably the specimen strength. Macroscopic cracks encircle large aggregates but also tend to pass in the matrix between the aggregates (see Fig. 25).

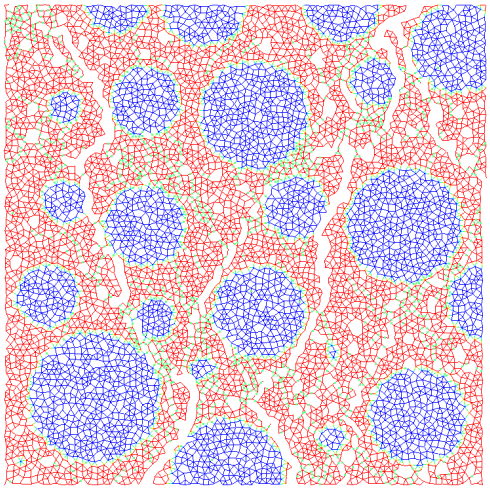

Figure 4.10: Crack pattern at 1 MPa of confinement in sample with high interface strength: $F^{0am}/F^{0m} = 1$

Weakening aggregates, as well as interface reduces the maximum stress. Damage evolution in the sample with a reduced aggregate cohesive threshold (S3) is presented in figure 26. Indeed, a part of links corresponding to aggregate is broken but damage is still mainly concentrated on the interface.

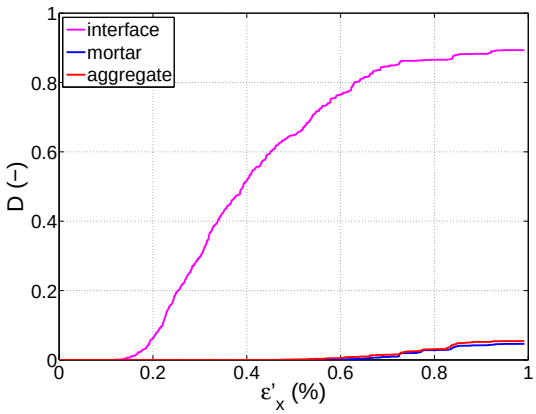

Figure 4.11: Evolution of damage parameter D with axial strain ε'_x at 1 MPa of confinement, for sample with low aggregate strength: $F^{0a}/F^{0m} = 1$

Let us now summarize more results of tests performed under very low confinement. Some values were studied despite being not realistic for concrete. Figure 27 displays a grey

level map representing the strength of numerical specimens, depending on both aggregate and interface cohesive thresholds. Grey level intensity is proportional to the peak stress; white corresponds to the highest maximum stress. Strong dependence of concrete strength on the interface strength is observed. Aggregate strength affects the concrete strength provided relatively low aggregate to mortar strength ratio. For high F^{0a}/F^{0m} ratios, further increase of aggregate strength does not affect the maximum deviatoric stress. These different combinations of aggregate and interface strength to mortar strength ratios results in various failure patterns. Six different modes of failure, illustrated schematically in Figure 28, were observed.

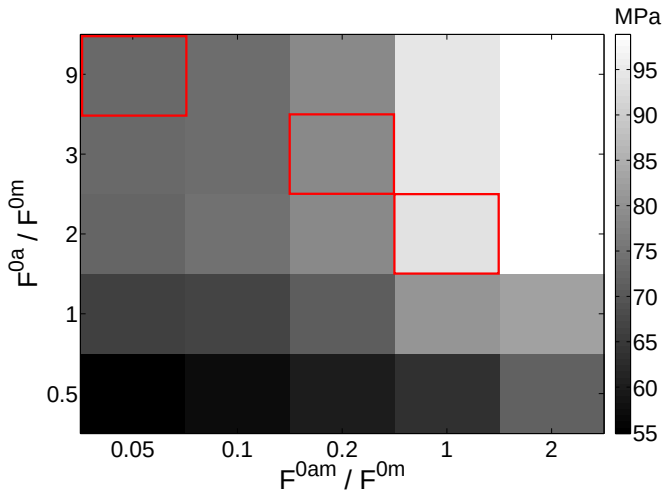

Figure 4.12: Grey level map representing the maximum deviatoric stress at 1 MPa of confinement, as a function of different aggregate and interface properties

In connection with experiments, the attention is focused on three parameters sets (related maximum stress values are marked with red squares in Figure 27):

- $\frac{F^{0a}}{F^{0m}} = 3$, $\frac{F^{0am}}{F^{0m}} = 0.2$ (ref. sample) - which may be referred to as strong aggregate and normal interface,
- $\frac{F^{0a}}{F^{0m}} = 9$, $\frac{F^{0am}}{F^{0m}} = 0.05$ - referred to as very strong aggregate and weak interface,
- $\frac{F^{0a}}{F^{0m}} = 2$, $\frac{F^{0am}}{F^{0m}} = 1$ - referred to as weak aggregate and strong interface.

These three sets of parameters would correspond in our experimental study to siliceous aggregate concrete, glass ball concrete and limestone aggregate concrete respectively. The evolution of maximum stress for these three samples is consistent with experimental results: the highest strength in simple compression was found for limestone aggregate concrete, the lowest - for glass ball concrete. Failure patterns obtained experimentally are also reproduced by the model. As mentioned above for the reference sample, when aggregates strength is much higher but interface strength considerably lower than that of mortar, cracks circumscribe the aggregates. This was the case of siliceous aggregate concrete but also glass ball concrete. In sample with weak aggregate ($F^{0a}/F^{0m} = 2$) and

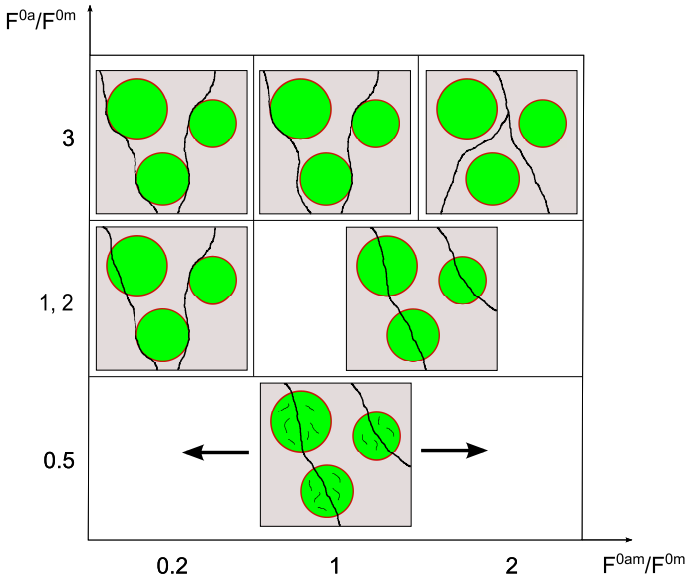

Figure 4.13: Sketches of failure patterns at 1 MPa of confinement in numerical samples with different aggregate and interface properties

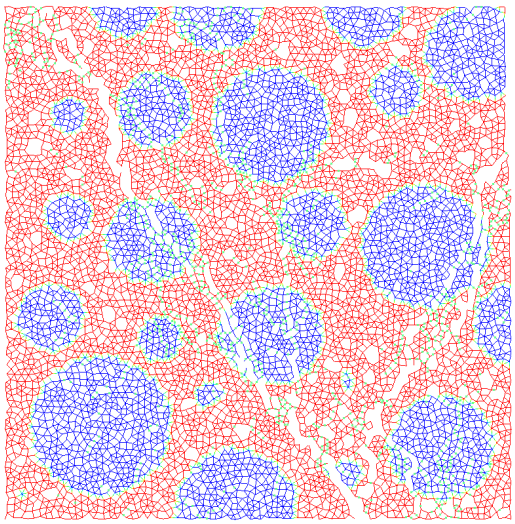

Figure 4.14: Crack patterns at 1 MPa of confinement in sample with low aggregate strength: $F^{0a}/F^{0m} = 2$, and high interface strength: $F^{0am}/F^{0m} = 1$,

strong interface ($F^{0a0}/F^{0m} = 1$), cracks pass through aggregates (Fig 29). Such failure pattern was in turn observed for limestone aggregate concrete.

4.2.2 Model response at moderate and high confinement

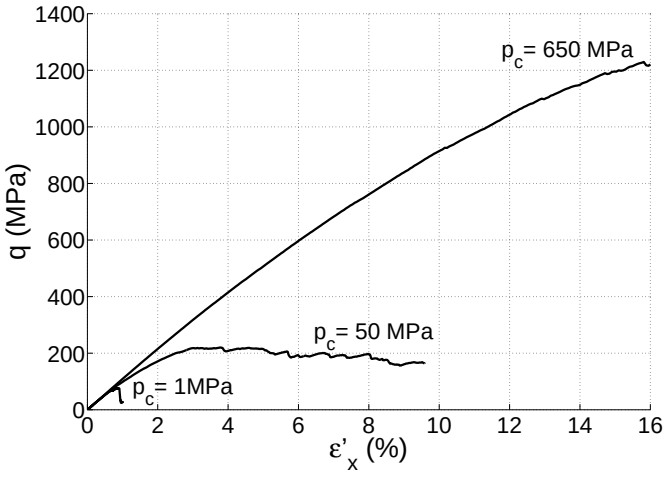

Figure 4.15: Biaxial compression tests conducted at different confining pressures on the reference concrete sample: stress deviator q vs. axial strain ε'_x

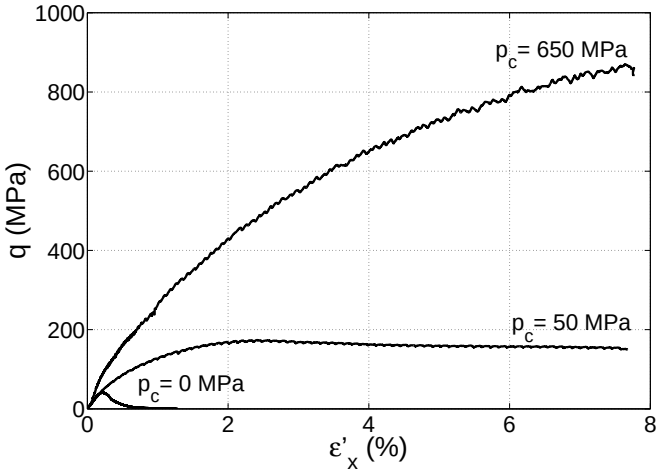

Figure 4.16: Triaxial tests conducted at different confining pressures on siliceous aggregate concrete: stress deviator q vs. axial strain ε'_x

Figure 4.15 displays results of tests conducted at 1 MPa, 50 MPa and 650 MPa on the reference concrete sample . Results of experimental tests performed on siliceous aggregate concrete are recalled in Figure 4.16. The relative shapes of the curves are similar but the stiffness are different. It has been mentioned at the end of the previous chapter, that stiffness parameters, k_n and k_t do not take into account the mesh size. It means that the same microscopic stiffness parameters used with different mesh types would result in different macroscopic stiffness. The parameters used in tests presented in Figure 4.15 were calibrated for a triangular mesh and were not changed for the mesh constructed on granular assembly. Therefore, the behavior of the numerical sample is much less stiff than

the behavior of real concrete specimen. Since the elastic stiffness can be easily adjusted by modifying k_n and k_t (see Fig. 4.17), we will focus here on other aspects of the behavior and not comment the stiffness differences any more.

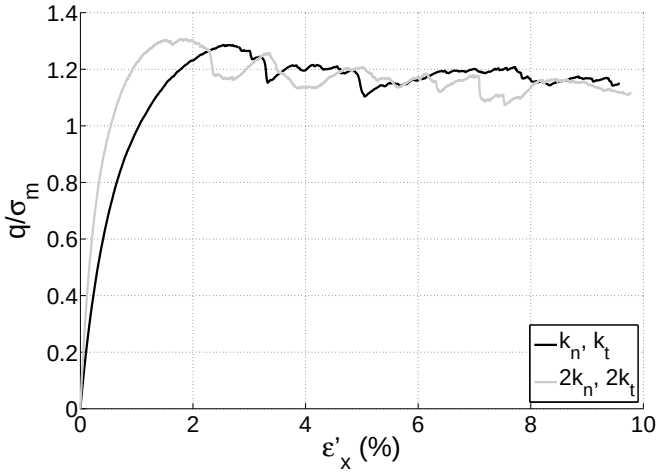

Figure 4.17: Influence of stiffness parameters k_n and k_t on the reference concrete sample; biaxial test at 50 MPa of confinement: stress deviator q to mean stress σ_m ratio vs. axial strain ε'_x

The model reproduces relatively well the increase of concrete strength with the confinement. It is quite efficient to model the behavior of mortar at different confinement levels (see Figures 4.18 and 4.19). Some refinements, such as calibration of friction coefficient for contact interactions could be made to fit more closely experimental results. The model is probably also appropriate to simulate the behavior of soft rock aggregates, such as limestone, which is similar to that of mortar.

Looking closer into the results of simulations, it can be seen that damage mechanisms in the reference concrete sample are very different than those found experimentally in concrete with strong aggregates. Figure 4.20 shows the evolution of damage parameter during biaxial compression conducted at 50 MPa and 650 MPa of confinement on reference concrete sample. It can be seen that at very high confinement, a very large part of aggregate links is broken. On the other hand, at moderate confinement, quite few aggregate links are ruptured. This finding contradicts experimental observations obtained with X-ray tomography and visual estimations: at 50 MPa of confining pressure, several aggregates are broken under shear loading, within the main crack zone; on the contrary, at very high confinement few broken aggregates are observed in the concrete specimen; in the macroscopic cracks aggregates are mainly debonded.

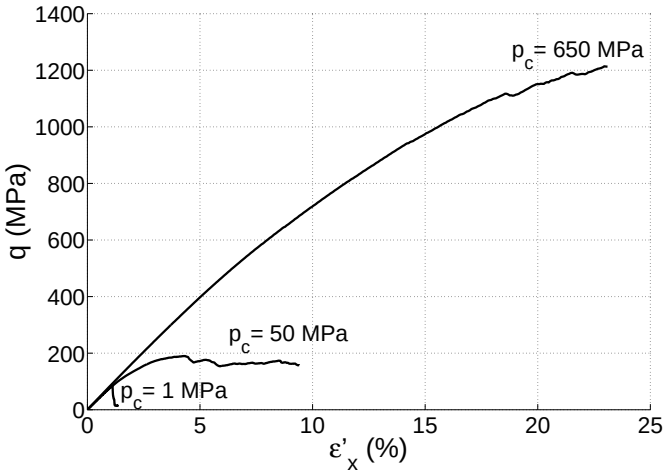

Figure 4.18: Biaxial compression tests conducted at different confining pressures on a numerical mortar sample: stress deviator q vs. axial strain ε'_x

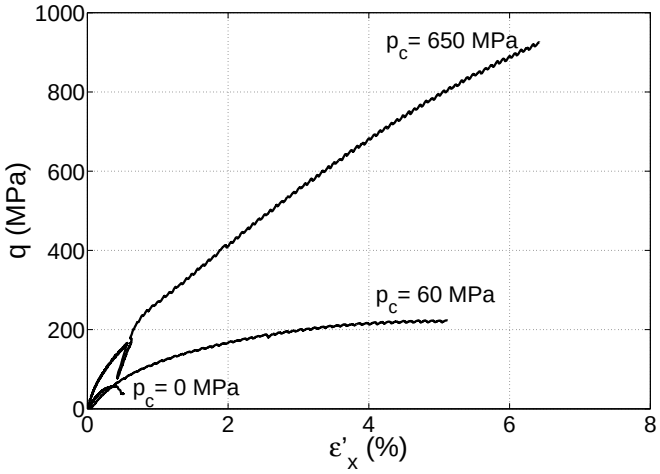

Figure 4.19: Triaxial tests conducted at different confining pressures on mortar: stress deviator q vs. axial strain ε'_x

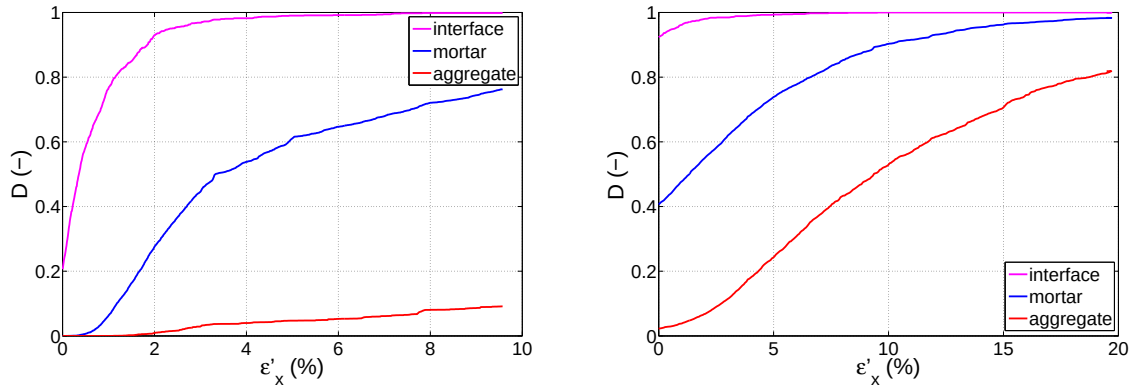

Figure 4.20: Evolution of damage parameter D with axial strain ε'_x at (a) 50 MPa and (b) 650 MPa of confinement for the reference concrete sample

Figure 4.21(a) displays numerical results of biaxial tests conducted at two different confining pressures on the reference aggregate material sample. Results of triaxial tests conducted on siliceous rock are shown in Figure 4.21(b). The proposed model in its present form is not able to reproduce correctly the response of very strong and brittle aggregates. The increase of aggregate strength with confinement in the model is not sufficient. In addition, the behavior of siliceous rock is very brittle at 50 MPa of confining pressure while the behavior of the model is ductile at this level of pressure. This drawback has to be overcome before investigating the effect of aggregate strength on concrete behavior at different confinement levels.

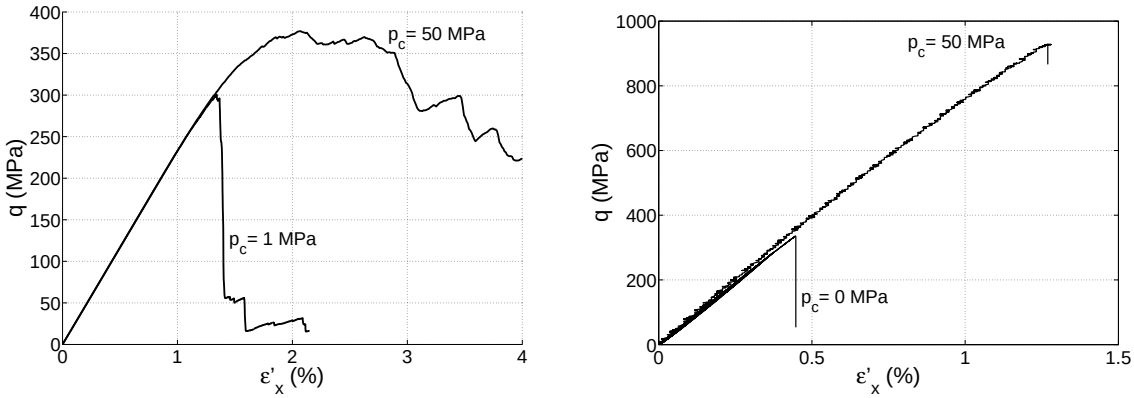

Figure 4.21: Confined compression tests conducted at different confining pressures on the reference aggregate sample: stress deviator q vs. axial strain ε'_x
(a) numerical results
(b) experimental results

The selection of a failure criterion, essential to model correctly the behavior of concrete

and its constituents at different confinement levels, is not an easy task and requires more in-depth calibration. In this first approach, power law criterion (Eq. 4.6), recalled in Figure 4.22 was used for both mortar and aggregate, by varying parameters F_n^0 and F_t^0. This criterion has to be modified in order to better reproduce the increase of aggregate strength with the confinement.

$$\zeta = \left|\frac{F_t}{F_t^0}\right|^5 + \frac{F_n}{F_n^0} - 1 = 0 \tag{4.6}$$

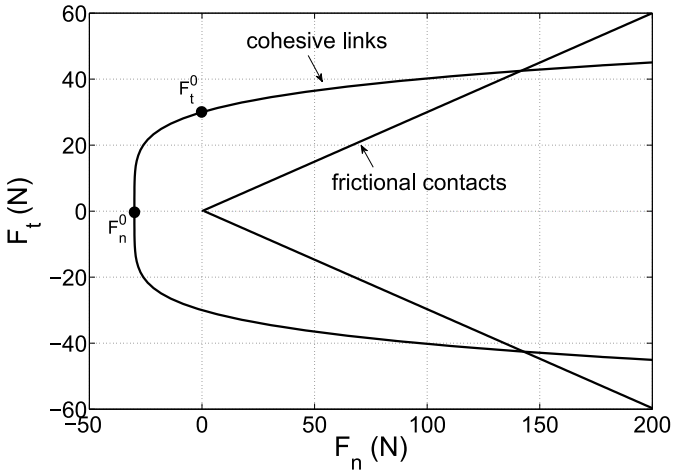

Figure 4.22: Initial failure criterion (crit1): cohesive links - power law with an exponent equal to 5, frictional contacts: Coulomb friction law

Some tests were performed in order to obtain a more realistic aggregate behavior. The first modification regards the power law exponent, which is decreased from 5 to 2. This is usually used in triaxial failure criteria of rocks. The new failure criterion has thus the following form:

$$\zeta = \left|\frac{F_t}{F_t^0}\right|^2 + \frac{F_n}{F_n^0} - 1 = 0 \tag{4.7}$$

In addition, the normal cohesive threshold F_n^0 is reduced and the tangential cohesive threshold F_t^0 increased; their ratio equals 0.5 instead of 1 in the initial parameters set. This modified criterion is presented in Figure 4.23(a). A higher shear threshold will increase a bit the strength of aggregate sample at 1 MPa of confinement. However, this increase will not affect the behavior of concrete, since with previous criterion (crit1) the aggregates in the reference concrete sample tested at very low confinement were already not broken. Figure 4.24(a) displays the response of the reference rock sample at 50 MPa of confinement obtained with the new failure criterion (crit2), in comparison with the results got with the initial criterion (crit1). The increase of aggregate strength can be observed.

Once a link breaks in shearing, it becomes a contact if it is under compression. In this case, if the breaking force is higher than the maximal force for contacts, there will

be a drop in the F_t value (see Fig. 4.23(a)). This drop, affecting macroscopic results, could be reduced with different criterion for frictional contacts (or much higher friction coefficient). Thus the peak stress value is controlled in a large part by the microscopic friction coefficient.

A third criterion is thus considered to test the influence of this drop; the modification concerns frictional contacts. Instead of Coulomb law, a parabolic friction law, with $F_n^0 = 0$, is used also for contacts. The corresponding stress-strain curve is presented in Figure 4.24(b). This 3rd criterion provides a higher strength of the aggregate sample comparing to the 2nd criterion what proves that the low friction coefficient previously used with the parabolic failure criterion for cohesive links strongly reduces aggregate macroscopic strength.

It is very difficult to reproduce aggregate brittleness under confinement, probably due to large part of broken cohesive links still working as contacts. However, it was observed that reducing tensile cohesive threshold to shear threshold ratio enhances material brittleness.

More tests would have to be performed to establish the correct set of parameters controlling mortar and aggregate strength and to efficiently use the model in further investigations. Due to time constraints, this issue could not be developed in this report.

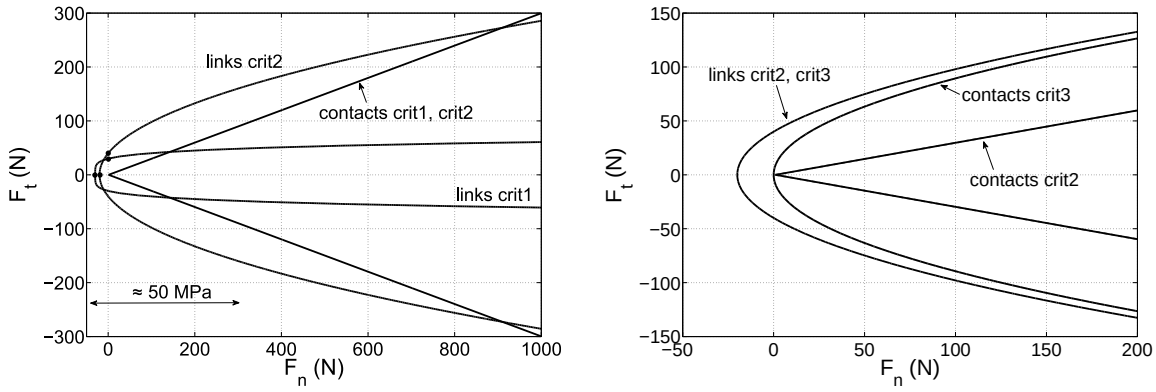

(a) (b)

Figure 4.23: Initial and modified failure criteria
(a) crit1: cohesive links - power law 5, contacts - Coulomb friction law
crit2: cohesive links - parabolic law, contacts - Coulomb friction law;
(b) crit2: cohesive links - parabolic law, contacts - Coulomb friction law
crit3: cohesive links - parabolic law, contacts - parabolic law

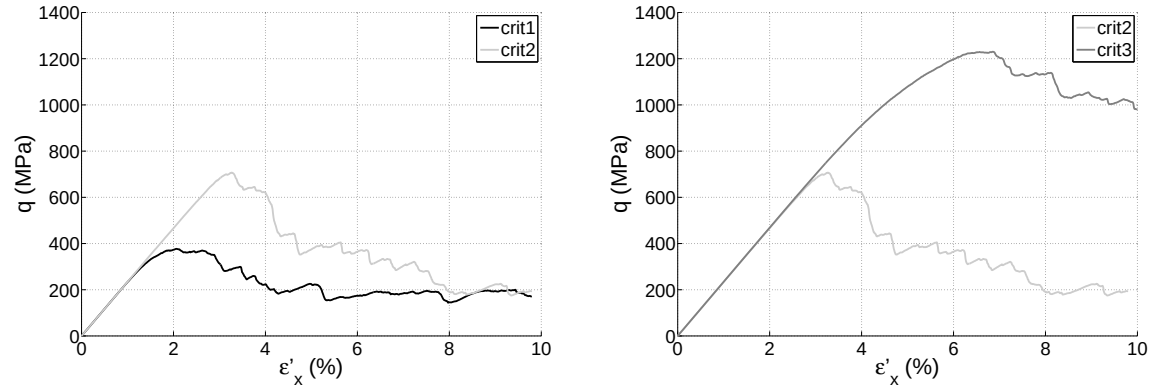

(a) (b)

Figure 4.24: Comparison of biaxial compression tests conducted at 50 MPa of confinement on an aggregate sample using different failure criteria: stress deviator q vs. axial strain ε'_x

4.3 Chapter conclusion

Mesoscopic, discrete model of concrete was used to study the behavior of concrete under confined compression. More specifically, the influence of concrete large-scale heterogeneities on the model's behavior was investigated.

The first part, concerning the influence of porosity, has revealed novel results that it is possible to reproduce the non linear compaction process of mortar using a linear interaction law. This compaction behavior was proved to be dependent on the void volume ratio but also a lot, on voids size. This issue has to be studied more profoundly to establish a valid link between the behavior of a real concrete and a porous numerical specimen, but the outcome obtained in this first study is very promising.

The second part focused on the effect of aggregate and interface strength on concrete behavior at different levels of confinement. Some previously described experimental results of triaxial tests conducted on concretes made with different type coarse aggregates were briefly recalled; a qualitative comparison with the model was made. The model's behavior at very low confinement is consistent with experimental observations. The important role of aggregate/mortar interface strength in the concrete strength was observed and the different failure patterns found in concrete samples under uniaxial compression were well reproduced.

The investigation under high confinement encountered more difficulties. At the current stage of development, the model appeared not appropriate to well reproduce the behavior of concrete, and, more specifically, the behavior of strong aggregates in a concrete sample. Some modifications of the model concerning local failure criterion were proposed. However, this part of the model still has to be improved in order to be able to study and well understand the behavior of concrete under a wide range of confining pressures.

Conclusion and perspectives

Today's dependency on massive infrastructure and increasing demand for safety lead to the necessity of thorough understanding of concrete behavior under severe loadings. The present work was interested in triaxial behavior of dry concrete at different stress levels. In order to complete previous research efforts, the influence of concrete large-scale heterogeneities, such as coarse aggregates, on its macroscopic behavior and damage mechanisms was examined. The work presented in this thesis consisted of both experimental and numerical investigations.

Bibliographic review provided a general introduction to the studied subject. The different scale heterogeneities in concrete material were first presented. Conventionally, concrete is represented as large aggregates embedded in a cohesive matrix. This matrix is made of cement paste and fine aggregates and characterized by the presence of porosity. The cement matrix also exhibits an important heterogeneity in the vicinity of aggregates: the interfacial transition zone (ITZ). Some relatively new and very powerful techniques used to explore the internal structure of concrete, such as X-ray tomography, were also mentioned.

Subsequently, the main aspects of concrete behavior under triaxial loading were discussed. The compactant behavior of concrete under hydrostatic compression and the influence of confining pressure under confined compression, such as increase of concrete strength and ductility with the confinement, were underlined. Triaxial behavior of concrete was presented in more details in relation to its composition, such as water/cement ratio, saturation ratio or coarse aggregate volume and size. Nevertheless, the influence of coarse aggregate type on concrete response at high stress levels is not yet reported in the literature.

Finally, different methods of concrete modeling at the meso-scale were cited. Recently widely developed, mesoscoping modeling takes into account the largest concrete heterogeneities, such as coarse aggregates, interfacial transition zone and also macroporosity. This approach allows better understanding of damage and failure mechanisms of concrete that come from its heterogeneity and may be used as a cost-effective means of formulating optimized concrete mixes.

The 2nd chapter of this manuscript was consecrated to the experimental study of coarse aggregate type effect on concrete triaxial behavior at different confinement levels. An exhaustive experimental investigation was performed on concretes distinguished either by coarse aggregate shape or composition. Some tests were also done on aggregate itself (rock sample).

One of the most striking results was that the coarse aggregate shape exerts practically no influence on concrete behavior under high confinement. The shear strength of concrete seems to be controlled by the compacted cement matrix provided aggregate strength sufficiently higher than that of mortar. Otherwise, a lower-strength aggregate reduces overall concrete strength at very high confinement.

The shear strength of concrete is mainly controlled by the aggregate strength at moderate confinement levels (50 MPa) and by the aggregate/mortar interface in unconfined compression test. Additionally, in these two loading types, rough angular aggregates increase the overall concrete strength.

This experimental study also revealed that aggregate composition strongly influences the failure pattern in concrete samples at high confinement. Depending on the aggregate strength, macroscopic cracks pass either through both mortar and aggregates (weak aggregate) or they are localized in mortar and characterized by aggregate debonding (strong aggregate).

The two subsequent chapters concerned numerical modeling of concrete at the mesoscopic scale. The main objective of this numerical work was to develop a very simple model in terms of interaction laws (elastic-brittle elements), which is not a common practice in concrete modeling, and introduce concrete heterogeneity at the mesoscopic level. Therefore, two types of interactions were used: initial cohesive links, whose behavior was described by a linear elastic-brittle law, and frictional contacts detected during the simulation. On the other hand, numerical concrete specimen was composed of three material phases described with different mechanical parameters: matrix, aggregate and interface, which corresponds to the classical representation of concrete mesostructure. As an additional feature, voids were introduced in a matrix phase by removing a number of mortar nodes.

Chapter 3, brought up some general aspects of the model. Originally, a network of cohesive bonds was constructed on a triangular grid. Such mesh was found not much suitable to be subjected to confined compression loading and was finally replaced by an isotropic granular assembly, as typically used in DEM. Validation tests showed that the proposed model can be used, after some refinements, to simulate deviatoric behavior of concrete at different confinement levels. Introducing porosity in the numerical sample appeared to be an interesting point of the model; hydrostatic compression performed on a porous sample revealed novel result showing that it is possible to reproduce compaction behavior of mortar using linear interaction law, the non-linearity being originated from the void structuring.

The influence of porosity on macroscopic response of the numerical sample was more developed in chapter4. The combined effect of void size and void volume fraction on the nonlinearity of hydrostatic behavior was underlined.

The model was also used to investigate the effect of aggregate and interface mechanical properties on the response of a concrete specimen. Different values of microscopic model's parameters, corresponding to the cohesive strength of aggregate and interface, were used to test the behavior of the concrete sample at very low confinement. Since the model was in its early development stage, the purpose was not to fit experimental results but to perform, a qualitative comparison with experimental observations. Within

these objectives, the model was found efficient at very low confinement. It simulated well differences in maximum stress values for concrete samples, due to different aggregate and interface strength properties. It was also able to reproduce failure patterns observed in real concrete samples.

The investigation of the same aspects under more important confining pressure encountered more difficulties, especially in the modeling of strength and brittleness of the aggregate phase. The initial choice of failure criterion was probably not well adapted to model the behavior of strong aggregates at different confinement levels. Some improvements concerning the local failure criterion were proposed; however, further studies has to be performed to validate this part of the model. Therefore, for the moment, it remains in the perspectives field.

Some perspectives

The presented numerical study can be recognized as work in progress. The numerical model was developed during this PhD thesis and still has to be improved in order to be used in more specific problems. First of all, the simplifications made in the first study should be corrected so that the study concerning the influence of aggregate strength on concrete behavior could be completed over a wider range of confining pressures. We have enlightened the crucial role of the failure criterion when high confining pressures are considered and proposed a solution to overcome this limitation. Moreover, more precise calibration of model's parameters is required in order to correctly reproduce the behavior of mortar, aggregate and concrete and perform more quantitative comparisons with the experimental results. In the next step, different aggregate shapes could be considered.

On the other side, the study on the influence of porosity opens many perspectives. Since, this issue was investigated only on a homogeneous sample, it would be interesting to perform a wider study on a concrete specimen. More heterogeneous void size distribution, corresponding more closely to the porosity of a real concrete specimen, could be used. Local information in a sample may also be analyzed, such as for example local volume changes in a porous sample with or without large aggregates.

In further investigations, it would be possible to account for microporosity, *i.e.* typical size below the link size, in addition to the macroporosity arising from geometrical structuring. This feature can be realized by incorporating irreversible compressive volumetric strains in the force-displacement relation (tangential plasticity used in the model does not induce volume changes). Such modification could be helpful to reproduce failure patterns observed experimentally at very high confinement (horizontal bands).

It is well known that the water phase plays an important role in concrete strength at high stress level. It would be thus interesting to take into account in the model the effect of free water filling the macro-pores. For this purpose, void nodes previously removed from the specimen would be replaced by water nodes, with appropriate mechanical behavior associated to the line elements connecting water nodes. In further perspectives, the liquid percolation through the mortar phase could be also consider.

Résumé en français

Cette partie fournit le résumé détaillé, chapitre par chapitre, du travail de cette thèse. Les méthodes utilisées ainsi que les résultats les plus marquants sont rapportés. Certaines questions de moindre importance ne sont pas considérées.

Introduction générale

Le contexte général du projet de recherche entourant cette thèse est la vulnérabilité des infrastructures complexes en béton (immeubles de grande hauteur, barrages, réacteurs nucléaires, *etc*) sous chargements extrêmes, tels que des détonations en champ proche ou des impacts balistiques. Dans ces situations, le béton subit de très fortes contraintes triaxiales (Zukas [71]). Lorsqu'un projectile frappe une structure en béton, divers effets localisés sont générés: l'écaillage sur la face avant de la structure peut être associée à de la traction simple, tandis que la pénétration du projectile dans l'intérieur de la structure constitue une compression triaxiale dynamique. Si la cible est suffisamment mince, des contraintes de traction simple et de cisaillement peuvent être observées sur la face distale de l'échantillon de béton au cours de la phase finale de pénétration.

La possibilité de reproduire le comportement du béton sous ces conditions extrêmes avec un modèle numérique est essentielle puisque les tests dynamiques à grande échelle et les tests de laboratoire sont très coûteux et chronophages. Une validation des modèles de comportement du béton, qui prennent en compte simultanément les phénomènes d'endommagement fragile et de déformations irréversibles, exige des résultats de tests qui permettent de reproduire ces trajets de chargement complexes et intenses.

La caractérisation statique d'un modèle de comportement devant prédire des phénomènes dynamiques représente une pratique courante dans l'étude des géomatériaux. Le comportement du béton dans les essais de compression confinée dépend peu de la vitesse de déformation pour les échantillons secs ou mouillés (Forquin *et al.* [28]). La compression triaxiale statique est donc le type de chargement concerné par ce travail.

En 2004, l'université de Grenoble a lancé, en collaboration avec le CEA Gramat, un programme de recherche sur la vulnérabilité des infrastructures en béton. Une presse triaxiale de grande capacité a été installée dans le laboratoire 3SR (Université de Grenoble). Grâce à ce dispositif novateur, une grande campagne expérimentale a été effectuée. Les études expérimentales ont porté sur l'influence du trajet de chargement (Gabet *et al.* [30], Poinard *et al.* [49]), du rapport eau/ciment, du degré de saturation, de la taille des gros granulats et du volume de pâte de ciment (Vu *et al.* [66, 67, 64]), sur le comportement du béton sous fort confinement. Ce programme de recherche a été récemment incorporé

dans le projet scientifique PREVI (Pôle de Recherche sur la Vulnérabilité des Infrastructures), reconnu par le ministère français de la recherche, qui regroupe des laboratoires de trois universités: le laboratoire 3SR (Université de Grenoble), le LML (Université de Lille 1), le LEM3 (Université de Lorraine), et un organisme de recherche scientifique, le CEA Gramat. Ces unités visent à caractériser, comprendre et modéliser le comportement du béton sous sollicitations extrêmes.

Dans ce contexte, la partie expérimentale de ce travail vise à étudier l'effet des gros granulats sur le comportement du béton pour les essais de compression triaxiale allant de 0 à 650 MPa de confinement. Cette question est certainement intéressante car les plus gros granulats occupent environ 40% du volume de béton. En outre, ils présentent différentes propriétés en fonction des propriétés de la roche-mère et du processus de création, soit une érosion naturelle, soit un écrasement mécanique. On étudiera ici à la fois l'influence des formes et textures de la surface des granulats, et l'influence de leur composition.

La seconde partie du manuscrit est consacrée à la modélisation numérique. En raison de sa nature fortement hétérogène (présence de gros granulats, de porosité, ...), le béton peut être considéré à différentes échelles, ce qui est illustré dans la Figure 1. Puisque nous étudions ici l'influence des gros granulats sur le comportement du béton, un modèle mésoscopique du béton est développé. La modélisation mésoscopique vise à mieux comprendre les mécanismes d'endommagement et de rupture du béton qui viennent de son hétérogénéité. L'importance de la méso-porosité a été soulignée dans les observations tomographiques d'échantillons de béton soumis à une compression hydrostatique (Poinard *et al.* [50]). La Figure 2 montre une sélection d'images de cette étude. Le deuxième objectif de la modélisation mésoscopique est d'être capable de déduire le comportement macroscopique du béton à partir de la connaissance des comportements de ses composants. Un modèle efficace et précis pourrait servir comme un outil d'optimisation de mélange du béton, de sorte que le nombre d'expériences pourrait être réduit.

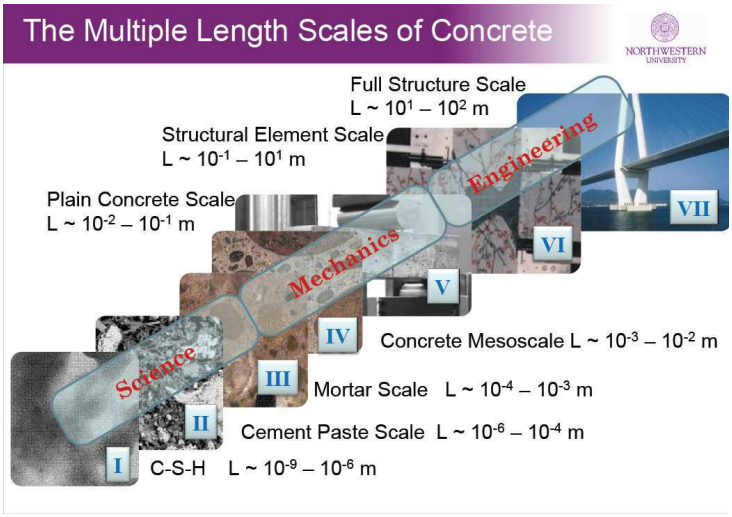

Figure 1: Multiples longueurs d'échelle de béton (G. Cusatis, International PREVI Workshop on Concrete Structures under Impact and Blast Loads, 2013, Les Houches, France)

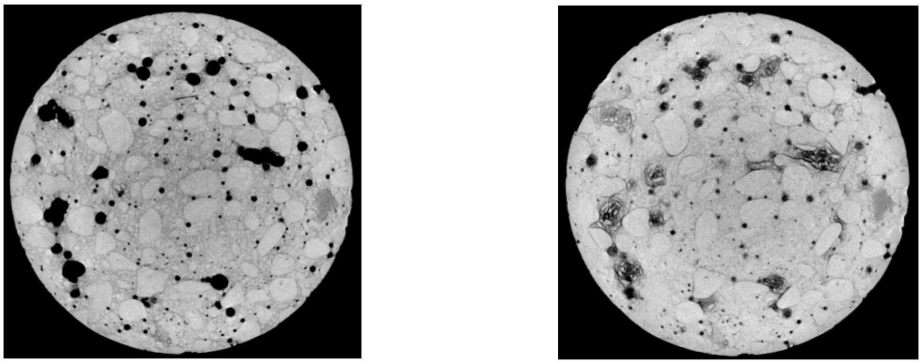

(a) (b)

Figure 2: Coupe horizontale d'un échantillon de béton soumis à une compression hydrostatique (Poinard [50]): (a) état vierge, (b) après 650 MPa

Étude expérimentale

Cette section résume une caractérisation expérimentale du comportement triaxial du béton à différents niveaux de confinement en s'intéressant à l'influence du type des plus gros granulats.

Dispositif expérimental: presse triaxiale

Les essais triaxiaux ont été réalisés au moyen d'une presse triaxiale de grande capacité, appelée GIGA. Une description complète des procédures d'essais sur le béton a été présentée en détail dans [65]. La presse, représentée à la figure 3, est capable de générer une pression de confinement jusqu'à 0,85 GPa et d'atteindre une contrainte axiale de 2.3 GPa pour des échantillons cylindriques de béton de 70 x 140 mm.

Figure 3: Vue d'ensemble de la presse GIGA

La presse est équipée de différents capteurs qui servent à surveiller les essais et fournir des informations sur l'état de l'échantillon pendant le chargement. Un capteur de déplacement axial et un capteur de pression contrôlent le trajet de chargement.

Les mesures de déformation de l'échantillon sont effectuées à l'aide d'un capteur LVDT, d'une jauge axiale et de deux jauges circonférentielles.

Dans ce mémoire, les contraintes de compression et les déformations de contraction sont positives. On note σ_x la contrainte axiale principale, p_c la pression de confinement,

σ_m la contrainte moyenne et q la différence des contraintes principales:

$$\sigma_m = \frac{\sigma_x + 2p_c}{3} \tag{4.8}$$

$$q = \sigma_x - p_c \tag{4.9}$$

Le chargement de compression triaxiale est appliqué en deux phases: une hydrostatique, puis une déviatorique. La phase hydrostatique consiste à appliquer une pression de confinement autour de l'échantillon, jusqu'à une valeur désirée. Une fois que le confinement désiré a été atteint, l'échantillon est chargé axialement à une vitesse de déplacement constante, tandis que la pression de confinement est maintenue constante. On procède dans l'ordre inverse pour la phase de déchargement.

Les essais de compression uniaxiale ont été réalisés sur une presse différente, *ie* une presse Schenk de capacité 100 tonnes. Ces tests ont été commandés en déplacement.

Caractéristiques des échantillons de béton

Cette étude a été réalisée sur quatre échantillons de béton qui se distinguent par le type de granulats. Le béton de référence (SR) contient des granulats roulés siliceux provenant d'un gisement naturel. Ce béton SR est un béton ordinaire en termes de résistance (30 MPa) et d'affaissement (7 cm). Les trois bétons modifiés contiennent tous le même volume de matrice cimentaire, le même volume de granulats et une distribution de taille des granulats aussi proche que possible de la composition de référence. Ils ne différent que par le type des granulats dans leur composition: le béton de granulats concassés (SC) contient des granulats concassés obtenus à partir de roche siliceuse; dans le béton de billes de verre (GB), les granulats sont remplacés par des billes de verre; le béton de granulats calcaires (LC) présente finalement des granulats concassés provenant d'une roche calcaire tendre.

Influence de la forme des granulats

Des essais triaxiaux ont été effectués sur les trois échantillons de béton à base des granulats suivants: roulés, concassés et billes de verre. Les propriétés physiques des trois types de granulats sont comparables. En revanche, ils présentent de fortes différences de formes et de textures de surface. Cette étude a donc principalement porté sur les caractéristiques externes, tout en gardant à l'esprit que le verre est un matériau assez différent du gravier ou de la roche siliceuse.

Essai de compression simple

La Figure 4 montre les résultats des essais de compression simple effectués sur les trois bétons étudiés. Tous les trois bétons présentent des propriétés élastiques très similaires, bien que des différences de contrainte ultime soient notées. Le béton de bille de verre présente une résistance nettement moindre que le béton fait avec des granulats roulés ou concassés. La plus grande résistance est trouvée pour le béton de granulats concassés.

La résistance uniaxiale d'un béton ordinaire est contrôlée par la résistance à l'interface mortier/granulat, qui est la zone la plus faible dans un béton constitué de granulats assez résistants. Les granulats sphériques très lisses développent des liaisons interfaciales plus faibles, ce qui résulte en une basse résistance du béton GB. Une légère augmentation de la résistance lors de l'introduction des granulat concassés est en effet observée. On suppose que la composition presque identique des granulats roulés et concassés donne une rugosité de surface microscopique semblable et, par conséquent, une force de liaison interfaciale comparable. En revanche, les granulats concassés ont une rugosité mésoscopique supérieur à celle des granulats roulés, et cette constatation se traduit par une plus grande résistance du béton, probablement en raison de l'imbrication mécanique des granulats et de la matrice cimentaire.

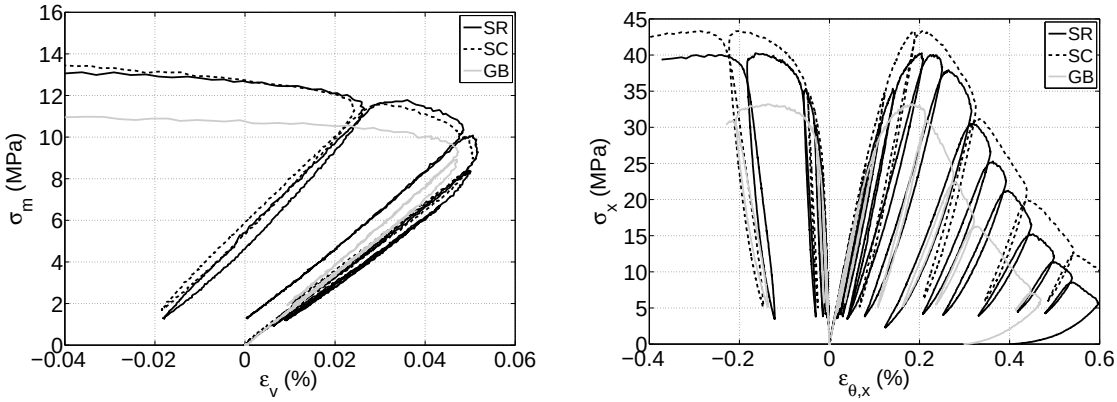

(a) (b)

Figure 4: Essais de compression simple sur des bétons ayant des granulats roulés (SR), des granulats concassés (SC) et des billes de verre (GB): (a) contrainte moyenne σ_m vs. déformation volumique ε_v, (b) contrainte axiale σ_x vs. déformations ε_θ and ε_x

Essai triaxial à 50 MPa de confinement

La Figure 5 présente les résultats d'essais triaxiaux réalisés à 50 MPa de confinement sur des échantillons de bétons avec des granulats roulés, des granulats concassés et des billes de verre. La Figure 5(b) indique les différences de contrainte maximale déviatorique. La résistance la plus basse est obtenue pour le béton de granulats roulés et la plus haute pour le béton de billes de verre. En outre, le béton de billes de verre présente un comportement plus rigide et un pic de contrainte plus prononcé que les deux autres échantillons. La contrainte à la rupture du béton de granulats concassés est légèrement supérieure à celle du béton de granulats roulés.

Pour expliquer ces différences, il est utile de comparer les modes de rupture observés pour les trois échantillons (voir Fig. 6). Les bétons de granulats roulés et de granulats concassés présentent tous les deux des faciès de fissuration très similaires. Le mécanisme de rupture est très localisé dans quelques fissures inclinées à 30° par rapport à la direction axiale. Certains grands granulats sont cassés, en particulier dans l'échantillon de granulats

concassés. Comme en compression simple, la plus grande résistance du béton SC est probablement due à la rugosité élevée des granulats concassés.

Le réseau de fissures dans le béton de billes de verre est très différent des deux autres. Plusieurs fissures perpendiculaires à la direction axiale sont observées; on observe un phénomène de décollement des billes de verre. Selon toute vraisemblance, cette tendance à la fissuration est principalement due à la résistance des billes de verre et sera discutée dans la section suivante.

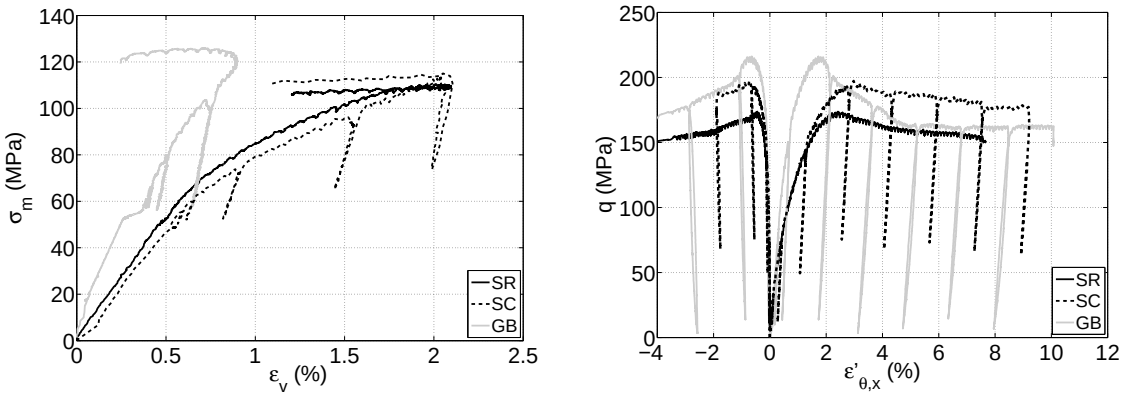

(a) (b)

Figure 5: Essai triaxial à 50 MPa de confinement sur des bétons ayant des granulats roulés (SR), des granulats concassés (SC) et des billes de verre (GB): (a) contrainte moyenne σ_m vs. déformation volumique ε_v, (b) contrainte déviatorique q vs. déformations ε'_θ and ε'_x

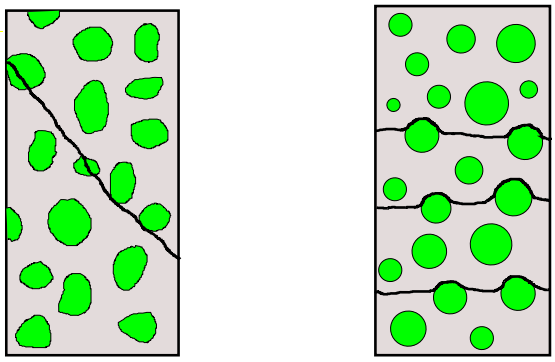

(a) (b)

Figure 6: Croquis des faciès de rupture des échantillons de béton à 50 MPa de confinement: (a) béton de granulats siliceux (SR, SC), (b) béton de billes de verre (GB)

Essai triaxial à 650 MPa de confinement

La Figure 7 présente les résultats d'essais triaxiaux à 650 MPa de confinement menés

sur les trois bétons étudiés. Le comportement volumique (voir Fig. 7(a)) suggère une déformabilité légèrement inférieure de béton de billes de verre.

Le comportement déviatorique montré à la Figure 7(b) indique que sous très haut confinement, les trois bétons se comportent à peu près similairement en termes de contrainte ultime et de raideur tangentielle.

Leurs modes de rupture respectifs sont également très similaires. Une série de fissures perpendiculaires à la direction axiale avec décollement considérable, ainsi que quelques granulats cassés sont observés. À ce niveau de confinement, le béton se comporte comme un empilement granulaire non cohésif. En raison de la présence de la matrice cimentaire détruite entre les granulats, leur forme globale n'a aucun effet sur le comportement de cet assemblage granulaire. Son comportement est susceptible d'être commandé par la matrice de ciment compacté entre les plus grands granulats.

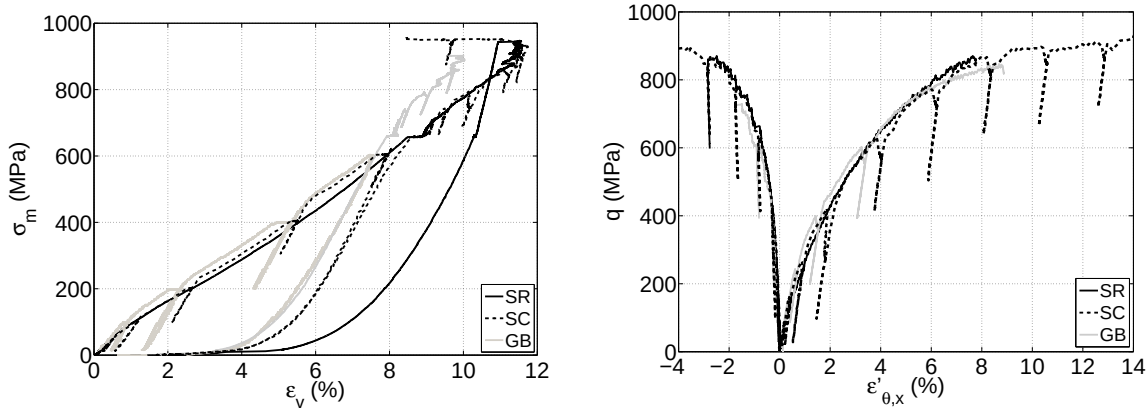

(a) (b)

Figure 7: Essai triaxial à 650 MPa de confinement sur des bétons ayant des granulats roulés (SR), des granulats concassés (SC) et des billes de verre (GB): (a) contrainte moyenne σ_m vs. déformation volumique ε_v, (b) contrainte déviatorique q vs. déformations ε'_θ and ε'_x

Influence de la composition des granulats

Cette section considère l'effet de la composition des granulats grossiers sur le comportement triaxial du béton. Les bétons incluant des granulats siliceux roulés (SR) ou des billes de verre (GB) seront analysés ici, en s'intéressant plus particulièrement à la résistance et aux propriétés élastiques. Ces caractéristiques, telles que définies à partir des essais de compression simple, sont résumées dans le Tableau 1. Le verre présente des propriétés mécaniques très intéressantes, même si elles varient largement en fonction de la composition du mélange, des conditions de production, *etc.* La valeur de la résistance en compression généralement admise est de 1 GPa, il est donc considéré ici que la résistance à la compression de billes de verre dépasse de loin celle des granulats siliceux (330 MPa).

Les comportements des bétons avec des granulats concassés siliceux (SC) et des granulats concassés de calcaire (LC), qui présentent tous les deux des propriétés physiques et

mécaniques très différentes (voir Tab. 1), ont également été comparés. La porosité de la roche calcaire, égale à 9,4%, est très élevée par rapport à la porosité de la roche siliceuse, *i.e.* <2%.

Type de granulats	**Siliceux**	**Verre**	**Calcaire**
Masse volumique $[g/cm^3]$	2.6	2.5	2.3
Module de Young $[GPa]$	78	70	51
Coefficient de Poisson $[-]$	0.12	0.22	0.28
Résistance à la compression $[MPa]$	330	1000	150

Table 1: Les propriétés physiques et mécaniques des granulats

Essai de compression simple

La Figure 8 montre les résultats des essais de compression uniaxiale effectués sur les bétons de granulats siliceux et de granulats calcaires. Pour le béton de granulats calcaires, le module de Young et le coefficient de Poisson, évalués à partir de la partie linéaire du comportement axial, sont inférieurs à ceux du béton de granulats siliceux. La résistance uniaxiale du béton de granulats calcaires, qui se situe entre 55 et 59 MPa, est nettement supérieure à celle du béton de granulats siliceux. Par ailleurs, des fissures traversent les granulats calcaires, alors qu'ils ont tendance à contourner les granulats siliceux. Ces observations confirment l'importance de la zone de transition interfaciale dans le comportement uniaxial du béton. La liaison interfaciale forte obtenue avec des granulats calcaires s'explique à la fois par une forte porosité et une absorption. En outre, certaines liaisons chimiques peuvent avoir lieu entre le calcaire et la matrice de ciment suite à une réaction entre la calcite des granulats et l'hydroxyde de calcium du ciment hydraté [43].

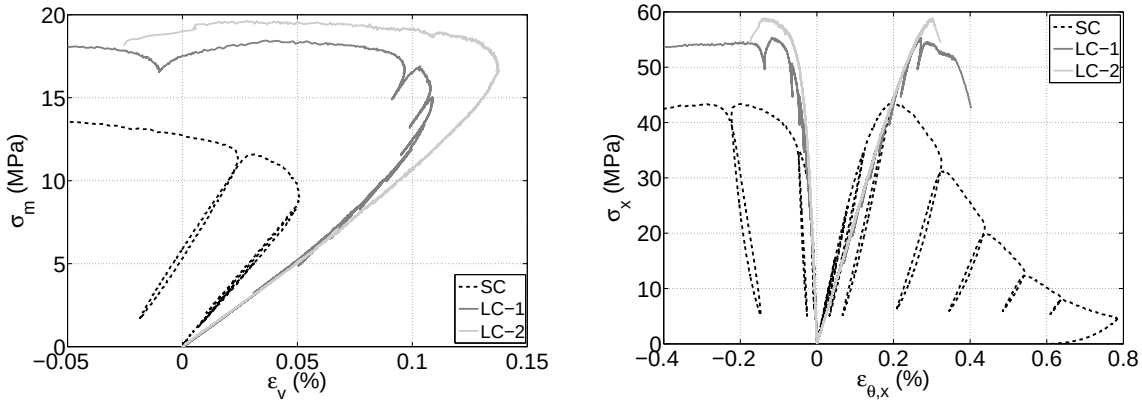

(a) (b)

Figure 8: Essais de compression simple sur des bétons ayant des granulats siliceux (SC) et des granulats calcaires (LC): (a) contrainte moyenne σ_m vs. déformation volumique ε_v, (b) contrainte axiale σ_x vs. déformations ε_θ and ε_x

Essai triaxial à 50 MPa de confinement

La Figure 9 présente le comportement axial du béton, avec des granulats siliceux roulés (SR) ou des billes de verre (GB), testé sous 50 MPa de pression de confinement. La valeur maximale du déviateur est beaucoup plus élevée pour le béton de billes de verre plutôt que pour le béton de granulats siliceux. Cette différence de contrainte ultime s'explique probablement par la résistance des granulats, qui est considérablement plus élevée pour les billes de verre que pour les granulats siliceux. Cette différence de résistance protège les billes de verre de la rupture par cisaillement et conduit par ailleurs à un modéle de fissuration complètement différent dans l'échantillon de béton de billes de verre, par rapport à celui observé pour les autres bétons (voir Fig. 6).

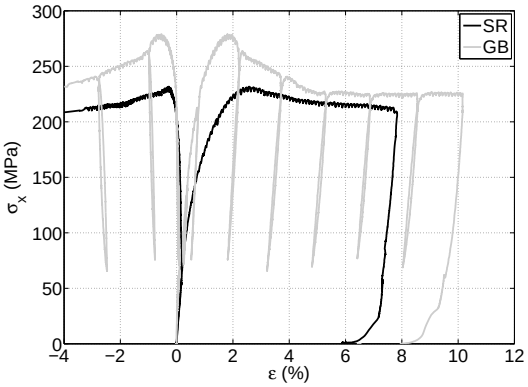

Figure 9: Essai triaxial à 50 MPa de confinement sur des bétons ayant des granulats siliceux (SR) et des billes de verre (GB): contrainte axiale σ_x vs. déformations ε'_θ and ε'_x

La Figure 10 présente les résultats de l'essai triaxial réalisé à 50 MPa de confinement sur les béton de granulats siliceux et de granulats calcaires. La courbe contrainte-déformation du béton de granulats calcaires, visualisée sur la Figure 10(b), présente un plateau, tandis qu'un pic de contrainte se produit pour le béton de granulats siliceux. Le déviateur maximum atteint par le béton de granulats siliceux est légèrement supérieur à celui du béton avec granulats calcaires. Ce résultat est attribuable à la composition des granulats. En raison de la forte liaison interfaciale et d'une faible résistance des granulats dans l'échantillon LC, une grande quantité de ceux-ci est cassée en cisaillement; néanmoins, la diminution de résistance due à l'utilisation de granulats calcaires tendres reste assez limitée.

Essai triaxial à 200 MPa de confinement

La Figure 11 représente les résultats des essais triaxiaux réalisés à 200 MPa de confinement sur les bétons de granulats siliceux et de billes de verre. La raideur volumique du béton de billes de verre est supérieure à celle du béton de granulats siliceux, ce qui résulte des différentes propriétés élastiques des granulats, qui représentent environ 40% du volume de béton.

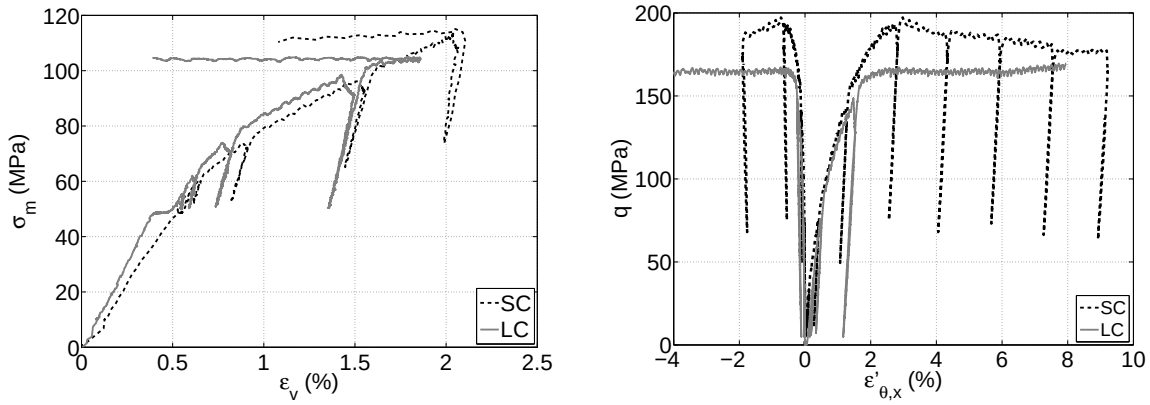

(a) (b)

Figure 10: Essai triaxial à 50 MPa de confinement sur des bétons ayant des granulats siliceux (SC) et des granulats calcaires (LC): (a) contrainte moyenne σ_m vs. déformation volumique ε_v, (b) contrainte déviatorique q vs. déformations ε'_θ and ε'_x

La Figure 11(b) révèle que la contrainte maximale déviatorique est exactement la même pour les béton de granulats roulés et de billes de verre. La raideur tangentielle est presque la même pour les deux échantillons. À ce niveau de confinement, la matrice cimentaire perd sa nature cohésive. Le test a également révélé que la plus grande résistance des granulats n'augmente pas la résistance déviatorique du béton lorsque la matrice de ciment est fortement endommagée.

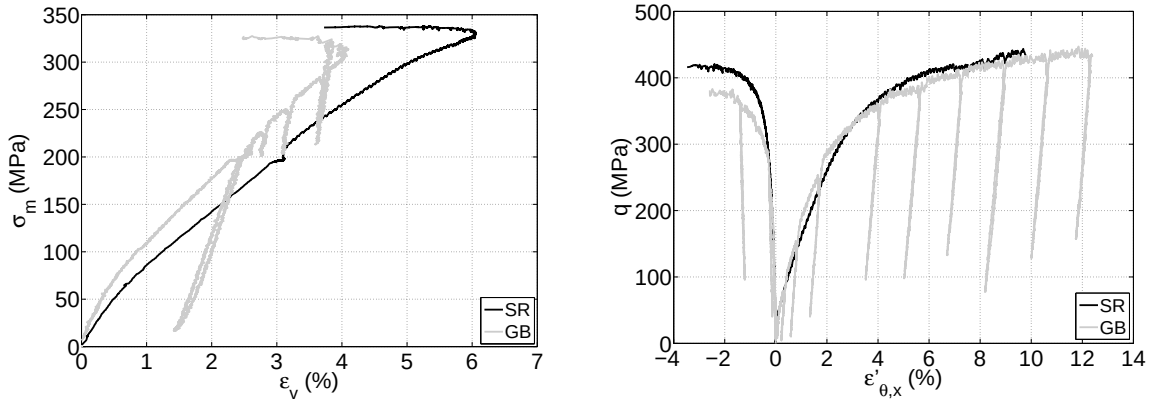

(a) (b)

Figure 11: Essai triaxial à 200 MPa de confinement sur des bétons ayant des granulats siliceux (SR) et des billes de verre (GB): (a) contrainte moyenne σ_m vs. déformation volumique ε_v, (b) contrainte déviatorique q vs. déformations ε'_θ and ε'_x

En raison d'un manque de résultats pour le béton de granulats siliceux concassés à 200 MPa de confinement, le béton de granulats calcaires est comparée au béton de granulats siliceux roulés. La Figure 12 montre les résultats des tests effectués à 200

MPa de confinement sur ces deux échantillons. En accord avec les résultats des tests à 50 MPa, la raideur volumique est légèrement plus élevée pour le béton de granulats calcaires au début de l'étape de chargement. Au-delà d'une contrainte moyenne de 50 MPa, une diminution de la rigidité peut être observée et par la suite la déformation volumique est plus élevée pour le béton LC. Cette réduction de la rigidité est attribuée à un endommagement progressif et au processus de compactage (fermeture de la porosité) de la matrice de ciment. La réduction est encore plus prononcée dans le béton LC car à ce niveau de contrainte moyenne, les granulats calcaires tendres subissent d'importantes déformations plastiques supplémentaires en raison de la fermeture de leur porosité.

Au cours de la phase déviatorique, le comportement du béton de granulats siliceux est nettement plus rigide. Néanmoins, les deux bétons atteignent le même niveau de contrainte finale. La résistance des granulats n'affecte pas la contrainte maximale déviatorique à ce niveau de confinement.

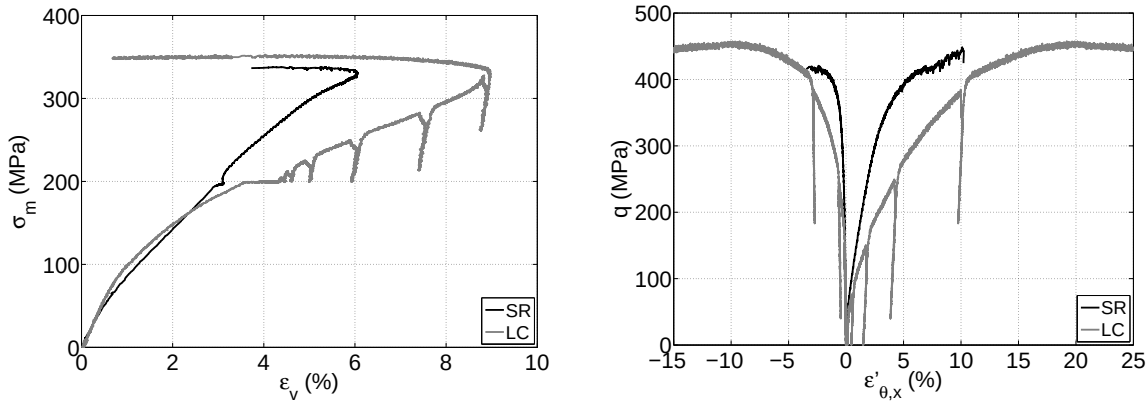

(a) (b)

Figure 12: Essai triaxial à 200 MPa de confinement sur des bétons ayant des granulats siliceux (SR) et des granulats calcaires (LC): (a) contrainte moyenne σ_m vs. déformation volumique ε_v, (b) contrainte déviatorique q vs. déformations ε'_θ and ε'_x

Essai triaxial à 650 MPa de confinement

La Figure 13 présente les résultats d'essais triaxiaux réalisés à 650 MPa de confinement sur les bétons de granulats siliceux et de billes de verre. Ces essais démontrent que la différence de déformation volumique est significative seulement à de faibles niveaux de confinement. Au-delà de 200 MPa de confinement, les raideurs volumiques tangentielles des deux bétons sont presque identiques. Pour une telle valeur de confinement, les différences dans les propriétés élastiques globales sont probablement annulées par la compaction de la matrice de ciment.

Les résultats de la compression triaxiale menée à 650 MPa de confinement sur des bétons avec des granulats siliceux et des granulats de calcaire sont présentés dans la Figure 14. Le béton de granulats calcaires a été chargé hydrostatiquement jusqu'à une pression de 650 MPa. En raison d'un problème technique, la partie triaxiale ultérieure,

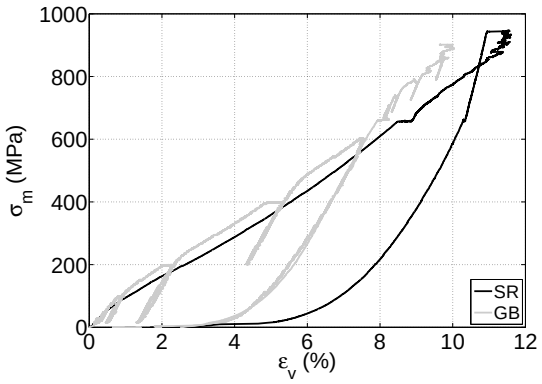

Figure 13: Essai triaxial à 650 MPa de confinement sur des bétons ayant des granulats siliceux (SR) et des billes de verre (GB): contrainte moyenne σ_m vs. déformation volumique ε_v

i.e. après déchargement et rechargement hydrostatique, a été réalisée sous un confinement de 600 MPa. La déformation volumique est beaucoup plus élevée pour les granulats de béton calcaire, une constatation qui peut s'expliquer par la forte porosité de la roche.

La Figure 14(b) montre que la rigidité tangentielle au cours de la phase déviatorique est presque la même pour les deux échantillons. Une grande partie de la porosité du calcaire a probablement été fermée au cours de la partie hydrostatique de chargement, ce qui a raidi les granulats calcaires, dans une plus large mesure que pour le test de 200 MPa. Pour comparer les contraintes maximales déviatoriques qui sont fortement tributaires de la pression de confinement, nous avons analysé un essai effectué sur béton de granulats siliceux roulés à 600 MPa de pression de confinement: la valeur résultante du déviateur des contraintes, 830 MPa, est supérieure à la contrainte déviatorique maximale atteinte par le béton de granulats calcaires (730 MPa).

La composition des granulats influe fortement sur le mode de rupture dans des échantillons de béton à haut confinement. Pour un béton de granulats calcaires, une seule fissure passant à la fois par le mortier et les granulats apparaît, tandis que quelques fissures horizontales le long de granulats principalement décollés sont observés dans le béton de granulats siliceux, ainsi que sur des échantillons de béton de billes de verre.

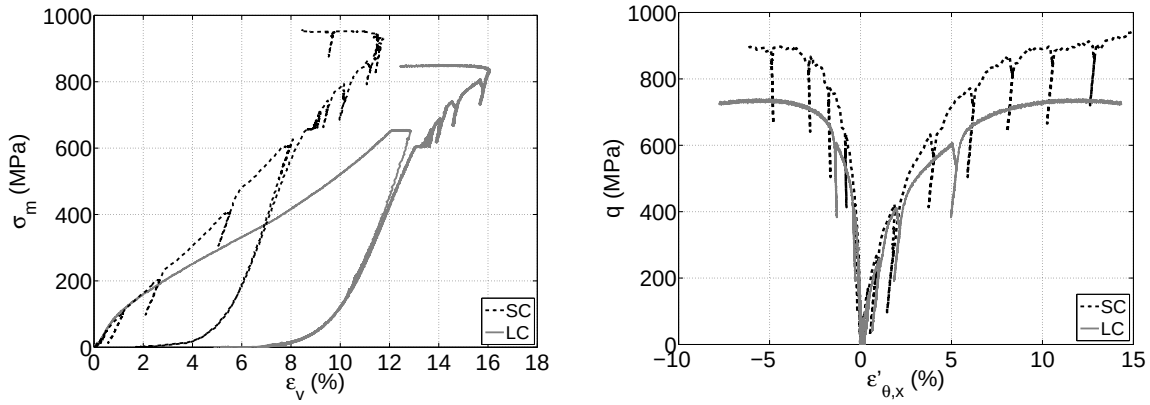

Figure 14: Essai triaxial à 650 MPa de confinement sur des bétons ayant des granulats siliceux (SR) et des granulats calcaires (LC): (a) contrainte moyenne σ_m vs. déformation volumique ε_v, (b) contrainte déviatorique q vs. déformations ε'_θ and ε'_x

Conclusion

Cette étude expérimentale a examiné les effets des granulats sur le comportement du béton sous chargement triaxial sévère. Des essais triaxiaux ont été réalisés à des niveaux de pression de confinement entre 0 et 650 MPa sur quatre bétons ne se distinguant que par le type des gros granulats. Tout d'abord, l'influence de la forme des granulats a été évaluée sur trois bétons contenant des granulats roulés, des granulats concassés et des billes de verre. Ensuite, des bétons à granulats siliceux, calcaires, ou contenant des billes de verre ont été introduits pour étudier l'influence de la composition des granulats. Les bétons avec des formes de granulats similaires ont été comparés par paires: le béton de billes de verre a été comparé au béton de granulats siliceux roulés, puis le béton de granulats siliceux concassés a été comparé avec un béton de granulats concassés calcaires.

La résistance de l'interface granulat/mortier s'est avérée être le principal facteur régissant le comportement du béton dans un essai de compression simple. Ce phénomène est bien connu pour le béton ordinaire, dans lequel la résistance des granulats est beaucoup plus grande que la résistance du mortier. Les granulats de forme irrégulière augmentent légèrement la résistance générée à l'interface granulat/mortier.

À des niveaux de confinement modérés (50 MPa), la résistance au cisaillement du béton est principalement contrôlée par la résistance des granulats, mais dans le même sens que ce qui a été observé pour la compression simple, les granulats angulaires rugueux améliorent la résistance du béton.

À fort confinement ($\geq$ 200 MPa), la résistance au cisaillement de béton semble être contrôlée par la matrice de ciment compacté, à condition que la résistance des granulats soit supérieure à la résistance du mortier. Sinon, un agrégat de moindre résistance réduit la résistance globale du béton à très haut confinement (600 MPa). La forme des granulats ne semble donc pas exercer d'influence sous fort confinement.

Modélisation discrète de béton à la méso-échelle

Le modèle numérique proposé dans ce travail combine une approche DEM cohésive (Delenne *et al.* [20]) avec une approche de type lattice, ce qui signifie que les éléments discrets sont des points matériels appartenant aux différentes phases du béton, au lieu de correspondre à des particules de corps rigides. Une approche 2-D est adoptée pour réduire les temps et coût de calcul.

Comme ce résumé est principalement axé sur les résultats finaux, nous ne présentons ici qu'une brève description du modèle. Le lecteur est invité à lire le corps principal afin d'avoir des informations plus détaillées sur ce chapitre.

Principes de la méthode

Le béton est modélisé comme un matériau composé de granulats, de matrice cimentaire et de vides. L'espace est discrétisé par une grille de points (noeuds) reliés par des éléments ligne (bonds). Différentes méthodes de génération de la grille de noeuds ont été testées. Pour les simulations finales, la grille des noeuds a été construite à partir d'un assemblage granulaire isotrope; les noeuds ont été placés dans les centres de disques. Les liens initiaux connectant les noeuds présentent un caractère cohésif. Chaque liaison peut alors transférer une force normale et une force tangentielle jusqu'à des seuils d'efforts donnés. En cas de rupture, la liaison cohésive est remplacée par un frottement standard. Un élément de ligne peut donc être dans deux états différents, liaison cohésive ou de contact.

Les granulats et les vides sont distribués de manière aléatoire sur la surface de l'échantillon. Les propriétés mécaniques des éléments lignes dépendent du type de noeuds connectés, c'est à dire de leur position dans le milieu à trois phases (Fig. 15). Les noeuds appartenant à la phase des vides sont retirés et les types de liaisons suivantes sont distingués:

- granulat (a): deux noeuds placés dans le même granulat
- matrice (m): deux noeuds placés dans la matrice cimentaire
- interface granulat-matrice (am): un noeud placé dans la matrice et l'autre dans un granulat

Une fois que l'échantillon est discrétisé, le modèle constitué de points matériels connectés par des bonds est soumis à une charge extérieure. L'algorithme de calcul exécuté à chaque intervalle de temps est le suivant:

- Actualisation de la position et la vitesse de chaque noeud
- Application de la loi de contact afin de déterminer les forces d'interaction
- Calcul des accélérations à partir des forces résultantes agissant sur chaque noeud en utilisant la deuxième loi de Newton.

Pour prendre en compte le phénomène de compaction, caractéristique pour des matériaux de matrice cimentaire et correspondant à la fermeture de la porosité, la liste des liaisons est mise à jour au cours de la simulation. Cependant, au lieu de la loi cohésive, une loi de contact habituelle, avec frottement sec, est appliquée aux nouvelles interactions.

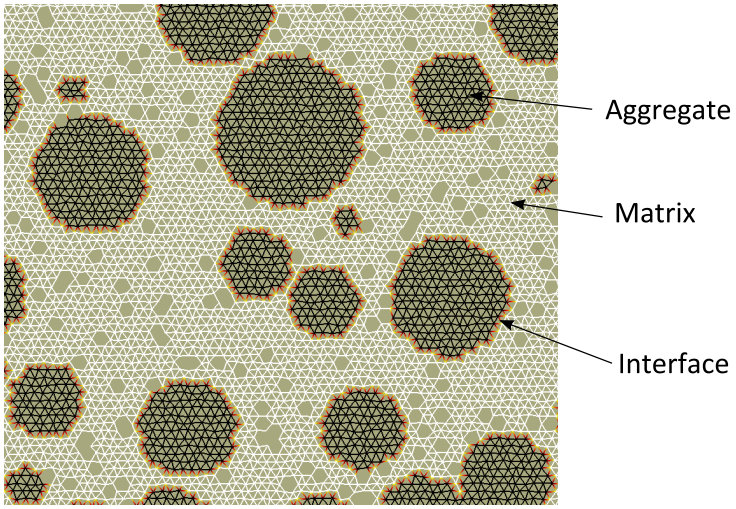

Figure 15: Une représentation d'un milieu à trois phases par un réseau triangulaire

Comportement des éléments

Le matériau est représenté par une grille de noeuds connectés par des liaisons cohésives. Les noeuds peuvent être animés à la fois de mouvements de translation et de rotation. Le déplacement relatif total au niveau de la liaison cohésive est décomposé en une composante normale d_n et une composante tangentielle d_t. Les actions mécaniques correspondantes sont une force normale $\vec{F_n}$ et une force tangentielle $\vec{F_t}$, calculées en utilisant les paramètres de rigidité locales, k_{n_comp}, k_{n_trac} et k_t, correspondant à la phase représentée par la liaison. Par conséquent, les relations force-déplacement sont:

$$F_n = \begin{cases} k_{n\_comp} d_n, & \text{if } d_n \geq 0 \text{ (contraction)} \\ k_{n\_trac} d_n, & \text{if } d_n < 0 \text{ (extension)} \end{cases} \tag{4.10}$$

Dans nos simulations k_{n_comp} and k_{n_trac} ont la même valeur et seront simplement notés k_n.

$$F_t = k_t d_t \tag{4.11}$$

Un critère de rupture locale régit la transition entre un état de cohésion et un état de contact frottant. La rupture peut se produire en traction ou en cisaillement. Le critère est exprimé par une fonction en loi puissance :

$$\zeta = \left| \frac{F_t}{F_t^0} \right|^n + \frac{F_n}{F_n^0} - 1 = 0 \tag{4.12}$$

où F_n^0 and F_t^0 sont respectivement les seuils en force tangentielle et en force normale. L'exposant n contrôle la forme de la courbe $\zeta = 0$ (Fig. 16). En première estimation, il a été fixé à 5.
Un lien cohésif entre deux noeuds est actif pour $\zeta < 0$, autrement la liaison rompt et le contact devient frictionnel sans cohésion. La même loi de contact est utilisée pour les contacts proviennent de la rupture d'une liaison cohésive et pour les "nouveaux contacts",

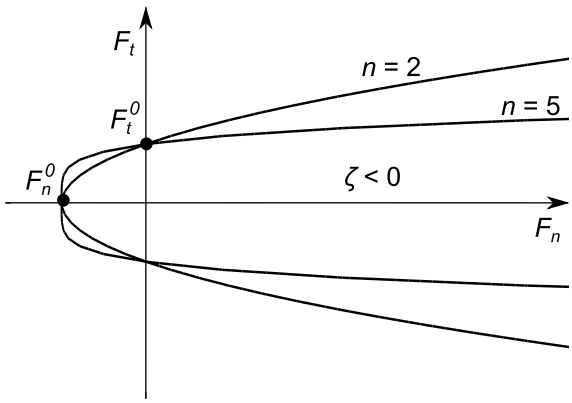

Figure 16: Critère de rupture des interactions cohésifs

n'existant pas auparavant sous forme de liasons cohésives, mais détectés au cours de la simulation. Une loi élastique linéaire est utilisée pour décrire l'interaction normale de contact:

$$F_n = \begin{cases} k_n d_n, & \text{if } d_n \geq 0 \\ 0, & \text{if } d_n < 0 \end{cases} \tag{4.13}$$

avec la rigidité normale du contact k_n.

La composante tangentielle de la force de contact est déterminée en utilisant une formulation élastique-plastique. La force est incrémentée à chaque pas de temps i en utilisant la raideur de contact tangentielle k_t, la vitesse de glissement par rapport au point de contact v_t, et la valeur de l'incrément de temps Δt:

$$F_t^i = F_t^{i-1} + k_t v_t \Delta t \tag{4.14}$$

Le seuil plastique est imposée par le critère de Coulomb:

$$|F_t| \leq \mu F_n \tag{4.15}$$

où μ est le coefficient de frottement.

Intégration du mouvement

Pour décrire l'évolution du système, les positions et les vitesses de chaque nœud sont mises à jour à chaque pas de temps en intégrant la deuxième loi de Newton (4.16), une fois que les forces résultantes sont connues.

$$m_i \frac{d^2 \vec{x}_i}{dt^2} = \vec{F}_i, \qquad i = 1, ..., N \tag{4.16}$$

où N est le nombre de noeuds, m_i est la masse du noeud i, $\vec{x}_i$ est sa position, et $\vec{F}_i$ est la force résultante agissant sur ce noeud.

Afin de calculer les nouvelles positions, vitesses et accélérations des noeuds, un algorithme explicite, nommé Velocity Verlet, est utilisé.

Il est supposé que les forces de contact sont exercées au niveau des points de contact, P_i et P_j. Cela implique une existence d'un couple agissant sur les deux noeuds. Ces couples modifient les vitesses angulaires des noeuds. Ainsi, il est nécessaire d'ajouter à l'équation 4.16 les équations pour les coordonnées angulaires des grains:

$$I_i \frac{d\vec{\omega}_i}{dt} = \vec{\Gamma}_{ij} \tag{4.17}$$

où I_i est le moment d'inertie du noeud i.

Certains autres aspects informatiques, tels que le choix du pas de temps, l'amortissement numérique et l'application des conditions aux limites, ainsi qu'une procédure utilisée pour déterminer les paramètres du modèle peuvent être trouvés dans le 3e chapitre du manuscrit.

Conclusion

Un modèle mésoscopique 2D de béton a été développé dans le cadre de la méthode des éléments discrets. Le modèle a été conçu pour combiner des lois d'interaction simples avec l'hétérogénéité du matériau au niveau mésoscopique. Par conséquent, deux types d'interactions sont utilisées dans le modèle : des liens cohésifs, dont le comportement est décrit par une loi élastique linéaire fragile, et des contacts frottants détectés au cours de la simulation, avec la loi de frottement de Coulomb. Ces derniers sont soit des liaisons cohésives cassées ou des nouveaux contacts. D'autre part, trois phases décrites avec différents paramètres mécaniques sont présentes dans un échantillon de béton: matrice, granulats et interface. En outre, la mésostructure d'un échantillon est modifiée par l'introduction des vides dans la phase de matrice.

Après les premiers efforts d'étalonnage, le modèle a été utilisé pour simuler le comportement biaxial de béton à différents niveaux de confinement. Deux résultats importants, qui ne sont pas développés ici, ont été obtenus avec cette méthode simple:

- on retrouve une augmentation de la résistance, et l'apparition d'un plateau de contraintes à la place d'un pic de contraintes, lors de l'augmentation de la pression de confinement

- on a pu simuler un comportement fortement non linéaire en compression isotrope grâce à la présence de vides.

Certaines applications du modèle

Influence de la structure des vides

Une des particularités du modèle est la prise en compte des vides comme une entité mésostructurale. Dans cette section, nous examinons comment les propriétés des vides influencent la réponse d'un échantillon numérique. Une étude de sensibilité est effectuée sur des échantillons numériques constitués d'une seule phase - mortier, pour évaluer l'effet des deux paramètres suivants:

- l'indice, ou taux, des vides ϕ - exprimé à partir du nombre de liaisons retirées de l'échantillon divisé par le nombre initial de liaisons,
- la taille des vides d^* - exprimé comme le rapport du diamètre moyen de vide $< d_{void} >$ par rapport au diamètre moyen des particules discrètes dans un échantillon d_{mean}.

Une distribution normale des tailles de vide est utilisée avec une valeur moyenne égale à $< d_{void} >$ et un écart-type égal à $0.5 d_{mean}$.

La Figure 17 montre l'évolution de la raideur volumique initiale en fonction de ϕ et d^*. Le module initial de chaque échantillon testé est comparé au module initial de l'échantillon non poreux. On peut observer que la raideur élastique est fortement influencée par le volume des vides dans un échantillon: la rigidité diminue à mesure que la porosité augmente. D'autre part, la taille des vides n'a que peu d'effet sur la rigidité volumique initiale.

L'effet du taux de vides pour une taille de vides donnée ($d^* = 3$) est plus précisément illustré dans la Figure 18 représentant la contrainte moyenne σ_m en fonction de la déformation volumique ε_v. L'augmentation de la porosité induit des déformations volumiques plus élevées. Dans l'échantillon non poreux, on observe une augmentation monotone, quasi-linéaire du module de compressibilité tangent. Cette rigidification est dûe à des contacts nouvellement créés lors du chargement. À la fin de l'essai, le nombre d'interactions dans un échantillon a augmenté d'environ 15%. Lorsque les vides sont introduits dans un échantillon, on observe d'abord une réduction de la raideur volumétrique. Elle est suivie par une augmentation du module tangent. La réduction de la rigidité provient de la présence des vides et est commandé par leurs propriétés. Il est intéressant de noter que ceci résulte directement de la prise en compte d'une méso-échelle contenant des vides. Aucun paramètre n'a été utilisé pour "contrôler" la courbe macroscopique, à l'exception de la répartition des vides à l'intérieur de la phase de mortier. C'est un atout du modèle: les caractéristiques macroscopiques résultent de la géométrie à la méso-échelle et des propriétés mécaniques de base. Les résultats présentés dans la Figure 19 indique que la courbure de la courbe contrainte-déformation au niveau des contraintes faibles et moyennes est plus affectée par la taille des vides que par la fraction en volume de vides. La réduction de la raideur volumique est plus marquée pour les échantillons avec de grands pores ($d^* = 3$ et $d^* = 5$) que pour l'échantillon avec de petits pores ($d^* = 1$), en dépit d'une fraction volumique de vides inférieure.

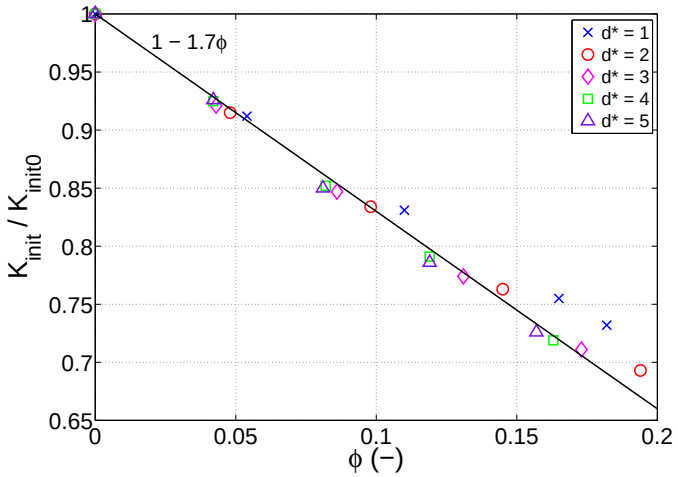

Figure 17: Module de compressibilité initial K_{init} par rapport au module initial de l'échantillon non poreux K_{init0}, en fonction du taux de vides ϕ, pour différentes tailles de vide d^*

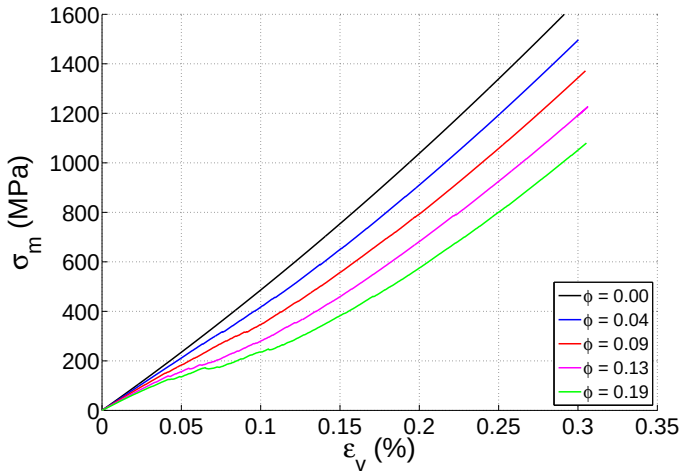

Figure 18: Compression isotrope menée sur des échantillons avec différents indices des vides ϕ et avec une dimension de vide d^* égal à 3: contrainte moyenne σ_m vs. déformation volumique ε_v

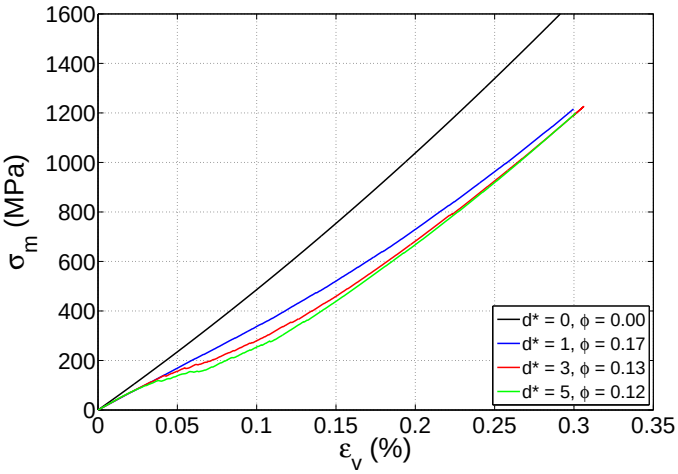

Figure 19: Compression isotrope menée sur des échantillons avec différents indices des vides ϕ et différentes tailles de vide d^*: contrainte moyenne σ_m vs. déformation volumique ε_v

Pour décrire la courbure de la courbe contrainte-déformation, S est défini comme le rapport de la valeur maximale sur la valeur minimale du module tangent (voir Fig. 20):

$$S = \frac{K_{max}}{K_{min}} \tag{4.18}$$

S est supérieur à 1 et augmente pour les courbures les plus prononcées. La Figure 21 affiche une carte en couleur correspondant à la valeur de S en fonction du taux de vide ϕ et la taille de vide d^*, interpolée à partir de 20 tests effectués. Une couleur noire correspond à la valeur minimale de S, obtenue pour l'échantillon non poreux. On observe à nouveau qu'à la fois le taux de vides, et la taille des vides, influencent la courbure de la courbe hydrostatique; la fonction $S(\phi, d^*)$ décline quasi-linéairement. Il est intéressant de noter que pour les indices des vides élevés, la présence de petits pores n'affecte pas sensiblement la forme de la courbe contrainte-déformation. D'autre part, les grands vides semblent réduire fortement la raideur volumétrique, même à des taux de pores inférieurs.

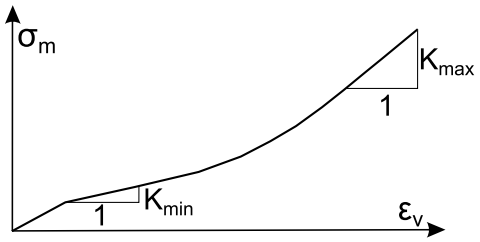

Figure 20: Croquis montrant les modules tangents K_{min} et K_{max} utilisés dans la définition du paramètre de courbure S

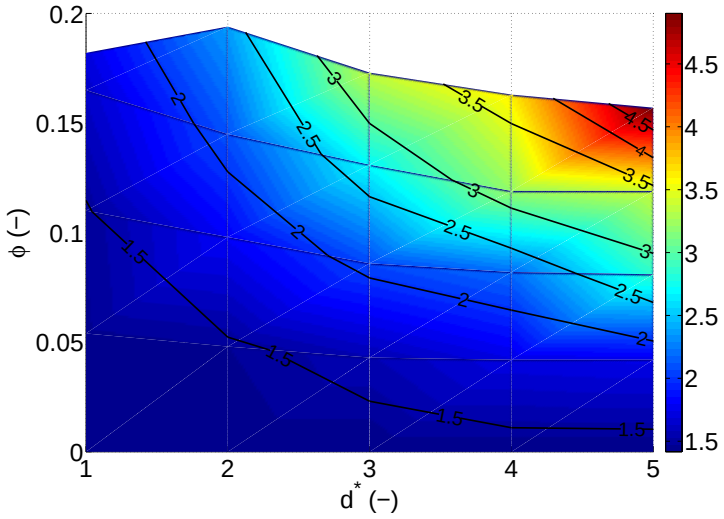

Figure 21: Carte en couleur représentant l'évolution du paramètre de courbure S en fonction du taux de vide ϕ et de la taille des vides d^*

Influence des propriétés de granulats et de l'interface à très faible confinement

L'influence des paramètres mécaniques correspondant à la phase des granulats et à l'interface granulats/mortier est étudiée sur un échantillon numérique composée de 6784 particules reliées par 16643 éléments ligne. Les granulats sphériques sont distribués au hasard sur l'échantillon. Les pourcentages de liens représentant le mortier, les granulats et l'interface sont répertoriés dans le Tableau 2.

Type déléments	**Pourcentage**
Mortier	55%
Granulats	38%
Interface	7%

Table 2: Pourcentage des différents types d'éléments ligne dans un échantillon de béton

Grâce à une nature simple du modèle, le nombre de paramètres décrivant le comportement mécanique des phases matérielles est très limité. Chaque phase est caractérisée par des paramètres de rigidité k_n et k_t, des seuils de cohésion F_n^0 and F_t^0, décrivant les liens cohésifs, et un coefficient de frottement μ, utilisé pour les contacts.

Dans tous les essais présentés dans cette section, les valeurs relatives des paramètres de rigidité sont les suivants :

$$\frac{k_n^a}{k_n^m} = \frac{k_t^a}{k_t^m} = 3 \tag{4.19}$$

$$\frac{k_n^{am}}{k_n^m} = \frac{k_t^{am}}{k_t^m} = 1 \tag{4.20}$$

En ce qui concerne le seuil cohésif, nous définissons un échantillon de référence comme suit:

$$\frac{F_n^{0a}}{F_n^{0m}} = \frac{F_t^{0a}}{F_t^{0m}} = 3 \tag{4.21}$$

$$\frac{F_n^{0am}}{F_n^{0m}} = \frac{F_t^{0am}}{F_t^{0m}} = 0.2 \tag{4.22}$$

Bien qu'il soit très difficile de déduire les paramètres du modèle microscopique d'expériences réalisées sur le béton ou sur les constituants du béton, les données expérimentales disponibles peuvent être utilisées comme un indicateur pour caractériser le modèle. Le Tableau 3 rappelle les valeurs de résistance uniaxiale du béton, du mortier et des granulats, obtenues à partir d'expériences. La résistance à la traction du mortier a été estimée à partir d'essais de flexion 3 points, celle des granulats suite à des tests de traction par fendage, et celle du béton a été mesurée à partir d'essais de traction directe.

Matériau	**Mortier**	**Granulats siliceux**	**Béton**
σ_c [MPa]	60	330	42
σ_t [MPa]	9	23	3.6

Table 3: Résistance uniaxiale du béton et de ses constituants mésoscopiques [29, 22, 48]

La zone de transition interfaciale (ITZ) entre la pâte de ciment et les granulats (matrice de ciment et granulats de grande taille à l'échelle mésoscopique), est bien connue comme étant un maillon faible dans le béton. Dans l'échantillon de référence, sa résistance a été fixée arbitrairement à 20% de la résistance du mortier. D'ailleurs, dans toutes les phases, les seuils de rupture normale et tangentielle sont égaux, ce qui est une simplification adoptée dans une première tentative.

Le premier objectif de cette étude préliminaire est d'analyser le comportement du modèle en fonction des granulats et des propriétés de l'interface et de saisir les grandes tendances. Une comparaison directe avec des expériences serait une tâche beaucoup plus difficile, en particulier parce que, expérimentalement, il n'est pas possible de contrôler les différentes propriétés de l'interface séparément.

Dans cette section, nous examinons l'effet des seuils cohésifs et de l'interface sur le comportement du béton. Ces paramètres correspondent aux résistances des granulats et de l'interface à l'échelle macroscopique.

Nous nous sommes intéressés au comportement de l'échantillon numérique sous 1 MPa de pression de confinement. Le confinement a été appliqué pour des raisons techniques, mais sa très faible valeur permet de comparer, de manière qualitative, les résultats numériques avec les observations des essais de compression simples effectués sur le béton.

La réponse de l'échantillon de référence est présentée dans la figure 22(a). Cette figure montre également une comparaison des courbes contrainte-déformation pour la matrice, les granulats et le béton. Un comportement élastique quasi-linéaire suivie d'une rupture soudaine est observé pour les échantillons homogènes de matrice et de granulats. Dans un échantillon composite en béton, une réduction de la rigidité avant le pic de contraintes est trouvée en dépit du caractère élastique-fragile du modèle. Ce phénomène est donc

dû à l'hétérogénéité du matériau et, comme dans un vrai spécimen de béton, vient des microfissures multiples, surtout dans l'ITZ. La Figure 22(b) montre l'évolution des liens rompus dans l'échantillon de béton de référence, dans ses trois phases: la matrice, les aggrégats et l'interface. Les dommages apparaissent d'abord à l'interface granulats / mortier et continue à se développer dans le mortier, entre les granulats. Les granulats ne se cassent pas alors que le déplacement axial augmente. À un certain moment, l'échantillon subit une rupture fragile caractérisée par plusieurs fissures quasi-verticales autour des granulats. La Figure 23 montre l'échantillon à la fin de l'essai. Les points verts marquent les liens cohésifs brisés. Ce mode de rupture, caractérisé par un décollement total, est typique pour le béton ordinaire, fait de granulats considérablement plus résistants que le mortier, lors de tests en compression uniaxiale.

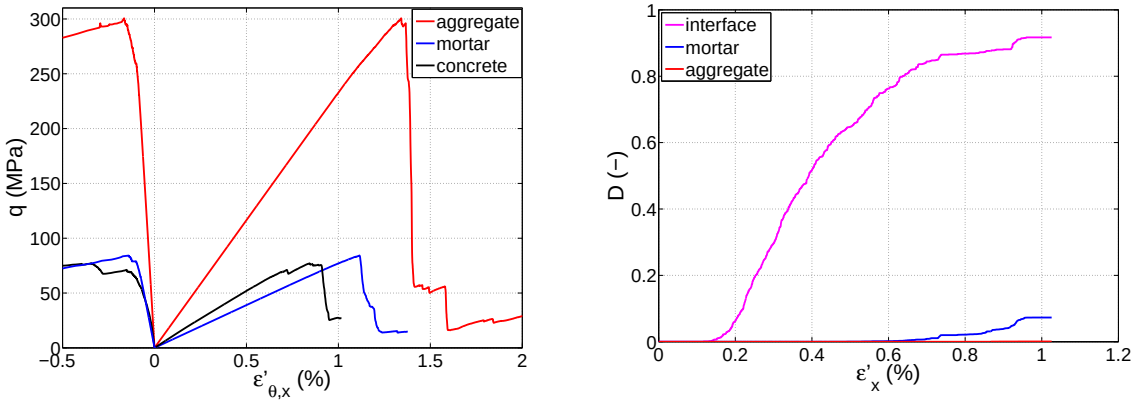

(a) (b)

Figure 22: Compression biaxiale à 1 MPa de confinement
(a) comportements du béton de référence ($F^{0a}/F^{0m} = 3$, $F^{0am}/F^{0m} = 0.2$), du mortier et des granulats: déviateur q vs. déformations ε'_θ and ε'_x
(b) évolution du paramètre d'endommagement D vs. déformation axiale ε'_x dans l'échantillon de béton de référence

Plusieurs tests ont été effectués en utilisant différentes propriétés de rupture de granulats F^{0a} et d'interface F^{0am}. Afin d'analyser l'influence de ces deux paramètres séparément, les tests suivants sont détaillés:

- S1: $\frac{F^{0a}}{F^{0m}} = 3$, $\frac{F^{0am}}{F^{0m}} = 0.2$ (échantillon de référence)
- S2: $\frac{F^{0a}}{F^{0m}} = \mathbf{9}$, $\frac{F^{0am}}{F^{0m}} = 0.2$
- S3: $\frac{F^{0a}}{F^{0m}} = \mathbf{1}$, $\frac{F^{0am}}{F^{0m}} = 0.2$
- S4: $\frac{F^{0a}}{F^{0m}} = 3$, $\frac{F^{0am}}{F^{0m}} = \mathbf{1}$
- S5: $\frac{F^{0a}}{F^{0m}} = 3$, $\frac{F^{0am}}{F^{0m}} = \mathbf{0.05}$

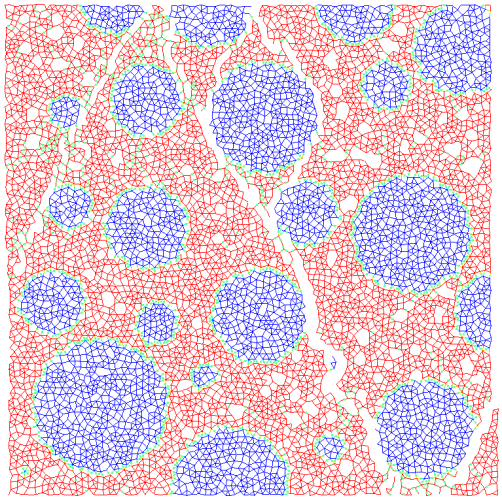

Figure 23: Faciès de fissuration à 1 MPa de confinement dans l'échantillon de béton de référence: $F^{0a}/F^{0m} = 3$, $F^{0am}/F^{0m} = 0.2$

La Figure 24 montre les courbes contrainte-déformation obtenues pour ces cinq échantillons numériques. Le graphe de gauche montre les différences de contraintes maximales dues à des seuils cohésifs différents dans les phases de granulats, à droite il s'agit de l'influence de différents seuils de cohésion de l'interface. Ces deux paramètres influencent la valeur maximale de contrainte, mais dans le cadre de notre étude, les différences de résistance du béton par rapport à l'échantillon de référence sont généralement assez limitées (jusqu'à 20%).

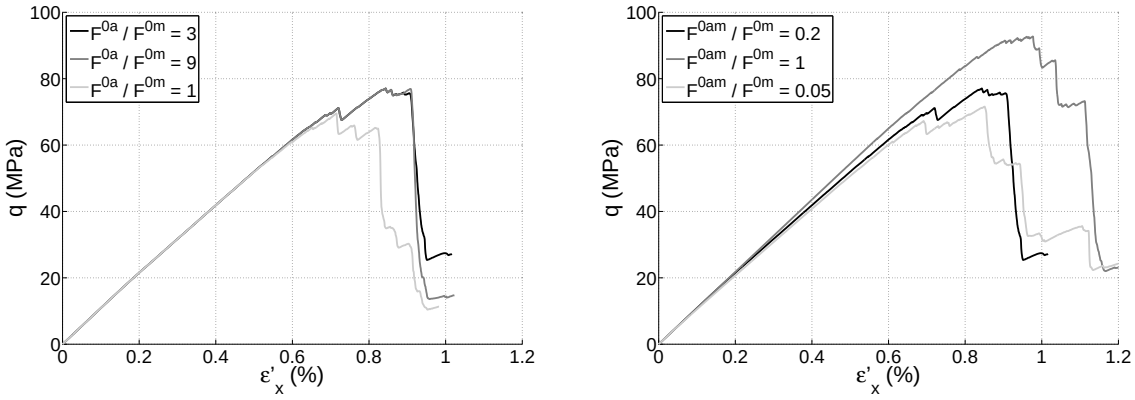

(a) (b)

Figure 24: Influence des résistances (a) de granulats et (b) de l'interface sur le comportement du béton à 1 MPa de confinement: déviateur q vs. déformations ε'_θ and ε'_x

Comme aucun des granulats n'est brisé dans l'échantillon de référence, l'augmentaion des seuils de cohésion dans l'échantillon S2 n'influence pas les résultats. En revanche, la contrainte à la rupture élevée attribuée aux interfaces de l'échantillon S4 augmente

considérablement la résistance de l'échantillon. Les fissures macroscopiques entourent de grands granulats mais ont aussi tendance à passer dans la matrice entre les granulats (voir Fig. 25).

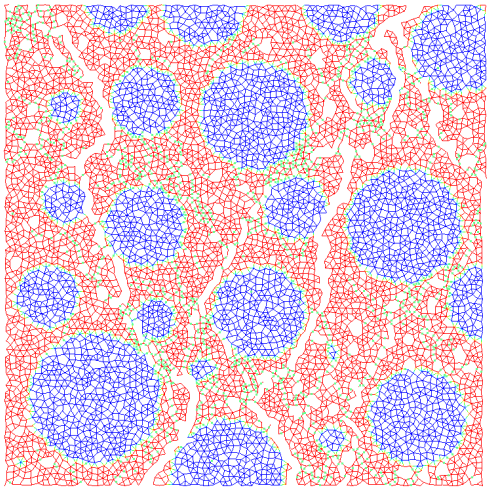

Figure 25: Faciès de fissuration à 1 MPa de confinement dans l'échantillon de béton avec une résistance de l'interface élevée: $F^{0am}/F^{0m} = 1$

L'affaiblissement des granulats et de l'interface réduit la contrainte maximale. L'évolution de l'endommagement de l'échantillon avec un seuil de cohésion réduit (S3) est présenté dans la Figure 26. En effet, une partie des liens correspondants aux granulats est cassée mais les dégâts sont encore principalement concentrés au niveau de l'interface.

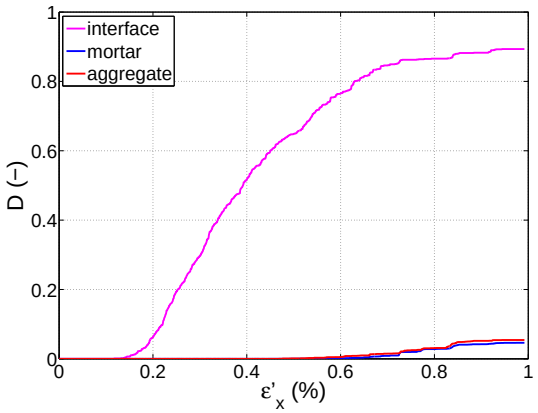

Figure 26: Évolution du paramètre d'endommagement D avec la déformation axiale ε'_x sous 1 MPa de confinement dans l'échantillon de béton avec une faible résistance de granulats: $F^{0a}/F^{0m} = 1$

Résumons maintenant l'ensemble des résultats de tests effectués sous très faible confinement. Certaines valeurs ont été étudiées bien qu'elles ne soient pas réalistes pour le

béton. La Figure 27 affiche une carte de niveaux de gris représentant la résistance des échantillons numériques, en fonction des seuils cohésifs à la fois globaux et d'interface. L'intensité du niveau de gris est proportionnelle à la résistance; une couleur blanche correspond à la plus haute contrainte maximale. Une forte dépendance de la résistance du béton par rapport à la résistance de l'interface est observée. La résistance des granulats affecte la résistance du béton si les granulats sont relativement faibles par rapport au mortier. Pour de grands rapports F^{0a}/F^{0m}, une augmentation ultérieure de la résistance des aggrégats n'affecte pas la contrainte maximale déviatorique.
Ces différentes combinaisons de granulats et de résistance d'interface entraîne différents modes de rupture. Six modes de rupture différents, illustrés schématiquement à la Figure 28, ont été observés.

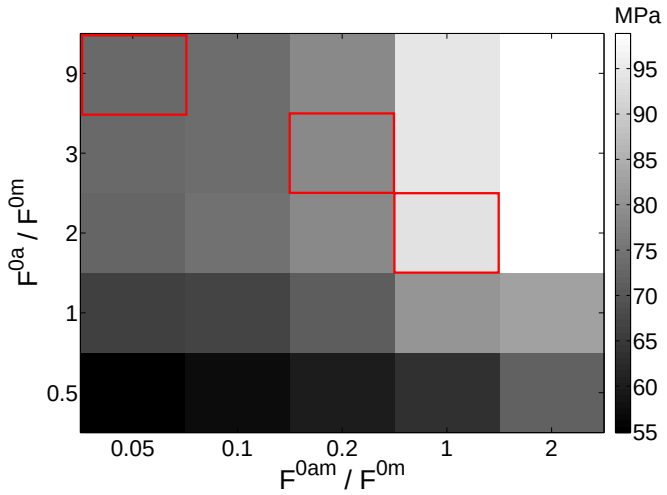

Figure 27: Carte de niveaux de gris représentant le déviateur maximum sous 1 MPa de confinement, en fonction des différentes propriétés de granulats et d'interface

Nous nous sommes concentrés sur trois jeux de paramètres (les valeurs de contraintes maximales correspondantes sont marquées avec des carrés rouges dans la Figure 27):

- $\frac{F^{0a}}{F^{0m}} = 3$, $\frac{F^{0am}}{F^{0m}} = 0.2$ (échantillon de ref.) - pouvant être désigné comme présentant des granulats résistants et une interface normale,
- $\frac{F^{0a}}{F^{0m}} = 9$, $\frac{F^{0am}}{F^{0m}} = 0.05$ - granulats très résistants et interface faible,
- $\frac{F^{0a}}{F^{0m}} = 2$, $\frac{F^{0am}}{F^{0m}} = 1$ - granulats faibles et interface résistante.

Ces trois ensembles de paramètres correspondraient dans notre étude expérimentale respectivement au béton de granulats siliceux, au béton de billes de verre et au béton de granulats calcaires. L'évolution de la contrainte maximale pour ces trois échantillons est conforme aux résultats expérimentaux: la plus grande résistance en compression simple a été trouvée pour le béton à granulats calcaires, la plus basse pour le béton de billes de verre. Les modes de rupture obtenus expérimentalement sont également reproduits par le modèle. Comme mentionné ci-dessus pour l'échantillon de référence, lorsque la

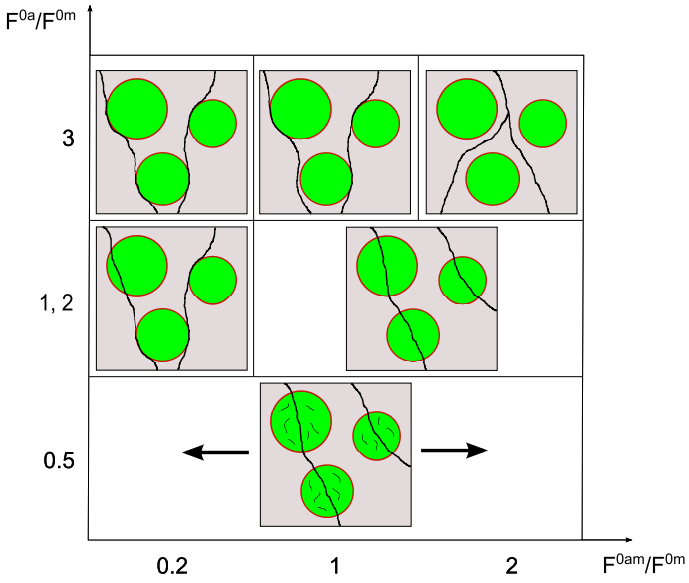

Figure 28: Croquis des modes de rupture sous 1 MPa de confinement dans des échantillons numériques avec différentes propriétés de granulats et d'interface

résistance des granulats est beaucoup plus élevée, mais la résistance de l'interface nettement inférieure à celle du mortier, des fissures entourent les granulats. Ce fut le cas du béton de granulats siliceux mais aussi du béton à billes de verre. Dans l'échantillon avec de faibles aggrégats ($F^{0a}/F^{0m} = 2$) et une l'interface solide ($F^{0a0}/F^{0m} = 1$), les fissures traversent les granulats (Fig. 29). Ce mode de rupture a été à son tour observé pour le béton de granulats calcaires.

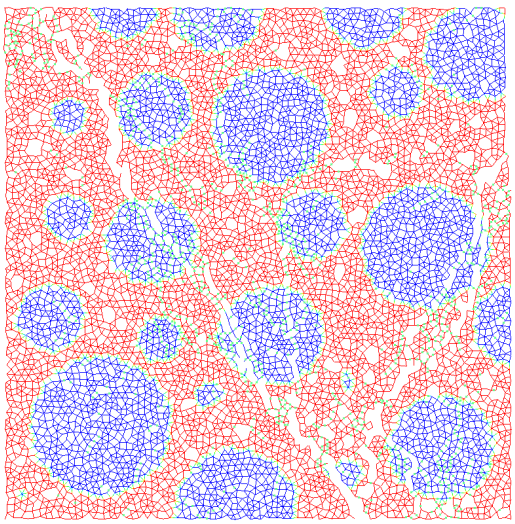

Figure 29: Faciès de fissuration sous 1 MPa de confinement dans l'échantillon avec une faible résistance de granulats: $F^{0a}/F^{0m} = 2$, et une résistance élevée de l'interface: $F^{0am}/F^{0m} = 1$

Conclusion

Un modèle mésoscopique discret de béton a été utilisé pour étudier le comportement du béton en compression confinée. Plus spécifiquement, l'influence des hétérogénéités à grande échelle du béton sur le comportement du modèle a été étudié.

La première partie, concernant l'influence de la porosité, a révélé de nouveaux résultats : il est en effet possible de reproduire le processus de compactage non linéaire du mortier à l'aide d'une loi d'interaction linéaire. Ce comportement de compactage est dépendant de la porosité mais aussi beaucoup de la taille des vides. Cette question doit être étudiée plus profondément, afin d'établir un lien valable entre le comportement d'un véritable béton et un spécimen numérique poreux, mais le résultat obtenu dans cette première étude est très prometteur.

La deuxième partie est axée sur l'effet de la résistance des granulats et de l'interface sur le comportement du béton à différents niveaux de confinement. Quelques résultats expérimentaux décrits précédemment, suite à des des tests triaxiaux réalisés sur des bétons fabriqués avec différents types de granulats ont été brièvement rappelés, et une comparaison qualitative avec le modèle a été faite. Le comportement du modèle à très faible confinement est cohérent avec les observations expérimentales. Le rôle important de la résistance de l'interface granulats / mortier dans la résistance du béton a été observé et les différents modes de rupture observés dans les échantillons de béton sous compression uniaxiale ont été bien reproduits.
L'enquête sous fort confinement a rencontré plus de difficultés et n'a donc pas été mentionnée dans ce résumé.

Bibliography

[1] Schott technical glasses physical and technical properties. Tech. rep., SCHOTT, 2010.

[2] Aitcin, P., and Mehta, P. Effect of coarse aggregate characteristics on mechanical properties of high-strength concrete. *ACI Materials Journal 87*, 2 (1990).

[3] Akers, S., and Phillips, B. Concrete modelled as un inhomogeneous material: numerical simulations of contact detonation charges. In *18th International Symposium on the Military Aspects of Blast and Schock* (Bad Reichenhall, Germany, 2004).

[4] Berthet-Rambaud, P., Limam, A., Roenelle, P., Rapin, F., Tacnet, J.-M., and Mazars, J. Avalanche action on rigid structures: Back-analysis of taconnaz deflective walls' collapse in february 1999. *Cold Regions Science and Technology 47*, 12 (2007), 16 – 31.

[5] Beshr, H., Almusallam, A., and Maslehuddin, M. Effect of coarse aggregate quality on the mechanical properties of high strength concrete. *Construction and Building Materials 17*, 2 (2003), 97–103.

[6] Burlion, N. *Compaction des bétons: éléments de modélisation et caractérisation expérimentale*. PhD thesis, ENS Cachan, France, 1997.

[7] Burlion, N., Bernard, D., and Chen, D. X-ray microtomography: Application to microstructure analysis of a cementitious material during leaching process. *Cement and Concrete Research 36*, 2 (2006), 346–357.

[8] Buzaud, E. High pressure triaxial compression of concrete. In *In Workshop High Target Research, QinetiQ* (Farnborough, UK, 2004).

[9] Caballero, A., Carol, I., and López, C. M. A meso-level approach to the 3D numerical analysis of cracking and fracture of concrete materials. *Fatigue and Fracture of Engineering Materials and Structures 29*, 12 (2006), 979–991.

[10] Caballero, A., López, C., and Carol, I. 3D meso-structural analysis of concrete specimens under uniaxial tension. *Computer Methods in Applied Mechanics and Engineering 195*, 52 (2006), 7182–7195.

[11] Castellote, M., Alonso, C., Andrade, C., Turrillas, X., and Campo, J. Composition and microstructural changes of cement pastes upon heating, as studied by neutron diffraction. *Cement and Concrete Research 34*, 9 (2004), 1633–1644.

[12] Combe, G. *Origines géométriques du comportement quasi-statique des assemblages granulaires denses: étude par simulations numériques.* PhD thesis, école Nationale des Ponts et Chaussées, Champs-sur-Marne, France, 2001.

[13] Combe, G., and Roux, J.-N. Construction of granular assemblies under static loading. In *Discrete-element Modeling of Granular Materials*, Radja Ed. pp. 153–180.

[14] Comby-Peyrot, I., Bernard, F., Bouchard, P.-O., Bay, F., and Garcia-Diaz, E. Development and validation of a 3D computational tool to describe concrete behaviour at mesoscale. application to the alkali-silica reaction. *Computational Materials Science 46*, 4 (2009), 1163–1177.

[15] Cundall, P. Distinct element models of rock and soil structure. *Analytical and Computational Methods in Engineering Rock Mechanics 4* (1987), 129–163.

[16] Cundall, P. A., and Strack, O. D. L. *Gotechnique 29*, 1 (1979), 47–65.

[17] Cusatis, G., Mencarelli, A., Pelessone, D., and Baylot, J. Lattice Discrete Particle Model (LDPM) for failure behavior of concrete. II: Calibration and validation. *Cement and Concrete Composites 33*, 9 (2011), 891–905.

[18] Cusatis, G., Pelessone, D., and Mencarelli, A. Lattice Discrete Particle Model (LDPM) for failure behavior of concrete. I: Theory. *Cement and Concrete Composites 33*, 9 (2011), 881–890.

[19] de Larrard, F., and Belloc, A. The influence of aggregate on the compressive strength of normal and high-strength concrete. *ACI materials journal 94*, 5, 417–426.

[20] Delenne, J.-Y., El Youssoufi, M. S., Cherblanc, F., and Bnet, J.-C. Mechanical behaviour and failure of cohesive granular materials. *International Journal for Numerical and Analytical Methods in Geomechanics 28*, 15 (2004), 1577–1594.

[21] Du, M., Gao, P., and Chen, F. J. The impact of aggregates distribution on concrete failure. *Advanced Materials Research 594* (2012), 929–932.

[22] Dupray, F. *Comportement du béton sous fort confinement: étude en compression et en extension triaxiales à l'échelle mésoscopique.* PhD thesis, Université Joseph Fourier, Grenoble, France, 2008.

[23] Dupray, F., Malécot, Y., Daudeville, L., and Buzaud, E. A mesoscopic model for the behaviour of concrete under high confinement. *International Journal for Numerical and Analytical Methods in Geomechanics 33*, 11 (2009), 1407–1423.

[24] Elaqra, H., Godin, N., Peix, G., R'Mili, M., and Fantozzi, G. Damage evolution analysis in mortar, during compressive loading using acoustic emission and X-ray tomography: Effects of the sand/cement ratio. *Cement and Concrete Research 37*, 5 (2007), 703–713.

[25] Erdogan, S., Quiroga, P., Fowler, D., Saleh, H., Livingston, R., Garboczi, E., Ketcham, P., Hagedorn, J., and Satterfield, S. Three-dimensional shape analysis of coarse aggregates: New techniques for and preliminary results on several different coarse aggregates and reference rocks. *Cement and Concrete Research 36*, 9 (2006), 1619–1627.

[26] Erzar, B., and Forquin, P. Experiments and mesoscopic modelling of dynamic testing of concrete. *Mechanics of Materials 43*, 9 (2011), 505 – 527.

[27] Ezeldin, A., and Aitcin, P. Effect of coarse aggregate on the behavior of normal and high-strength concretes. *Cement, Concrete and Aggregates 13*, 2 (1991).

[28] Forquin, P., Safa, K., and Gary, G. Influence of free water on the quasi-static and dynamic strength of concrete in confined compression tests. *Cement and Concrete Research 40*, 2 (2010), 321–333.

[29] Gabet, T. *Comportement triaxial du béton sous fortes contraintes : Influence du trajet de chargement*. PhD thesis, Université Joseph Fourier, Grenoble, France, 2006.

[30] Gabet, T., Malécot, Y., and Daudeville, L. Triaxial behaviour of concrete under high stresses: Influence of the loading path on compaction and limit states. *Cement and Concrete Research 38*, 3 (2008), 403–412.

[31] Garboczi, E. Three-dimensional mathematical analysis of particle shape using X-ray tomography and spherical harmonics: Application to aggregates used in concrete. *Cement and Concrete Research 32*, 10 (2002), 1621–1638.

[32] GDR MiDi. On dense granular flows. *The European Physical Journal E 14* (2004), 341–365.

[33] Giaccio, G., and Zerbino, R. Failure mechanism of concrete: Combined effects of coarse aggregates and strength level. *Advanced Cement Based Materials 7*, 2 (1998), 41–48.

[34] Groupe de travail Durabilité des bétons (France), and Laboratoire Matériaux et durabilité des constructions (Toulouse). *Compte-rendu Des Journees Techniques AFPC-AFREM, Durabilité Des Bétons: Méthodes Recommandées Pour la Mesure Des Grandeurs Associées à la Durabilité : 11 Et 12 Décembre 1997, Toulouse*. INSA, 1998.

[35] Iwashita, K., and Oda, M. Rolling resistance at contacts in simulation of shear band development by DEM. *Journal of Engineering Mechanics 124*, 3 (1998), 285–292.

[36] Jamet, P., Millard, A., and Nahas, G. Triaxial behaviour of a micro-concrete complete stress-strain for confining pressures ranging from 0 to 100 MPa. In *Proc. of Int. Conf. on Concrete under Multiaxial Conditions* (1984), vol. 1, pp. 133–140.

[37] Johnson, K. *Contact Mechanics*. Cambridge University Press, 1985.

[38] Landis, E. N., Nagy, E. N., and Keane, D. T. Microstructure and fracture in three dimensions. *Engineering Fracture Mechanics 70*, 7 (2003), 911–925.

[39] Lilliu, G., and van Mier, J. G. 3D lattice type fracture model for concrete. *Engineering Fracture Mechanics 70*, 7 (2003), 927–941.

[40] Lu, S., Landis, E., and Keane, D. X-ray microtomographic studies of pore structure and permeability in portland cement concrete. *Materials and Structures 39*, 6 (2006), 611–620.

[41] Mazars, J. A description of micro-and macroscale damage of concrete structures. *Engineering Fracture Mechanics 25*, 5 (1986), 729–737.

[42] Moës, N., Dolbow, J., and Belytschko, T. A finite element method for crack growth without remeshing. *International Journal for Numerical Methods in Engineering 46* (1999), 131–150.

[43] Monteiro, P., and Mehta, P. Interaction between carbonate rock and cement paste. *Cement and Concrete Research 16*, 2 (1986), 127–134.

[44] Monteiro Azevedo, N., Lemos, J., and de Almeida, J. R. Influence of aggregate deformation and contact behaviour on discrete particle modelling of fracture of concrete. *Engineering Fracture Mechanics 75*, 6 (2008), 1569–1586.

[45] Moreau, J. J. Numerical Investigation of Shear Zones in Granular Materials. In *Friction, Arching and Contact Dynamics* (Singapore, 1997), D. E. Wolf and P. Grassberger, Eds., World Scientific.

[46] Neville, A. *Properties of Concrete*. Pearson Education Canada, 2011.

[47] Özturan, T., and Çeçen, C. Effect of coarse aggregate type on mechanical properties of concretes with different strengths. *Cement and Concrete Research 27*, 2 (1997), 165–170.

[48] Poinard, C. *Comportement du béton sous chargement triaxial sévère : analyse tomographique et modélisation à l'échelle mésoscopique*. PhD thesis, Université de Grenoble, France, 2010.

[49] Poinard, C., Malécot, Y., and Daudeville, L. Damage of concrete in a very high stress state: experimental investigation. *Materials and Structures 43* (2010), 15–29.

[50] Poinard, C., Piotrowska, E., Malécot, Y., Daudeville, L., and Landis, E. N. Compression triaxial behavior of concrete: the role of the mesostructure by analysis of X-ray tomographic images. *European Journal of Environmental and Civil Engineering 16*, sup1 (2012), 115–136.

[51] Roelfstra, P., Sadouki, H., and Wittmann, F. Le béton numérique. *Materials and Structures 18* (1985), 327–335.

[52] Roux, J.-N., and Chevoir, F. Dimensional analysis and control parameters. In *Discrete-element Modeling of Granular Materials*, Radja Ed. pp. 199–232.

[53] Roux, J.-N., and Chevoir, F. Discrete numerical simulation and the mechanical behavior of granular materials. *Bulletin des Laboratoires des Ponts et Chaussées 254* (2005), 109–138.

[54] Schlangen, E., and van Mier, J. Simple lattice model for numerical simulation of fracture of concrete materials and structures. *Materials and Structures 25* (1992), 534–542.

[55] Schmidt, M., Cazacu, O., and Green, M. Experimental and theoretical investigation of the high-pressure behavior of concrete. *International Journal for Numerical and Analytical Methods in Geomechanics 33*, 1 (2009), 1–23.

[56] Scrivener, K., Crumbie, A., and Laugesen, P. The interfacial transition zone (ITZ) between cement paste and aggregate in concrete. *Interface Science 12*, 4 (2004), 411–421.

[57] Scrivener, K. L. Backscattered electron imaging of cementitious microstructures: understanding and quantification. *Cement and Concrete Composites 26*, 8 (2004), 935–945.

[58] Sfer, D., Carol, I., Gettu, R., and Etse, G. Study of the behavior of concrete under triaxial compression. *Journal of Engineering Mechanics 128*, 2 (2002), 156–163.

[59] Shiu, W., Donzé, F. V., and Daudeville, L. Compaction process in concrete during missile impact: a DEM analysis. *Computers and Concrete 5*, 4 (2008), 329–342.

[60] Taylor, H. *Cement Chemistry*. T. Telford, 1997.

[61] Topin, V., Delenne, J.-Y., Radjaï, F., Brendel, L., and Mabille, F. Strength and failure of cemented granular matter. *The European Physical Journal E: Soft Matter and Biological Physics 23*, 4 (2007), 413–429.

[62] Verbeck, G. *Hardened Concrete – Pore Structure*. ASTM special technical publication. Portland Cement Association, Research and Development Laboratories, 1956.

[63] Vu, X. H. *Caractérisation expérimentale du béton sous fort confinement : influences du degré de saturation et du rapport eau/ciment*. PhD thesis, Université Joseph Fourier, Grenoble, France, 2007.

[64] Vu, X. H., Daudeville, L., and Malécot, Y. Effect of coarse aggregate size and cement paste volume on concrete behavior under high triaxial compression loading. *Construction and Building Materials 25*, 10 (2011), 3941–3949.

[65] Vu, X. H., Malécot, Y., and Daudeville, L. Strain measurements on porous concrete samples for triaxial compression and extension tests under very high confinement. *The Journal of Strain Analysis for Engineering Design 44*, 8 (2009), 633–657.

[66] Vu, X. H., Malécot, Y., Daudeville, L., and Buzaud, E. Effect of the water/cement ratio on concrete behavior under extreme loading. *International Journal for Numerical and Analytical Methods in Geomechanics 33*, 17 (2009), 1867–1888.

[67] Vu, X. H., Malécot, Y., Daudeville, L., and Buzaud, E. Experimental analysis of concrete behavior under high confinement: Effect of the saturation ratio. *International Journal of Solids and Structures 46*, 5 (2009), 1105–1120.

[68] Wong, R., and Chau, K. Estimation of air void and aggregate spatial distributions in concrete under uniaxial compression using computer tomography scanning. *Cement and Concrete Research 35*, 8 (2005), 1566–1576.

[69] Wriggers, P., and Moftah, S. Mesoscale models for concrete: Homogenisation and damage behaviour. *Finite elements in analysis and design 42*, 7 (2006), 623–636.

[70] Zhou, F., Lydon, F., and Barr, B. Effect of coarse aggregate on elastic modulus and compressive strength of high performance concrete. *Cement and Concrete Research 25*, 1 (1995), 177–186.

[71] Zukas, J. *Penetration and perforation of solids, Impact Dynamics*. Impact Dynamics. Krieger Publishing Co., 1992.